NREL

National Renewable Energy Laboratory

Innovation for Our Energy Future

Optimization of Phase-Engineered a-Si:H-Based Multi-Junction Solar Cells

Final Technical Report
October 2001 — July 2005

C.R. Wronski, R.W. Collins, N.J. Podraza,
V. Vlahos, J.M. Pearce, J. Deng, M. Albert,
G.M. Ferreira, and C. Chen
Pennsylvania State University
University Park, Pennsylvania

Optimization of Phase-Engineered a-Si:H-Based Multi-Junction Solar Cells

Final Technical Report
October 2001 — July 2005

C.R. Wronski, R.W. Collins, N.J. Podraza,
V. Vlahos, J.M. Pearce, J. Deng, M. Albert,
G.M. Ferreira, and C. Chen
Pennsylvania State University
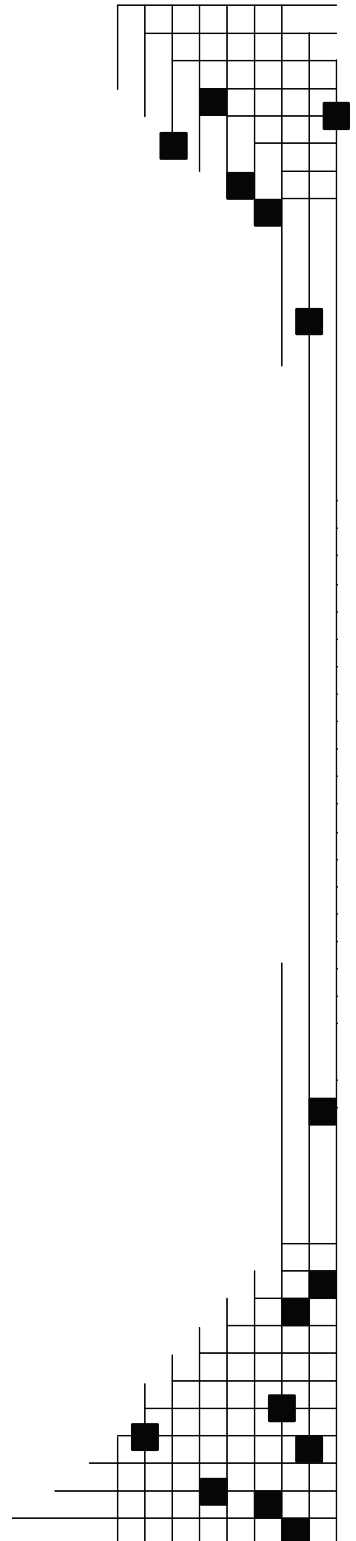*University Park, Pennsylvania*

National Renewable Energy Laboratory
1617 Cole Boulevard, Golden, Colorado 80401-3393
303-275-3000 • www.nrel.gov

Available electronically at http://www.osti.gov/bridge

Available for a processing fee to U.S. Department of Energy
and its contractors, in paper, from:
      U.S. Department of Energy
      Office of Scientific and Technical Information
      P.O. Box 62
      Oak Ridge, TN 37831-0062
      phone: 865.576.8401
      fax: 865.576.5728
      email: mailto:reports@adonis.osti.gov

Available for sale to the public, in paper, from:
      U.S. Department of Commerce
      National Technical Information Service
      5285 Port Royal Road
      Springfield, VA 22161
      phone: 800.553.6847
      fax: 703.605.6900
      email: orders@ntis.fedworld.gov
      online ordering: http://www.ntis.gov/ordering.htm

Table of Contents

List of Figures

iv

List of Tables

Executive Summary

The restructuring in the program brought about by the move of co-PI Robert Collins to the University of Toledo in the third phase of this subcontract has proceeded smoothly. One of the graduate students associated with the project continued working at Penn State applying the same single-chamber system fitted with real time spectroscopic ellipsometry (RTSE) instrumentation that was used during the first and second phases of the project. This student continued to perform in-situ RTSE studies of the growth of a-Si$_{1-x}$Ge$_x$:H materials for high performance solar cells. Construction of a new Dual Beam Photoconductivity (DBP) apparatus has been completed, and the new capabilities are being utilized in studies of a-Si:H thin films. A new apparatus has also been constructed for in-depth studies of the mechanisms limiting the performance of a-Si:H solar cells and for the parallel-track studies (cells and films) of the Staebler-Wronski Effect (SWE). The capabilities include integration of the cell characteristics including the Q.E. at different temperatures on both p-i-n and n-i-p solar cells. The scope of the work under this subcontract has entailed investigating engineered improvements in the performance and stability of solar cells in a *systematic* way. It has consisted of the following four tasks.

> **Task 1.** Materials research and device development
> **Task 2.** Process improvement directed by real time diagnostics
> **Task 3.** Device loss mechanisms
> **Task 4.** Characterization strategies for advanced materials

The work carried out in these tasks has resulted in new and important insights into the deposition of a-Si:H-based materials, as well as into the nature of the SWE. Presumably, many of these insights have been utilized by the industrial partners in developing more *systematic* approaches in the optimization of solar cells for higher performance and stability. This effort also cleared up several serious misconceptions that are still being held about the nature of the p-layer in cells and the SWE in materials and cells. Finally, the subcontract identified future directions that should be pursued for greater understanding and improvements.

Task 1. Materials Research and Device Development

In Task 1, an understanding of n-i-p (substrate) solar cells was achieved and on the basis of this understanding, optimization was carried out. The inherent differences between n-i-p and p-i-n (superstrate) cell structures have been addressed. Phase diagrams have been developed using real time spectroscopic ellipsometry (RTSE) and applied to characterize thin film growth and microstructure, comparing the two configurations. Such an approach has been successful in explaining the nature of p-type Si:H films doped using BF$_3$ and guiding the development of high V$_{OC}$ in n-i-p solar cells. The results show that in order to maximize V$_{OC}$, it is necessary to deposit the p-layers at the maximum R value that allows the desirable thickness to be obtained without crossing the transition into the mixed-phase growth regime. This study also showed that previous work reporting the highest V$_{OC}$ for microcrystalline Si:H p-layers was erroneous. The possible mechanisms responsible for the differences in 1 sun V$_{OC}$ obtained with the different p-type Si:H layers were explored. Carrier recombination in cell structures was characterized with J$_D$-V measurements, and the recombination in the p/i and i/p interface regions was identified and quantified. These systematic studies clearly established that the lowest p/i interface recombination is

1

obtained with *protocrystalline a-Si:H* and not with layers containing any *microcrystalline* phase. (When the microcrystalline phase appears, V_{OC} is also significantly lower than that achieved with the structure incorporating the optimum a-Si$_{1-x}$C$_x$:H p-layer.) The significantly lower i/p interface recombination in the cells with the protocrystalline Si:H p-layer is attributed in large part to the sub-surface modification of the underlying intrinsic layer that occurs during the deposition of the p-layer contact. Evidence is found that the high concentration of atomic hydrogen present during the deposition of the protocrystalline Si:H p-layer is responsible for this beneficial effect. In addition, unlike a-Si$_{1-x}$C$_x$:H, it allows the protocrystalline p-layer to be used in fabricating solar cell structures without any adverse effect of exposing the i-layers to air.

The optimization of rf and vhf PECVD materials for high rate i-layers of Si:H solar cells based on the deposition phase diagram was also investigated. It is found that under H$_2$ deficient dilution conditions, vhf (60 MHz) PECVD provides significant advantages over rf (13.56 MHz) PECVD in the fabrication of higher quality a-Si:H at high rates. Under optimum conditions, however, with the H$_2$-dilution ratio set just below the a→(a+μc) transition for the desired film thickness, vhf PECVD provides no significant advantage over rf PECVD when identical high deposition rates are compared. It was also found that in a high plasma power, high pressure (3 Torr) rf PECVD process for a-Si:H film growth, the amorphous phase roughening transition thickness remains above 1000 Å just below the a→(a+μc) boundary where the rate is 6.5 Å/s. This transition thickness is a factor of two higher than that observed under low pressure deposition conditions with almost a factor of two lower deposition rate for the a-Si:H.

In fact, three manifestations of enhanced precursor surface diffusion are found with increasing H$_2$-dilution ratio R under all conditions of a-Si:H deposition explored: (i) increased surface smoothening (both rate and amplitude) associated with the coalescence of initial nuclei in the first 100 Å of deposition; (ii) reduced surface roughness layer thickness at the stable surface value; and (iii) increased surface stability as measured by the thickness of the a→a roughening transition. The presence of all three effects provide clear signatures of improved-device quality materials based on the monolayer level processes detected at the film surface. As a result, we can conclude that the appropriate combination of high R [at the a→ (a+μc) transition for the desired film thickness], high power, and high pressure give rise to reasonable device performance at rates > 6 Å/s, without resorting to unconventional deposition methods.

Because the a→(a+μc) transition decreases in thickness with increasing R, two-step and even multi-step i-layer processes can be designed on the basis of the phase diagram in order to optimize solar cells. Optimization of rf and vhf PECVD materials for high rate i-layers of a-Si:H solar cells based on the deposition phase diagram has been further explored. The similarities of the phase diagrams for both rf and vhf PECVD of Si:H on R=0 a-Si:H substrate films demonstrate that the two-step optimization procedure developed for the rf PECVD protocrystalline i-layers of a-Si:H-based p-i-n and n-i-p cells also apply for vhf PECVD i-layers as well.

Task 2. Process Improvement Directed by Real Time Diagnostics

In Task 2, real time spectroscopic ellipsometry was applied in the development of deposition phase diagrams for guiding the fabrication of hydrogenated silicon (Si:H) and hydrogenated amorphous silicon germanium (a-Si$_{1-x}$Ge$_x$:H) thin films at low temperatures (<300°C) for high performance solar cells. Phase diagrams have been extended to include the thickness at which a roughening transition is detected in the amorphous film growth regime. The three surface microstructural and phase transitions, including the a→a roughening transition, the a→(a+μc)

2

roughening transition, and the (a+μc)→μc smoothening transition have been incorporated into an extended deposition phase diagram. Correlations of such phase diagrams for the intrinsic Si:H layers with the corresponding electronic properties and p-i-n device performance demonstrate that the optimum i-layers are obtained at the maximum possible R value for the desired thickness without crossing the a→(a+μc) boundary of the phase diagram into the mixed-phase growth regime. Because the R value at this phase boundary depends on both the nature of the substrate and the i-layer thickness, these aspects of the materials or device structure must be specified in order to identify the optimum conditions for i-layers deposited on amorphous film substrates (such as the p or n-layers of p-i-n or n-i-p solar cells). The optimum a-Si:H i-layer material has been described as *protocrystalline* Si:H -- this material ultimately evolves into (a+μc)-Si:H if the film is allowed to grow beyond the desired thickness for which the deposition process was optimized.

Schematic of the structure of Si:H films
prepared at different R on a-Si:H (R=0)
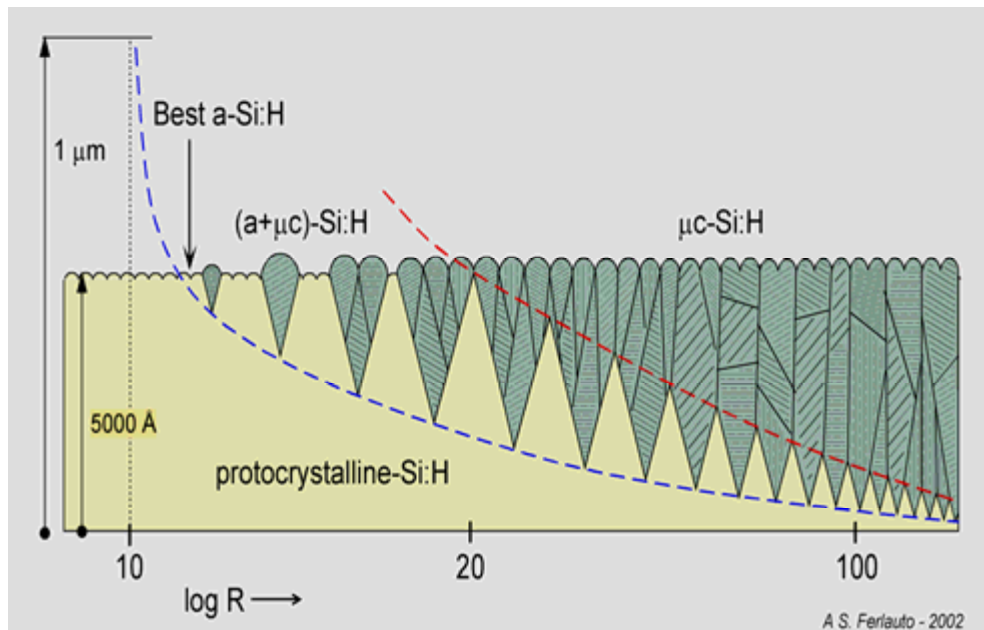
• *In this project it is emphasized that great attention must be given to the a→(a+μc) transition and the thickness evolution of the crystalline phase in both films and cells. In fact, the resulting film will exhibit a depth profile in the crystalline content if the film crosses the transition at any point during the course of the deposition.*

2.1 $Si_{1-x}Ge_x$:H Roughness and Phase Evolution

Overview

Extensive research on hydrogenated amorphous silicon (a-Si:H) thin films has shown that optimum device performance is correlated with the smoothest, most stable surfaces versus time during the PECVD process – in fact, less than a monolayer of roughening occurs throughout the deposition of optimum films as thick as 0.5 μm [2.1]. Such research requires smooth crystalline silicon substrates for high sensitivity to surface roughness as well as an in situ probe such as spectroscopic ellipsometry (SE) for real-time analysis. It has been also shown that when the PECVD conditions deviate from the optimum even slightly, e.g., by a reduction in the hydrogen dilution ratio or by an increase in plasma power from its minimum, then a roughening transition is observed in the a-Si:H growth regime [2.1]. This transition shifts to decreasing bulk layer thickness for films with increasingly deteriorated device properties. As a result, the thickness at which the roughening transition (denoted a → a) occurs has been entered into deposition phase diagrams, relevant for c-Si substrates, that provide insights into the device quality of a-Si:H and how it varies with deposition parameters.

In this study, the amorphous-phase roughening transition thickness has been determined as a function of process variables in plasma-enhanced chemical vapor deposition (PECVD) of hydrogenated amorphous silicon-germanium alloys (a-$Si_{1-x}Ge_x$:H). Among the process variables include the H_2-dilution gas flow ratio, the alloying flow ratio, the electrode configuration (anode vs. cathode), the substrate temperature, and the He-dilution ratio. One clear feature of this study is a maximum in the amorphous roughening transition thickness (and hence surface stability) at a H_2-dilution ratio just below the transition from amorphous to mixed-phase (amorphous + microcrystalline) growth. A second feature for high Ge content films is a significant increase in the roughening transition thickness for cathode PECVD (with a self-bias of ~ –20 V). Additional features of interest involve suppression of the mixed-phase transition for (i) alloying with Ge, (ii) decreasing substrate temperature, (iii) cathodic substrate biasing, and (iv) diluting the gas with He.

Experimental Details

The $Si_{1-x}Ge_x$:H films in this study were deposited onto native-oxide/c-Si substrates using single-chamber rf (13.56 MHz) PECVD and were measured in real time using a rotating-compensator multichannel ellipsometer [2.2]. The fixed parameters were selected for the most part at values used in previous studies of pure Si:H PECVD [2.1], the minimum plasma power for a stable plasma (P ~ 0.08 W/cm^2), a low partial pressure of the source gases {[SiH_4]+[GeH_4]} (~ 0.06 Torr), and a low total pressure (p_{tot} < 1.0 Torr). In this study, the primary phase diagram variable was the H_2-dilution ratio R = [H_2]/{[SiH_4]+[GeH_4]}, as usual. The other variable parameters include (i) alloying flow ratio G = [GeH_4]/{[SiH_4]+[GeH_4]} which was varied from G=0 to G=0.167, leading to x values up to 0.4; (ii) substrate temperature which was varied over the range 200°C $\leq$ T_s $\leq$ 320°C; (iii) electrode configuration (see [2.3]), either the conventional anode or the cathode the latter with a dc self-bias of ~ –20 V; and (iv) He-dilution defined by the flow ratio He=[He]/{[SiH_4]+[GeH_4]} which was varied from 0 to 90. The optical gap of the a-$Si_{1-x}Ge_x$:H reached its minimum of ~1.3 eV for the maximum G value, with smaller variations due to the other parameters.

Results and Discussion

Comparison of Si:H and Si$_{1-x}$Ge$_x$:H films prepared on the anode at T=200°C

A comparison of the deposition rates is shown in Fig. 2.1 for Si:H and Si$_{1-x}$Ge$_x$:H similarly-prepared on the reactor anode at 200°C with a rf plasma power of 0.08 W/cm^2 and a source gas partial pressure of ~0.06 Torr. The only difference in the process for Si$_{1-x}$Ge$_x$:H is the replacement of 1/5 of the SiH$_4$ flow by GeH$_4$. The significantly higher rates for the alloys are attributed to the ease with which GeH$_4$ is dissociated in the plasma relative to SiH$_4$.

Figure 2.2 shows the superimposed deposition phase diagrams for the pure Si:H and Si$_{1-x}$Ge$_x$:H alloy thin films of Fig. 2.1. Two significant differences are observed between these diagrams, indicating the profound effect of alloying. First, the a→(a+μc) transition for the series of Si$_{1-x}$Ge$_x$:H alloys is shifted to much larger R compared to pure Si:H. Thus, the presence of Ge in the growth process suppresses the nucleation of microcrystals from the amorphous phase. Second, the a→a roughening transition for the a-Si$_{1-x}$Ge$_x$:H saturates at a low bulk layer thickness of 200 Å, even as the a→(a+μc) transition for thick films is approached and crossed. In contrast, for Si:H, the a→a roughening transition increases sharply, exceeding a bulk layer thickness of 4000 Å, as the a→(a+μc) transition is approached. This difference suggests that the diffusion length of film precursors on the surface during growth is significantly reduced for the alloys, likely due to surface defects that immobilize the precursors. Furthermore, because the a→a transition thickness remains at ~200 Å throughout the range of R from R = 40 to 70 [i.e., up to the a→(a+μc) transition for the bulk layer thickness desired in the device], it would appear that no significant gain in the device performance of the alloys can be realized by increasing the H$_2$-dilution over this range.
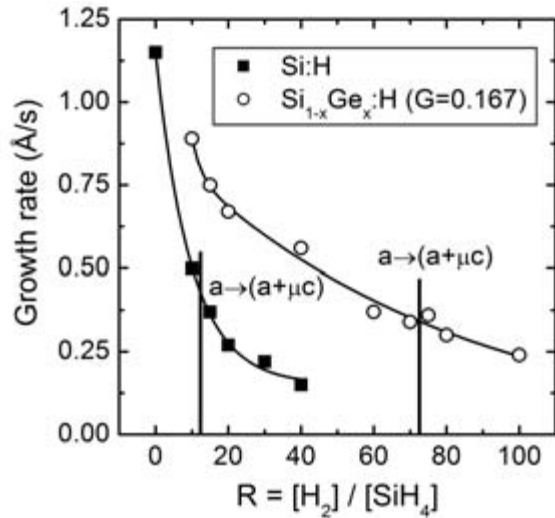
Fig. 2.1: A comparison of the deposition rates of pure Si:H and Si$_{1-x}$Ge$_x$:H alloy films as a function of the H$_2$-dilution ratio. These films were prepared on native oxide-covered c-Si substrates mounted on the reactor anode and held at 200°C.
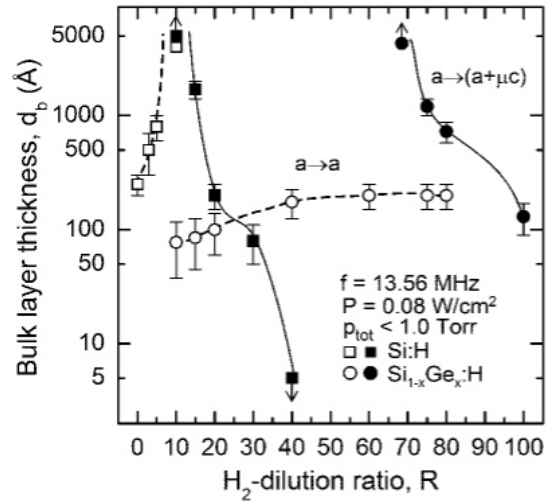
Fig. 2.2: Superimposed phase diagrams for Si:H (squares) and Si$_{1-x}$Ge$_x$:H (circles) films deposited at low power (0.08 W/cm^2) and low total pressure (< 1 Torr) on oxide-covered c-Si. These substrates were mounted on the anode and held at 200°C. The (up, down) arrows indicate that the transition occurs (above, below) the designated value.
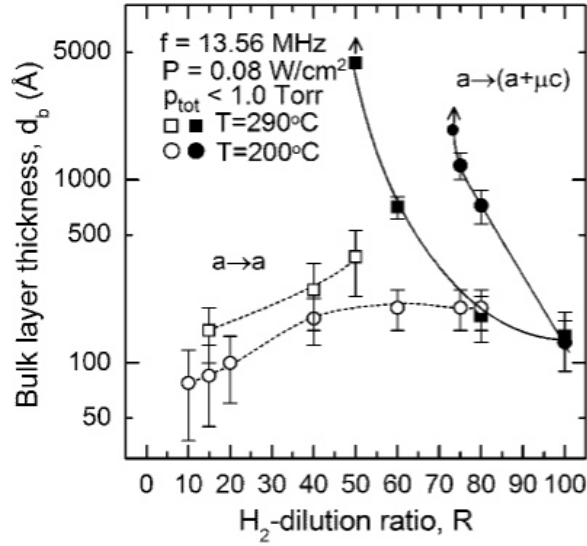
Fig. 2.3: Superimposed phase diagrams for $Si_{1-x}Ge_x$:H films deposited on the anode under similar conditions at two different substrate temperatures (T=200°C and T=290°C). The temperature increase shifts the onset of the mixed phase transition to lower R, and generally results in an increased bulk layer thickness for the a$\rightarrow$ a transition.

In the next paragraphs, the effect of other deposition characteristics and parameters on the $Si_{1-x}Ge_x$:H phase diagram will be demonstrated, including substrate temperature, electrode configuration, and He dilution in an attempt to increase the a$\rightarrow$a transition to bulk layer thicknesses much greater than the 200 Å observed in Fig. 2.2.

Comparison of $Si_{1-x}Ge_x$:H films prepared on the anode at varying substrate temperature

Previous phase diagram studies of pure Si:H prepared at elevated deposition rates (~3.5 Å/s) are relevant to the present studies of $Si_{1-x}Ge_x$:H, since higher plasma power levels and gas phase GeH_4 incorporation each lead to significantly reduced a$\rightarrow$a transition thicknesses [2.4]. In attempts to improve the situation for Si:H, previous phase diagram studies have shown that by increasing the substrate temperature to 260°C, the a$\rightarrow$(a+μc) transition shifts to lower R, and as a result the R value for optimum a-Si:H must be decreased in order to maintain deposition within the amorphous regime of the phase diagram for the desired thickness. This decrease in R leads to a decrease in the a$\rightarrow$a transition thickness even below that obtained for maximal R, high-rate deposition at 200°C. In essence, the detrimental effect of crystallite nucleation overcomes any possible improvement in the growth process due to enhanced surface diffusion.

In contrast to the case of pure Si:H, the broad range of R for a-$Si_{1-x}Ge_x$:H over which the a$\rightarrow$a transition thickness remains constant (40 $\leq$ R $\leq$ 70) suggests that, in elevating the temperature above 200°C, improvements can be made in the maximal R condition [that is, in spite of the expected shift to lower R in the a$\rightarrow$(a+μc) transition]. This suggestion is borne out in the phase diagram for $Si_{1-x}Ge_x$:H prepared at T=290°C, shown in Fig. 2.3 for comparison with the corresponding diagram from Fig. 2.2 for $Si_{1-x}Ge_x$:H prepared at T=200°C. First, Fig. 2.3 reveals the expected shift in the a$\rightarrow$(a+μc) transition to lower R with the increase in substrate temperature, from R=80 to 60 for a 5000 Å thick film. Second with the increase in temperature, the a$\rightarrow$a transition shifts to higher d_b from ~ 200 to more than 400 Å, indicating an enhancement in surface diffusion, and an expected modest improvement in material characteristics for solar cells.

6
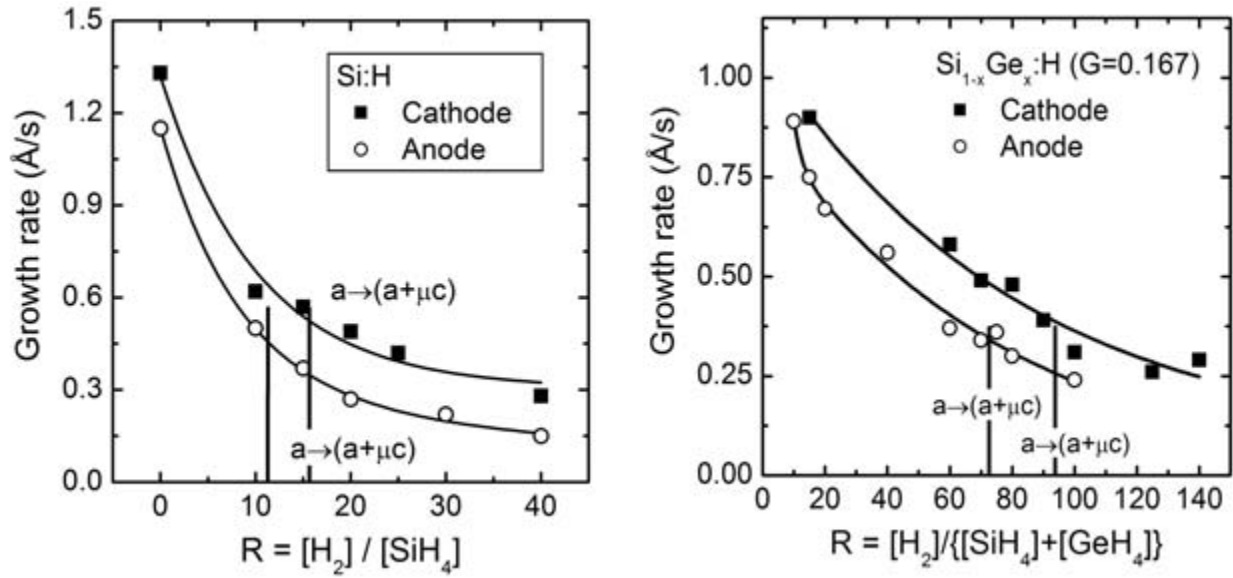
Fig. 2.4: (Above) Comparison of deposition rates for anode and cathode Si:H and $Si_{1-x}Ge_x$:H thin film series versus the H_2-dilution ratio, $R = [H_2]/\{[SiH_4]+[GeH_4]\}$. The alloy flow ratio $G = [GeH_4]/\{[SiH_4]+[GeH_4]\}$ was fixed at $G = 0$ and $G = 0.167$, respectively.

Additional phase diagrams have also been developed for processes at 260°C and 320°C, as well as for a two step, 200°C/320°C process, the latter in order to enhance the nucleation density on the substrate and characterize the surface diffusion processes with greater confidence. Furthermore, a phase diagram versus temperature has been established for R=60. In all these studies, under no conditions of substrate temperature has the a→a transition been found to exceed ~ 500 Å.

Comparison of Si:H and $Si_{1-x}Ge_x$:H films prepared on the cathode

Having exhausted the potential of substrate temperature optimization to improve $Si_{1-x}Ge_x$:H surface stability under standard conditions, other less conventional approaches were considered. On the basis of previous successes by Paul et al. for a-Ge:H [2.3] and Ganguly et al. for a-Si:H [2.5], depositions were performed on the cathode of the reactor with a self-bias of ~ –20 V. The substrate temperature of T=200°C was maintained indirectly from the anode through radiative and conductive heating, the latter through the deposition gas. Because cathodic deposition is new to the phase diagram studies, depositions of pure Si:H on the cathode were also performed and the results will be reported for convenience together with those for $Si_{1-x}Ge_x$:H in the following paragraph and in Figs. 2.4-2.7.

Higher deposition rates for cathodic films (under otherwise identical conditions) are expected due to higher gas dissociation rates by the more energetic ions crossing the cathode sheath. This expectation is been borne out in the comparisons of the deposition rates for cathodic and anodic $Si_{1-x}Ge_x$:H [2.6] and for pure Si:H depicted in Fig. 2.4. Figure 2.5(a) depicts the dramatic differences in the microstructural evolution in a comparison of R=80 $Si_{1-x}Ge_x$:H films deposited on

7

the cathode and anode. The anodic $Si_{1-x}Ge_x$:H film exhibits an a→a roughening transition at d_b = 200 Å and an a→(a+μc) transition at d_b = 700 Å. In contrast, the cathodic $Si_{1-x}Ge_x$:H remains amorphous throughout, exhibiting a strong smoothening effect that leads to a stable surface with d_s ~ 7 Å that presists to a thickness of d_b~1500 Å, a factor of three higher than the best anodic result. Figure 2.5(b) shows the similarly dramatic differences between R=20 pure Si:H films deposited at the cathode and anode. The anodic Si:H film exhibits an initial strong smoothening effect in the amorphous growth regime to a roughness thickness of d_s ~ 2 Å at a bulk layer thickness of 150 Å. The film evolves through an a→(a+μc) transition almost immediately thereafter (d_b = 230 Å), however, and then through an (a+μc)→μc transition at d_b = 1400 Å, the latter characterized by a smoothening effect due to the coalescence of isolated crystallites. The cathodic Si:H film shows a similar smoothening effect, but in contrast exhibits sub-monolayer level roughness (d_s ~ 2 Å) throughout the growth of a 3500 Å thick film at which point the a→(a+μc) transition occurs. In this case, the extensive growth period with monolayer level smoothness, a key characteristic of protocrystallinity, is unique to the Si:H cathodic deposition.

Results for cathodic $Si_{1-x}Ge_x$:H deposition at 200°C such as those of Fig. 2.5(a) have been have been used to construct the phase diagram shown in Fig. 2.6, along with that for anodic deposition from Figs. 2.2 and 2.3. This comparison reveals two important effects. First, a significant shift in the a→(a+μc) transitions to higher R is observed for deposition on the cathode versus anode. Second, the a→a transition shifts to much larger thicknesses of 2000 Å for deposition on the cathode as the a→(a+μc) is approached. Such behavior suggests significant improvement in the precursor surface diffusion under cathodic conditions. It is possible that low energy ion impact in the top 1-2 monolayers of the film is sufficient to enhance the processes of H-elimination, leading to a more compact surface. This may also lead to a suppression of microcrystallite nucleation which has been proposed to involve clusters of specific Si-H bonding structures in the top 1-2 monolayers [2.7]. The high H_2-dilution R > 60 ensures a low defect density as H-elimination proceeds. The results for cathodic Si:H depositions have been used to construct the phase diagram of Fig. 2.7 which reveals
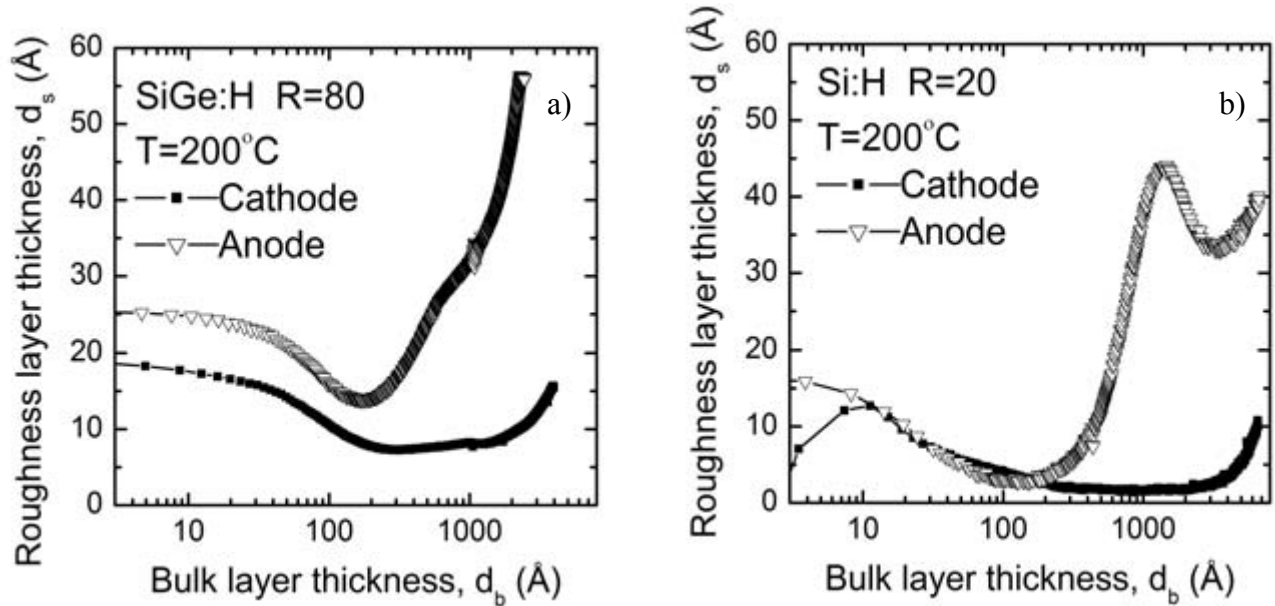
Fig. 2.5: Comparison of the structural evolution of (a) $Si_{1-x}Ge_x$:H and (b) Si:H films deposited on c-Si substrate mounted at the anode (triangles) and cathode (squares) using R=80 and R=20, respectively.
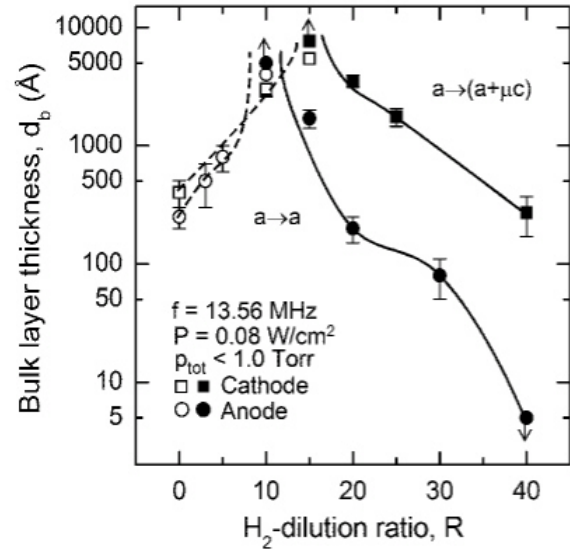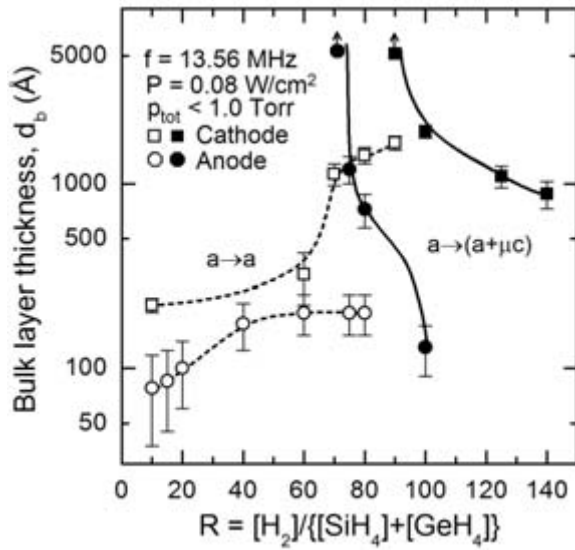
Figs. 2.6 and 2.7: Superimposed deposition phase diagrams for the cathode (squares) and anode (circles) $Si_{1-x}Ge_x$:H and Si:H alloy series plotted as a function of H_2-dilution, R. The alloy flow ratio $G = [GeH_4]/\{[SiH_4]+[GeH_4]\}$ was fixed at 0.167 and 0, respectively. The broken lines denote the amorphous roughening transition (a → a), and the solid lines denote the amorphous-to-mixed phase transition [a → (a+µc)].

similar qualities. Again, compared to the anodic depositions, the cathodic conditions shift the a→(a+µc) transitions to higher R. This effect is advantageous in that an extended protocrystalline regime becomes available at higher dilution levels, even though the a→a transition thickness is reduced somewhat at the a→(a+µc) transition for a thick layer.

Comparison of $Si_{1-x}Ge_x$:H films prepared on the cathode with varying G

Figure 2.8 depicts the optical band gaps of the $Si_{1-x}Ge_x$:H samples versus the GeH_4 flow ratio G for $Si_{1-x}Ge_x$:H films prepared with a cathodic electrod configuration. The results shown as the points and solid lines were obtained from real time spectroscopic ellipsometry data collected at the deposition temperature (T=200°C) and deduced from extrapolations of $\varepsilon_2^{1/2}$ versus E, assuming a constant dipole matrix element (see inset). The gaps of the films prepared at R values just before the [a→ (a+µc)] transition (R=10 for G=0; R=40 for G=0.083; and R=90 for G=0.167) are within the range of 1.23 to 1.66 eV. Also shown in Fig. 2.8 are room temperature (T=20°C) estimates based on an optical gap shift of ~0.08 eV (or 4.5×10^{-4} eV/°C; broken line). Estimated room temperature Tauc gaps [extrapolations of $(\varepsilon_2 E^2)^{1/2}$ versus E, assuming a constant momentum matrix element], as would be measured by transmission spectroscopy on thick films, range from 1.35 to 1.78 eV when the band gap is extrapolated from photon energies close to the gap. A ~ 0.04 eV increase in gap is attributed to the differences in optical gap extrapolation methodology (constant momentum versus constant dipole matrix element) [2.8].

Figure 2.9 shows the surface roughness layer thickness versus bulk layer thickness during Si:H and $Si_{1-x}Ge_x$:H growth for two pairs of depositions, each pair at the same R but different ratios G. These two pairs were selected to show two trends to be emphasized in the phase diagrams presented
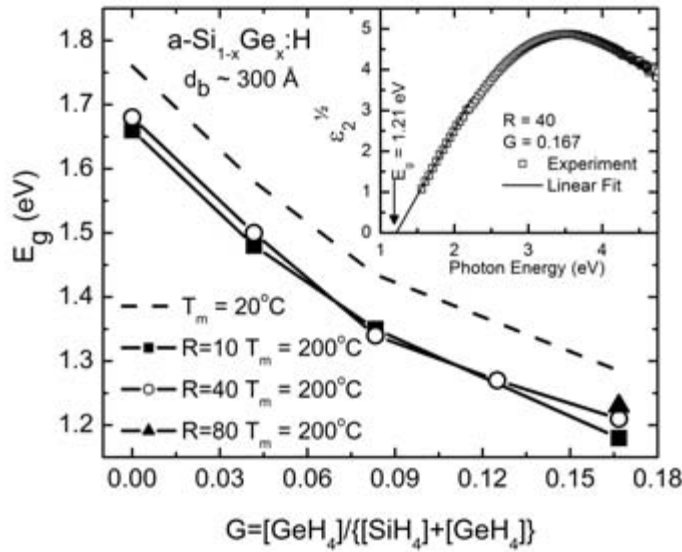
Fig. 2.8 Optical band gap as a function of GeH$_4$ flow ratio G determined from real time spectroscopic ellipsometry applying a linear extrapolation to $\varepsilon_2^{1/2}$ spectra obtained at the deposition temperature of T=200°C (main panel; points) and approximated to room temperature assuming a linear temperature coefficient of 4.5x10^4 eV/$^{\circ}$C (broken line). The inset shows a typical extrapolation that provides the gap.

in Fig. 2.10. In the main part of Fig. 2.9, the role of GeH$_4$ addition of G=0.083 is shown for R=10. The key effect is the shift of the roughening transition in the amorphous growth regime, denoted a→a, to much lower thicknesses. In the inset, the role of the same GeH$_4$ addition is shown for R=40. The key effect in this case is the shift of the amorphous-to-(mixed phase microcrystalline) roughening transition, denoted a → (a+μc), to larger thicknesses outside the accessible range. In fact, for G=0 and R=40, the Si:H film passes through amorphous, mixed-phase, and single-phase regimes during the growth of a 4000 Å thick film, whereas for G=0.083 and R=40, the Si$_{1-x}$Ge$_x$:H film remains fully amorphous over the same range of thickness.

Figure 2.10 depicts three superimposed phase diagrams for G values of G=0, 0.083, and 0.167, but otherwise identical PECVD conditions. These phase diagrams depict the a→a roughening transition thickness (as in Fig. 2.9, main part) and the a→(a+μc) transition thickness (as in Fig. 2.9, inset, with G=0) as functions of the H$_2$-dilution ratio R. A comparison of the overlapping phase diagrams yields the following three observations.

(i) Considering the phase diagrams collectively, the boundary defining the a → (a+μc) transition thickness shifts to much higher R *with increasing phase diagram G value*. In fact, the H$_2$-dilution level at which the a → (a+μc) transition occurs in an ~ 2000 Å thick film, increases from R=20 to R=100 as G increases from G=0 to G=0.167.

(ii) Considering each of the three phase diagrams individually, the a → a roughening transition thickness increases with increasing H$_2$-dilution ratio right up to the R value at which the a → (a+μc) transition occurs. For example with G =0.083, the a → a transition thickness increases from d$_b$ ~ 250 Å to d$_b$ ~ 3500 Å with increasing R over the amorphous growth regime.

(iii) Returning to the phase diagrams collectively, the maximum a → a transition thickness [which occurs at the R value just below the a → (a+μc) transition for a thick film] decreases *with increasing phase diagram G value*. In fact, the overall decrease from G=0 to G=0.167 is minimized by cathodic PECVD with a self bias of ~ −20 V, rather than conventional anodic PECVD [2.9].

Here it should be recalled that in previously-described phase diagram studies at G=0.167, where E$_g$(20°C) ~ 1.25-1.35 eV, deposition conditions were set to ensure microstructural evolution that reflects the highest electronic quality and stability, assuming correlations established between
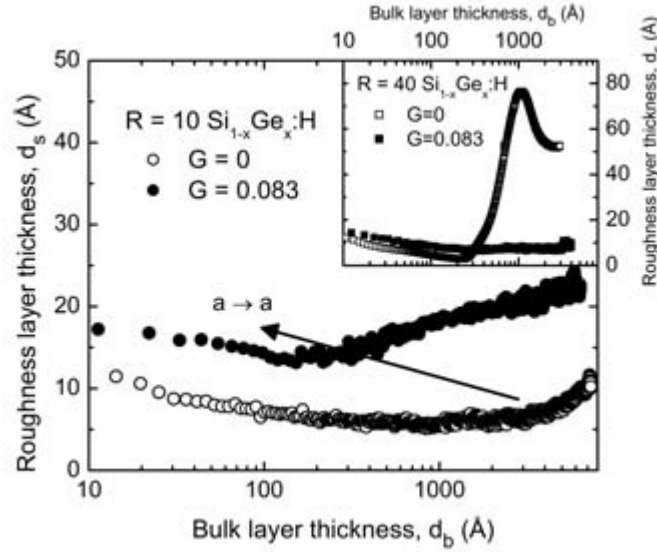
Fig. 2.9: Surface roughness evolution for two pairs of $Si_{1-x}Ge_x$:H films prepared under rf PECVD conditions that include: a substrate temperature of T=200°C, a total pressure of p<1 Torr, an rf power of P=0.08 W/cm^2, and a cathodic dc bias of V_{dc} ~ −20V. The main part shows a comparison of depositions with G=0 and 0.083 with the H_2 dilution ratio fixed at R=10 (in the amorphous regime for G=0), whereas the inset shows the corresponding comparison with R=40 (in the amorphous to microcrystalline evolution regime for G=0).
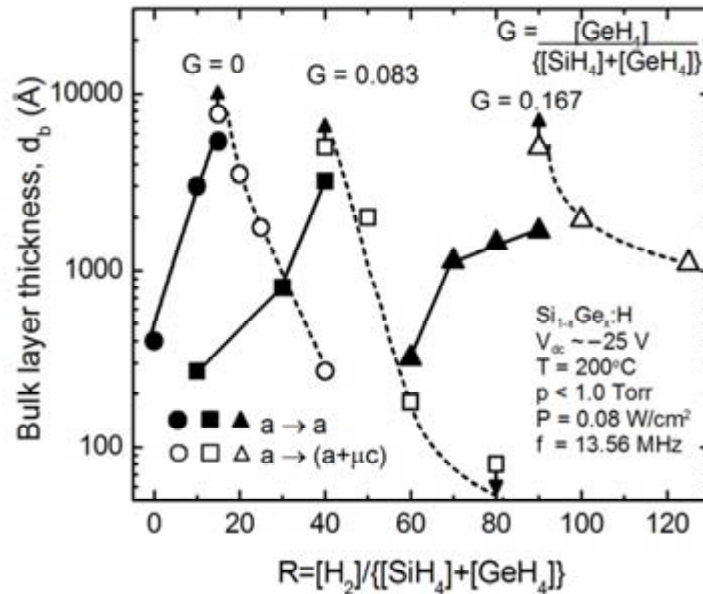
Fig. 2.10: Superimposed phase diagrams for different GeH_4 flow ratios G, each plotted versus the H_2 dilution level R. For each phase diagram, the thicknesses of the amorphous roughening transition are plotted (solid line and points) along with those of the amorphous-to-(mixed-phase-microcrystalline) transition (broken line and open points). Up- and down-arrows indicate that the transitions occur at thicknesses above or below the indicated values. [Left: G=0 (circles); center: G=0.083 (squares); and right: G=0.167 (triangles).]

11

phase diagrams and device characteristics for a-Si:H also hold for a-Si$_{1-x}$Ge$_x$:H [2.9]. These characteristics include the largest smoothening effect during coalescence, the lowest roughness layer thickness when a stable surface is reached, and the largest a $\rightarrow$ a roughening transition thickness, the latter evident directly from the phase diagram. PECVD at the cathode with a dc self-bias of $\sim$ -20 V, rather than at the grounded anode, was the key process difference for optimized microstructural properties at G=0.167 [2.9]. The improvement is attributed to a positive influence of weak ion-bombardment that can enhance near-surface dehydrogenation reactions and network ordering, but without causing damage through sub-surface atomic displacements [2.10].

Figures 2.11-13 show the effects on the deposition rate, the a $\rightarrow$ a transition thickness, and the dielectric function resonance width that result due to increases in R from 10 to the value just before the thick-film a $\rightarrow$ (a+μc) transition. These data are plotted versus G for a-Si$_{1-x}$Ge$_x$:H alloys prepared by optimum cathode PECVD as described in the previous paragraph. The solid line in Fig. 2.12 represents the a $\rightarrow$ a boundary plotted versus G for fixed R=10, and the broken line represents the corresponding boundary but for R selected as its maximum G-dependent value without crossing the a $\rightarrow$ (a+μc) transition. As a result, the broken lines in Figs. 2.11-13 represent optimized conditions versus R for the given G plotted along the abscissa. Such optimization was demonstrated in detail for pure a-Si:H (G=0) by usual anode PECVD through correlations with solar cell performance. Here, Fig. 2.13 depicts optimization of a-Si$_{1-x}$Ge$_x$:H by cathode PECVD through the width of the resonance in the 200°C dielectric function, which can be determined from the real time spectroscopic ellipsometry data together with the structural evolution. Narrowing of this resonance indicates improvement in short-range order in the network and accompanies narrowing of the Urbach tail [2.11]. Thus, Figs. 2.12 and 2.13 demonstrate that the increase in a $\rightarrow$ a transition thickness correlates with enhanced ordering.

Figure 2.14 shows a phase diagram in which case all three transition thicknesses are included: a $\rightarrow$ a, a $\rightarrow$ (a+μc), and (a+μc) $\rightarrow$ μc; however, the latter one is only observed for G = 0, i.e., only for pure SiH$_4$ depositions. For the non-zero G values, single phase microcrystalline Si$_{1-x}$Ge$_x$:H cannot be obtained, irrespective of thickness. The new phase diagram in Fig. 2.14 exhibits features similar to the diagrams versus R; however, the behavior vs. the abscissa is reversed: crystallite development occurs at low rather than high abscissa values. Finally, it should be noted that the phase diagram of Fig. 2.14 exhibiting structural and phase transitions versus G is expected to be useful in optimization of Ge grading in the i-layers of solar cells. It is clear from this figure that optimized grading of Ge will require simultaneous variations in H$_2$-dilution ratio R, i.e., to higher R with increasing G and vice versa. These phase diagrams can direct such a process, and this will be a focus of future efforts.

Comparison of Si$_{1-x}$Ge$_x$:H films prepared with variable He dilution

Figures 2.15-17 provide a comparison between the roles of H$_2$-dilution and He-dilution for Si$_{1-x}$Ge$_x$:H alloys (G=0.167) prepared by standard anode PECVD. This study explores the possibility that He dilution can also improve the properties of Si$_{1-x}$Ge$_x$:H prepared by anode PECVD. Figure 2.15 shows the surface roughness evolution for a film prepared with R=80 without He-dilution. Under these conditions the a $\rightarrow$ a and a $\rightarrow$ (a+μc) transitions occur near bulk layer thicknesses of 200 and 800 Å, respectively, as depicted on the phase diagram of Fig. 2.2. The low value of the former transition thickness is an indication of a short precursor diffusion length on the film surface and poor electronic properties in spite of the proximity to the a $\rightarrow$ (a+μc) transition. As shown in Fig. 2.2, this situation is improved by conversion to the cathode PECVD in which case the
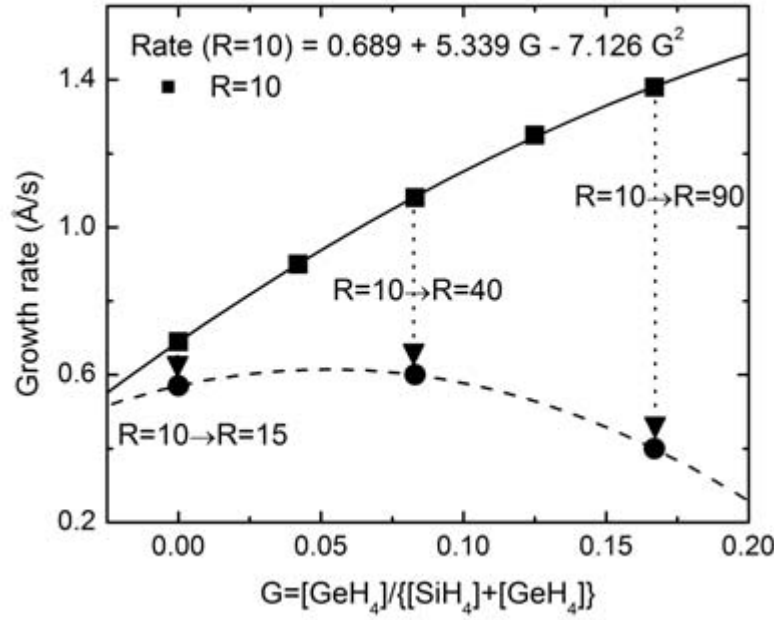
Fig. 2.11: Deposition rate for cathode $Si_{1-x}Ge_x$:H as functions of $G = [GeH_4]/\{[SiH_4]+[GeH_4]\}$ for R=10 and for the maximal R value before the thick-film (0.5 μm) a → (a+μc) transition is crossed.
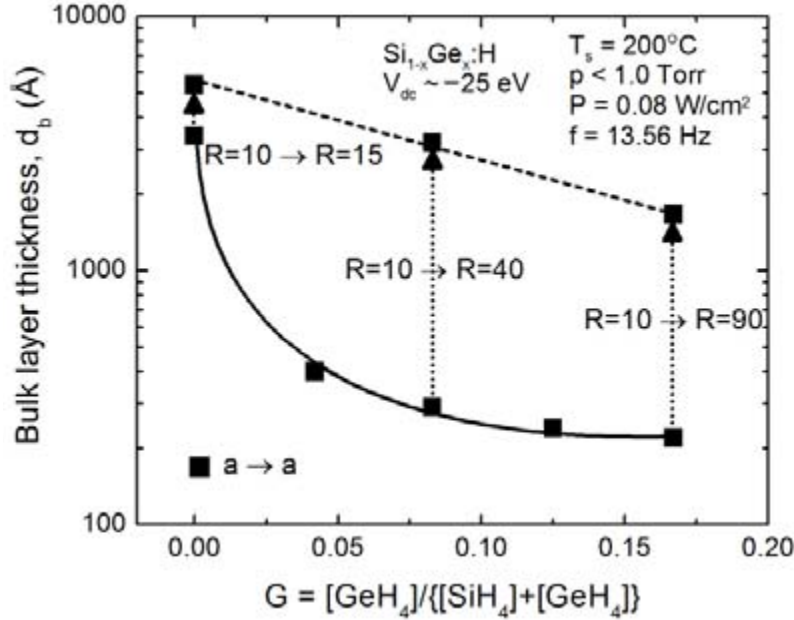
Fig. 2.12: A deposition phase diagram depicting the amorphous roughening transition (a→a) for R=10 a-$Si_{1-x}Ge_x$:H films plotted versus the alloy flow ratio $G=[GeH_4]/\{[SiH_4]+[GeH_4]\}$ (solid line and square points). The dotted arrows represent the increase in the a → a transition possible with the increase in R indicated, i.e., up to the amorphous-to-(mixed-phase) transition for a thick film. Thus, the broken line represents the phase boundary that results versus G for optimized a-$Si_{1-x}Ge_x$:H films versus R.

13
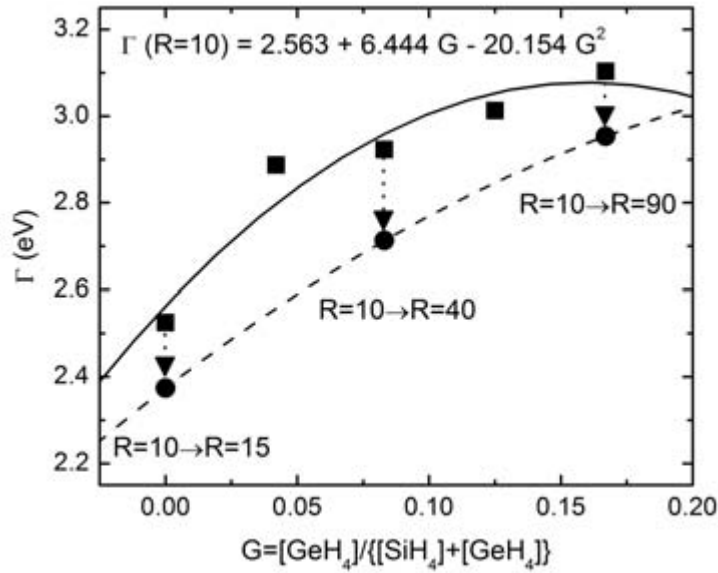
Fig. 2.13: Width of the resonance in the dielectric function (measured at 200°C and at a thickness of 150-300 Å) for cathode $Si_{1-x}Ge_x$:H as a function of $G = [GeH_4]/\{[SiH_4]+[GeH_4]\}$ for R=10 and for the maximal R value before the thick-film (0.5 μm) a → (a+μc) transition is crossed. Thus, the arrows indicate improvements in short-range order possible by increasing the R from 10 right up to the a → (a+μc) transition.
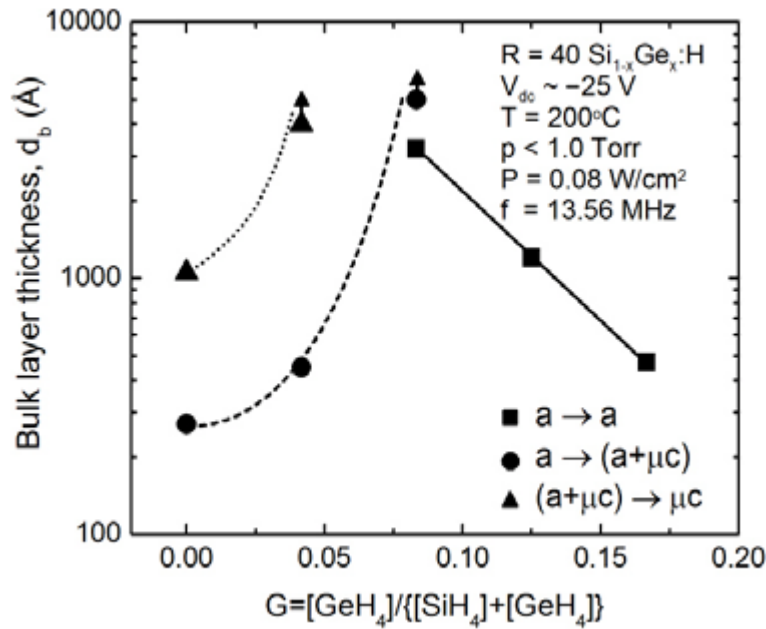
Fig. 2.14: A single deposition phase diagram for R= 40 $Si_{1-x}Ge_x$:H films plotted versus the GeH_4 flow ratio G. In this diagram, the thicknesses of the amorphous roughening transition (solid line and square points), the amorphous-to-(mixed-phase microcrystalline) transition (dashed line and circles), and the (mixed-phase)-to-(single-phase) microcrystalline transition (dotted line and triangles) are depicted. Up-arrows indicate that the transitions occur at thicknesses above the indicated value.

14
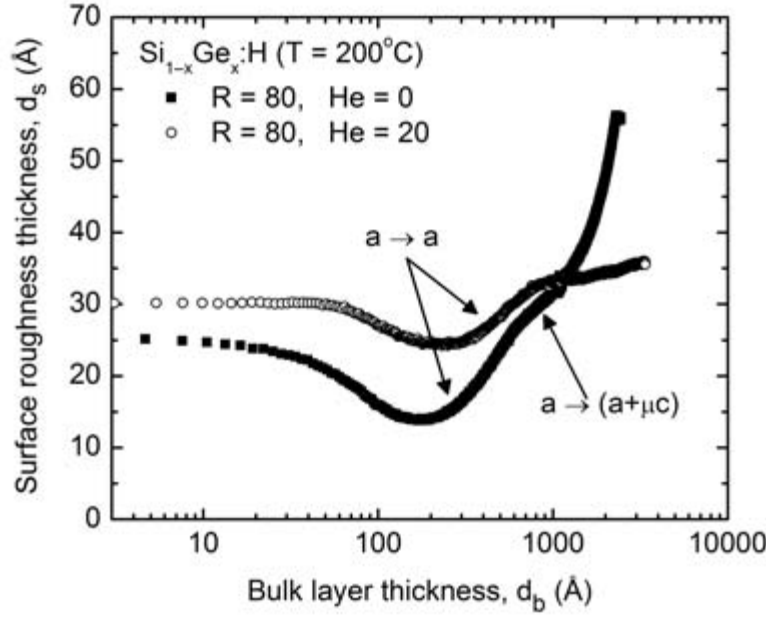
Fig. 2.15: (left) Surface roughness evolution for two $Si_{1-x}Ge_x$:H films prepared in the anode configuration with R=[H$_2$]/{[SiH$_4$]+[GeH$_4$]} = 80 and G=[GeH$_4$]/{[SiH$_4$]+[GeH$_4$]} = 0.167. One film was prepared with He=[He]/{[SiH$_4$]+[GeH$_4$]} = 0 and the other with He =20.
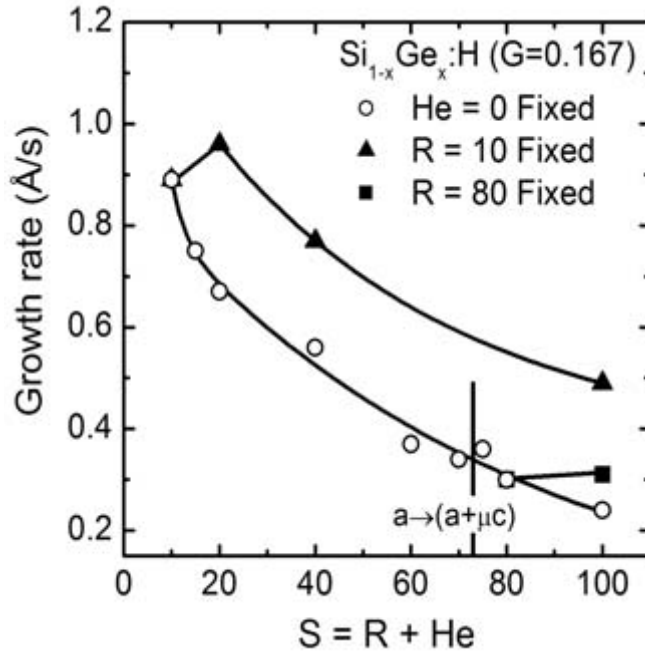
Fig. 2.16: (right) Deposition rate versus the combined [H$_2$+He]-dilution ratio S=R+He= {[H$_2$]+[He]}/{[SiH$_4$]+[GeH$_4$]} for $Si_{1-x}Ge_x$:H films prepared in the anode configuration with G=[GeH$_4$]/{[SiH$_4$]+[GeH$_4$]}= 0.167. Here, results for the nine depositions without He-dilution are plotted from Fig. 2.1, along with two series of depositions, one in which R is fixed at 10 and the dominant dilution effect is He (four depositions with He increasing from 0 to 90), and the other in which R is fixed at 80 and the dominant dilution effect is H$_2$ (two depositions with He = 0, 20).

15

a → (a+μc) transition is suppressed and the a → a transition increases considerably to ~1500 Å. Figure 2.15 also includes the roughness evolution of a film prepared with R=80 and He=[He]/{[SiH$_4$]+[GeH$_4$]}=20. In this case, the addition of He shifts the a →(a+μc) transition to higher R such that the film remains amorphous throughout deposition. Furthermore the a → a transition shifts to somewhat higher thickness, but not nearly as much as occurs with the change in electrode configuration. Figure 2.16 summarizes all results for deposition rate versus the combined [H$_2$+He]-dilution ratio S=R+He={[H$_2$]+[He]}/{[SiH$_4$]+[GeH$_4$]}. Here, results for the nine depositions without He-dilution are plotted from Fig. 2.1, along with two series of depositions, one in which R is fixed at 10 and the dominant dilution effect is He (four depositions with He increasing from 0 to 90), and the other in which R is fixed at 80 and the dominant dilution effect is H$_2$ (two depositions with He = 0, 20).

Figure 2.17 shows the phase diagrams for the same set of samples. The following two observations can be made. (i) Dominant H$_2$-dilution (He=0) and He dilution (R=10) generate similar a → a transition thicknesses, even though higher deposition rates are achieved with dominant He dilution. (ii) A larger a → a transition thickness and improved properties are possible (without sacrificing deposition rate) by using He-dilution to suppress to a → (a+μc) transition thickness, enabling a larger R value, as shown for the deposition with R=80 and He=20 in Figs. 2.15 and 2.17. The larger amplitude of d$_s$ for this deposition in Fig. 2.15 appears to be due to a lower initial nucleation density, possibly a result of longer precursor diffusion length on the substrate surface.
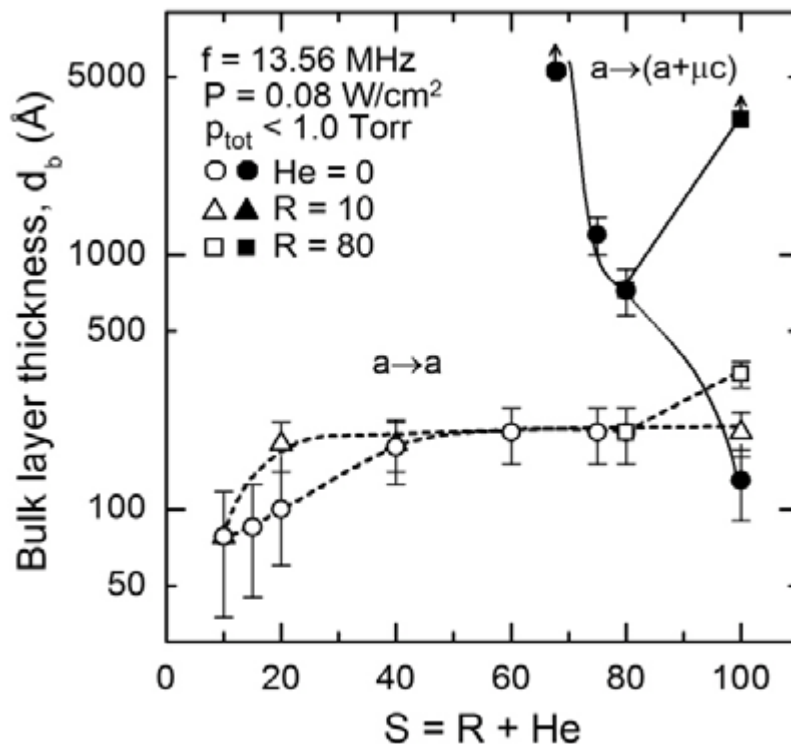
Fig. 2.17: Deposition phase diagrams plotted versus the combined [H$_2$+He]-dilution ratio S=R+He={[H$_2$]+[He]} /{[SiH$_4$]+[GeH$_4$]} for the set of Si$_{1-x}$Ge$_x$:H films of Fig. 2.7, prepared in the anode configuration with G=[GeH$_4$]/ {[SiH$_4$]+[GeH$_4$]} = 0.167. The broken lines denote the a → a transitions while the solid lines denote the a → (a+μc) transitions.

16

Summary

$Si_{1-x}Ge_x$:H phase diagrams have been developed comparing anode and cathode electrode configurations and the role of low-energy ion bombardment. These comparisons show that the a $\rightarrow$ (a+µc) transitions shift to higher R for films deposited on the cathode. This opens a narrow window leading to a $\rightarrow$ a transitions at much higher bulk thicknesses, suggesting significant increases in precursor surface diffusion for a-$Si_{1-x}Ge_x$:H deposited at the cathode. $Si_{1-x}Ge_x$:H phase diagrams versus R have been developed under cathode deposition conditions for different flow ratios G. This comparison shows that: i) the a $\rightarrow$ a transitions shift to higher thicknesses with increasing R right up to the a $\rightarrow$ (a+µc) transitions, indicating the beneficial effect of H on precursor surface diffusion under all alloying conditions and ii) the dielectric function width parameter Γ decreases with increasing R up to the a $\rightarrow$ (a+µc) transition, indicating improvedshort-range order in the films. Additionally, for anode depositions with substrate temperature as a variable have indicated that the a $\rightarrow$ (a+µc) transition shifts to lower R with increasing temperature. In spite of this behavior, the a $\rightarrow$ a transitions for the highest dilution R before crossing the a $\rightarrow$ (a+µc) occur at increasingly higher bulk layer thickness with increasing temperature. This result indicates modest improvements in film quality, although not to the extent seen through the change in the electrode configuration from anode to cathode.   Finally, the presence of He in a-$Si_{1-x}Ge_x$:H has been shown to shift the a $\rightarrow$ a roughening transition to higher bulk layer thicknesses, indicating enhanced surface diffusion, but the effect is much weaker than for H_2 dilution.   Similarly, He has been shown to suppress microcrystallite formation, shifting the a $\rightarrow$ (a+µc) transition in thin film $Si_{1-x}Ge_x$:H to higher bulk layer thickness, extending the protocrystalline regime.

2.2 Dielectric Functions of a-Si$_{1-x}$Ge$_x$:H versus Ge Content, Temperature, and Processing: Advances in Optical Function Parameterization

Overview

Parameterizations of the optical functions of semiconductors have three important applications [2.11]. First, they can be used in performance simulations of optoelectronic devices that involve photon collection -- solar cells being an important example. In this case, the effects of deviations in the optical band gaps for the component i-layers on the measured quantum efficiency can be predicted in order to assess fabrication tolerances. Second, parameterizations can be applied in fitting transmittance, reflectance, ellipsometric, or optical quantum efficiency spectra acquired on multilayer stacks that include one or more of the layers. By using parameter databases, one can extract wavelength-independent parameters directly such as thicknesses, compositions (or preferably optical gaps), and even temperature that directly assist in evaluating the processing and material properties of interest in devices. Finally, parameterizations can provide succinct information useful for correlating with other properties for indirect assessment of the performance of the materials. For example, we have found that an important parameter is the energy width of the resonance in the dielectric function which provides information on defect density and disorder presumably due to its proportionality to the excited state relaxation rate.

We have applied an advanced model to analyze the dielectric functions $\varepsilon = \varepsilon_1 + i\varepsilon_2$ of amorphous silicon-germanium alloys (a-Si$_{1-x}$Ge$_x$:H) (i) as a function of alloy content x by varying the flow ratio $G = [GeH_4]/\{[SiH_4]+[GeH_4]\}$ in plasma-enhanced chemical vapor deposition (PECVD), and (ii) for the first time as a function of the measurement temperature T_m by cooling the newly-deposited film. All ε spectra (1.5 – 4.5 eV) have been measured by spectroscopic ellipsometry (SE) either in real time during deposition or in situ post-deposition in order to avoid surface contamination. From the resulting extensive database, the optical properties of the alloys can be predicted for any value x and T_m within the ranges of the database. Such a capability is expected to be useful, for example, in real time control of optical gap in the PECVD process and in predicting the quantum efficiency of multijunction a-Si:H-based solar cells versus operating temperature. The effect on the database of other deposition parameters such as the electrode configuration and the H$_2$-dilution ratio $R = [H_2]/\{[SiH_4]+[GeH_4]\}$ have also been explored. The latter two studies provide useful insights into materials properties that can be extracted from a single spectroscopic measurement performed in real time during PECVD. For example, the energy width of the resonance in ε correlates closely with the precursor surface diffusion characteristics observed throughout growth -- both determined from real time SE. This result indicates that short-range ordering in the film is improved when surface diffusion is promoted.

Experimental Details:

Deposition Process

The primary a-Si$_{1-x}$Ge$_x$:H series explored in this study and presented to exemplify our approach was prepared by PECVD on crystalline Si (c-Si) wafers from gas flows of SiH$_4$, GeH$_4$, and H$_2$. Most parameters were set for optimum a-Si:H [2.1] including a H$_2$-dilution ratio of $R = [H_2]/\{[SiH_4]+[GeH_4]\} = 10$, a substrate temperature of $T_s = 200°C$, a minimum plasma power of $P = 0.08$ W/cm^2, and a partial pressure of [SiH$_4$]+[GeH$_4$] of p ~ 0.05 Torr. The gas flow ratio

$G = [GeH_4]/\{[SiH_4]+[GeH_4]\}$ was set at values from 0 to 0.167, corresponding to an optical gap range at 20°C of 1.3 to 1.8 eV, which is of interest for multijunction solar cells [2.12]. To improve the growth and optical characteristics of the lowest gap a-Si$_{1-x}$Ge$_x$:H, but at the expense of those of pure a-Si:H, the substrate was mounted on the cathode with a dc self-bias of $\sim$ –20 V [2.9].

This a-Si$_{1-x}$Ge$_x$:H series was measured in real time by spectroscopic ellipsometry (SE), and the structural evolution was determined throughout the growth of 0.2 - 0.8 μm thick films [2.1]. In addition, the dielectric function at a measurement temperature of $T_m=T_s=200°C$ was deduced in a numerical inversion process that requires the bulk and surface roughness layer thicknesses. This inversion was performed on data collected after complete coalescence and surface smoothening when the bulk layer is $\sim$ 150-300 Å thick. For this first series with variable G and R=10, selected samples were cooled from $T_m=T_s=200°C$ after deposition, and the dielectric function was deduced by SE as a function of T_m, applying numerical inversion using the bulk and surface roughness layer thicknesses from the end of deposition. The calibration that provides the true T_m from a thermocouple reading is performed using a c-Si wafer and a similar cooling cycle, applying SE to deduce the critical point energies which are known functions of T_m [2.13].

For the first series, Fig. 2.18 shows the variation in x and a measure of the optical band gap E_g as functions of G. The former is obtained ex situ by x-ray photoelectron spectroscopy and the latter in
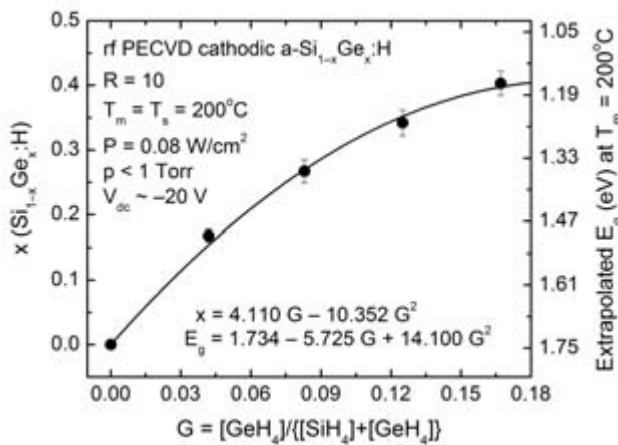
Fig. 2.18: (Above) Alloy content x in a-Si$_{1-x}$Ge$_x$:H thin films and their optical band gaps at $T_m=T_s=200°C$ as a function of the flow ratio $G=[GeH_4]/\{[SiH_4]+[GeH_4]\}$ using a fixed ratio $R=[H_2]/\{[SiH_4]+[GeH_4]\}=10$ and a cathodic electrode configuration. The gaps are from extrapolations of $\varepsilon_2^{1/2}$ to zero ordinate using ε_2 obtained by inversion at thicknesses in the range of 150-300 Å.
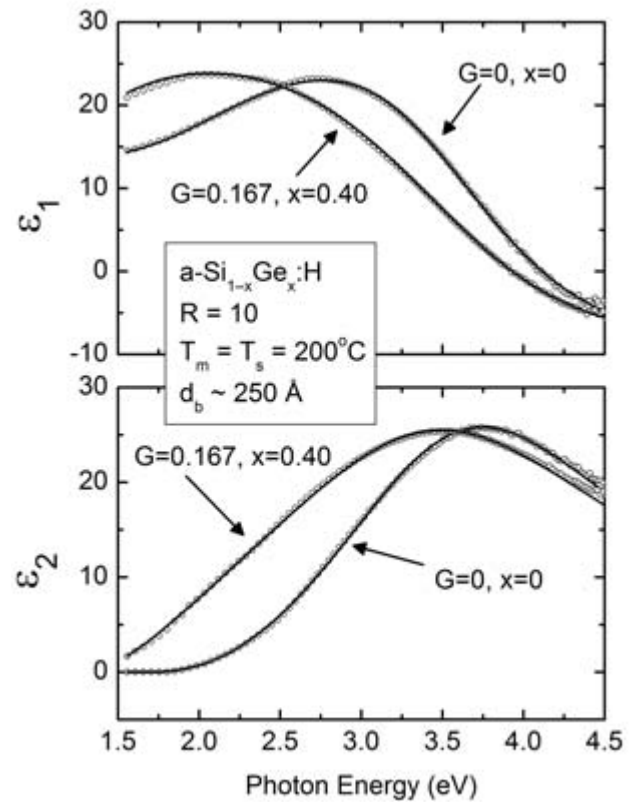
Fig. 2.19: (Above, right) Examples of fits (solid lines) to dielectric function spectra (points) of a-Si$_{1-x}$Ge$_x$:H measured at $T_m=T_s=200°C$ from films of the series of Fig. 2.18 (R=10, cathodic deposition) at the extremes of the alloy range. These spectra were deduced by inversion of real time SE data at bulk layer thicknesses in the range 150-300 Å.

real time by SE, applying an extrapolation of $\varepsilon_2^{1/2}$ versus photon energy E, assuming parabolic bands and a constant-dipole matrix element (CD-ME, Cody's method) [2.14]. It should be noted that the T_m=200°C gap of 1.17 eV at G=0.167 corresponds to a T_m=20°C Tauc gap of 1.28 eV, assuming parabolic bands and a constant-momentum matrix element (CM-ME) [2.8].

    Second and third deposition series were performed at the anode with fixed G values at the extrema of 0 and 0.167 in order to explore the effect of the electrode configuration, but now as a function of the H_2-dilution ratio R. Under the G=0 conditions, the optimum a-Si:H is obtained at R=10 just before the amorphous-to-mixed-phase transition [a → (a+μc)] for a thick film (>0.5 μm). Here the amorphous phase roughening transition (a→a) thickness is maximum and the observed solar cell performance is the highest [2.1]. In contrast, the thick film a → (a+μc) transition for G=0.167 anodic depositions occurs at R=70.   A fourth deposition series was performed at the cathode with G also fixed at 0.167 as a function of R from 10 to 140 -- under otherwise identical conditions as the first series. This variation in R leads to a significant improvement in the growth and optical characteristics for the a-Si$_{1-x}$Ge$_x$:H as the thick film a → (a+μc) transition is approached. For this fourth series, the a → (a+μc) transition occurs at R~95, which identifies the optimum a-Si$_{1-x}$Ge$_x$:H growth conditions achieved thus far in our real time SE studies, as indicated by the largest precursor surface diffusion length [2.9] and the highest degree of short-range order (see below).

Optical Model

    The most popular dielectric function parameterization for amorphous semiconductors is based on a model for ε_2 that includes a parabolic-band, CM-ME expression $G_M(E)=(E-E_g)^2/E^2$ at near gap energies, evolving to a Lorentz oscillator $L(E) = AE_0\Gamma E/[(E_0^2-E^2)^2+\Gamma^2E^2]$ at high energies, including a total of four free parameters [2.15].   Then ε_1 is given by an analytical Kramers-Kronig integration of $\varepsilon_2(E)=G_M(E)L(E)$; $E>E_g$ and ε_2=0; $E<E_g$.   In fact, in determining ε_1, a fifth free parameter is introduced, the constant contribution to the dielectric function ε_∞. More recent research has shown that a similar approach that adopts instead a CD-ME formalism $G_D(E) = (E-E_g)^2/[(E-E_g)^2+E_p^2]$ at near gap energies provides a superior fit with improved internal consistency [2.11, 2.16].   Thus, in order to couple the CD-ME expression to the Lorentz oscillator, the additional parameter E_p is required that controls the transition energy between the near gap absorption onset and the Lorentz oscillator behavior. The extra parameter of the CD-ME approach is compensated through improved consistency that allows fixing ε_∞=1. In contrast, for the CM-ME, ε_∞ decreases with increasing x, becoming negative for the larger values of x, unphysical behavior [2.11]. Fig. 2.19 shows examples of the experimental data and fits to the CD-ME approach for cathodic a-Si$_{1-x}$Ge$_x$:H prepared with the extremes of G=0, 0.167, and with R=10.

Results and Discussion

    Figure 2.20 depicts data plotted versus x in the best fit variable parameters in the CD-ME formula with ε_∞ fixed at 1 (solid points).   In addition, the resonance energy E_0 is found to be constant at 3.736 eV within the confidence limits, and so is also fixed. The samples analyzed to obtain the results in Fig. 2.20 were from the first deposition series using the cathodic configuration with R fixed at 10. The results are characteristic of T_m=T_s=200°C and also a film thickness of ~150 - 300 Å. The variations with x of interest include the expected, nearly linear decreases in the fitted

E_g (distinct from the $\varepsilon_2^{1/2}$ extrapolation for E_g in Fig. 2.18) and transition energy E_p. Of equal interest is the monotonic increase in the width parameter Γ. This is attributed to a reduction in the excited state lifetime due to increased disorder with alloying. In fact, assuming electron and hole velocities υ characteristic of the E_1 excited states of c-Si and using the simple expression for the mean free path $L = h\upsilon/\Gamma$ (h: Planck's constant), a $2 \rightarrow 3$ eV dielectric function width can be ascribed to a $5 \rightarrow 4$ Å mean free path, which is consistent with the lack of long-range ordering. Thus, the width Γ is a very useful parameter for assessing short-range order, also found to correlate with the Urbach tail width [2.11]. In fact, its usefulness lies in its accessibility in a real time measurement.
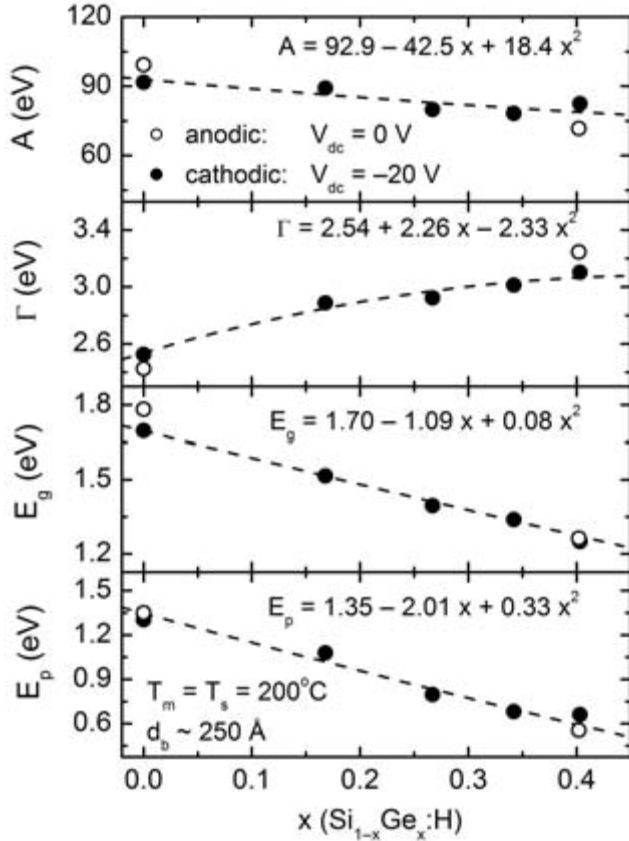
Fig. 2.20: Dielectric function parameters versus a-Si$_{1-x}$Ge$_x$:H alloy composition x at T$_m$=T$_s$=200°C deduced in fits such as those of Fig. 2.19 for the series of depositions of Fig. 2.18 (R=10, cathodic deposition, closed circles). Also shown are the corresponding results for films deposited on the anode under otherwise identical conditions. The dielectric functions fitted in this study were deduced by inversion at bulk layer thicknesses of ~150-300 Å. The following parameters were fixed in the analysis: $\varepsilon_\infty = 1$ and $E_0 = 3.74$ eV.
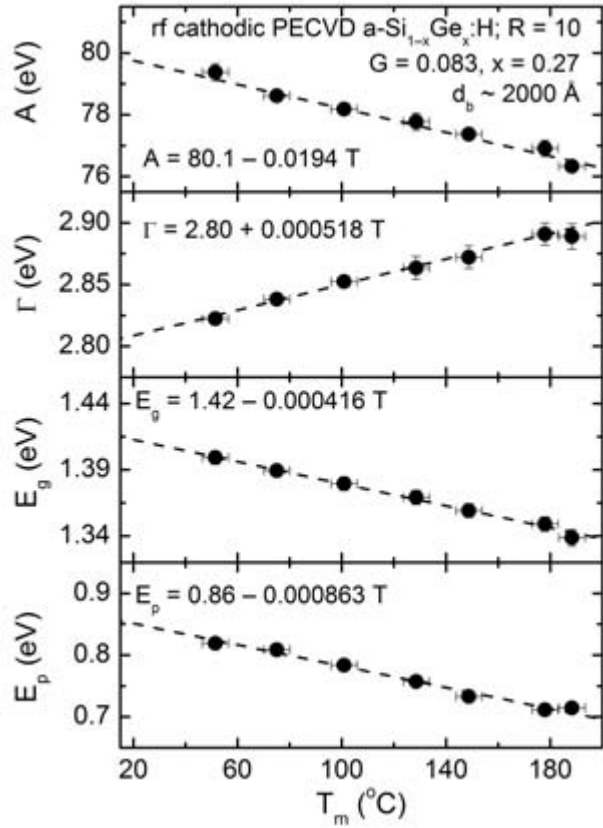
Fig. 2.21: Dielectric function parameters versus measurement temperature T$_m$ obtained in fits such as those of Fig. 2.19 for an a-Si$_{1-x}$Ge$_x$:H alloy with G=0.083 prepared at the cathode. The dielectric functions fitted in this study were deduced by inversion using thicknesses deduced for the final film. The following parameters were fixed in the analysis: $\varepsilon_\infty = 1$, $E_0 = 3.77$ eV. The small difference in E_0 compared with that of Fig. 2.20 is attributed to the different stage of the growth process.

21

Figure 2.20 also shows results at $T_m=T_s=200°C$ for selected depositions from the second and third series using the anodic configuration also with R=10 (open points) for comparison with the otherwise identical cathodic series in the same figure (solid points). An observation of interest is that the conversion from the anodic to cathodic configuration leads to a reduction in Γ for the a-Si$_{1-x}$Ge$_x$:H, i.e., an improvement in order, whereas the conversion for pure a-Si:H leads to an increase in Γ. This is precisely the same behavior as is observed in the a$\rightarrow$a roughening transition: an increase upon conversion to the cathodic configuration for a-Si$_{1-x}$Ge$_x$:H, but a decrease upon conversion for pure a-Si:H [2.9]. Evidently there is a close connection between precursor surface diffusion length and the resulting short-range order in the film. In fact, in previous studies, the narrowest width of Γ=2.0 eV at T_m=20°C has been obtained from protocrystalline Si:H which exhibits no a$\rightarrow$ a roughening transition throughout the growth of a 0.5 μm thick film [2.1,2.11].

Figure 2.21 shows how the dielectric function parameters vary with temperature, as obtained during cooling of the a-Si$_{1-x}$Ge$_x$:H prepared in the cathodic configuration with G=0.083 and R=10 (sample of the first series). In this study, ε_∞ =1 as usual and the resonance energy is fixed as well (E_0=3.773 eV, appropriate for the thicker films, independent of x). All other parameters exhibit linear variations with T. Specifically, the optical gap E_g and transition energy E_p decrease with slopes of -4.2×10^{-4} eV/°C and -8.6×10^{-4} eV/°C, and the width Γ increases with a slope of 5.2×10^{-4} eV/°C. As shown in Fig. 2.22, there are relatively weak variations in the slopes with T_m that can be averaged assuming linear functions of x. For example, the variations in the slopes of E_g and E_p with x are consistent: at larger x the slopes are larger in magnitude apparently due to stronger electron-phonon interactions in the alloys.

As further evidence for the significance of the parameterization, in particular to extract the width of the resonance, Fig. 2.23 shows fitting results similar to those of Fig. 2.20, but for the fourth deposition series involving a variation in R under cathodic conditions with G=0.167. The vertical line indicates the a$\rightarrow$(a+μc) transition for a 0.5 μm thick film. On average the gap increases by ~0.05 eV with the increase in R up to the a$\rightarrow$(a+μc) transition, an increase typical of that for G = 0 depositions versus R. In addition, Γ decreases from 3.1 eV to 2.8 eV with the increase in R from 10 to 100. For R=125 and 140, the saturations in E_g and Γ are likely to be due to the development of crystallites in the thin films (~150-300 Å). The decrease in Γ for R≤100 also tracks the corresponding increase in the a$\rightarrow$a roughening transition thickness and even extends into the protocrystalline regime of the thin film (to R=100), i.e., beyond the thick-film a$\rightarrow$(a+μc) transition.

Summary

In this section, we have described a recently-developed parameterization of the optical properties of amorphous semiconductors and its application to a-Si$_{1-x}$Ge$_x$:H alloys as a function of the alloy content x and the temperature T_m. Results at T_m=200°C in Fig. 2.20 (solid points) which define intercepts, along with the slopes in Fig. 2.22 allow one to apply SE for simultaneous in situ composition, optical gap, and temperature determination (with ε_∞ = 1 and E_0=3.75 eV). The same set of results can be used to predict the effect of optical gap variations and operation temperature changes on the quantum efficiency of multijunction solar cells. The results in Fig. 2.20 (open points) and Fig. 2.23, show how variations in electrode configuration and H$_2$-dilution influence the results. Since all trends versus T can be approximated as linear functions, it is straightforward to predict the effects of combinations of variables. Finally, the parameter Γ, the dielectric function
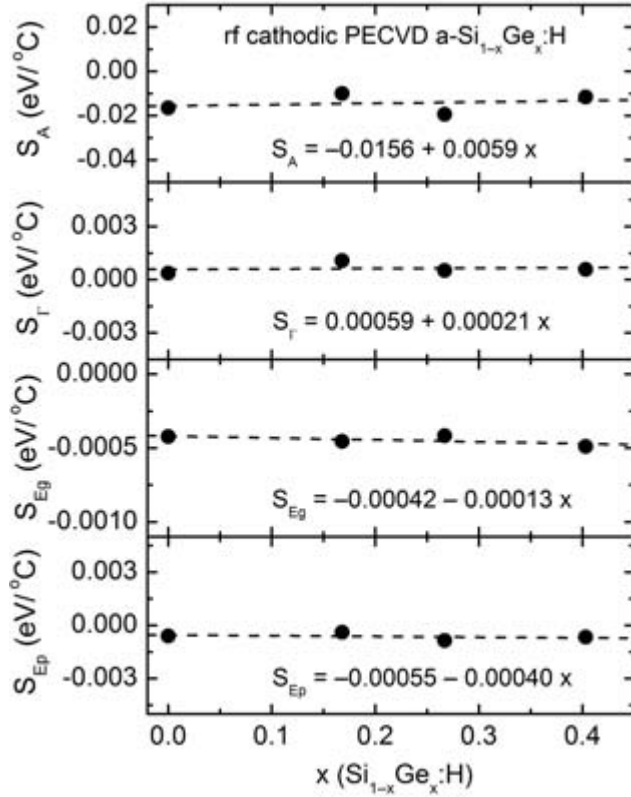
Fig. 2.22: The slopes that describe the linear variation of the dielectric function parameters versus measurement temperature T_m determined as shown in Fig. 2.21. Results are given for four a-$Si_{1-x}Ge_x$:H alloys of different composition x. In the overall analysis, the following parameters were fixed: $\varepsilon_\infty = 1$, $E_0 = 3.75$ eV.
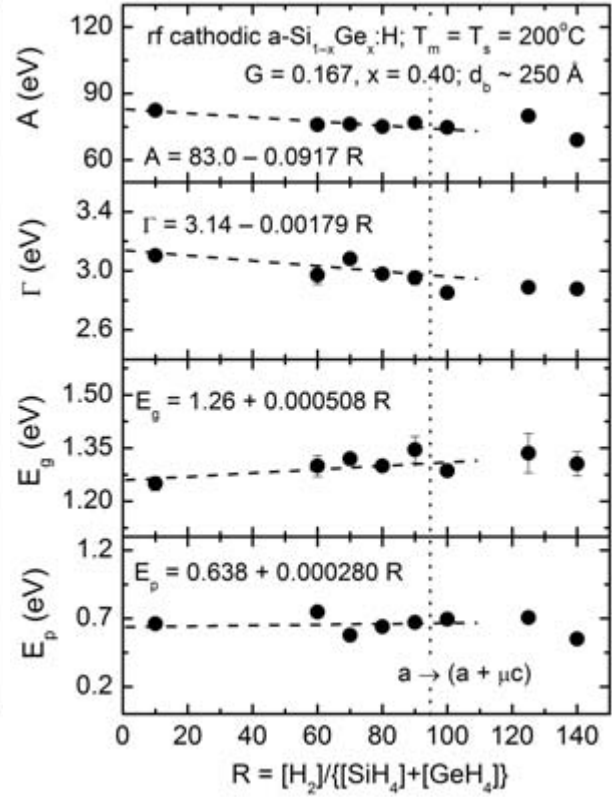
Fig. 2.23: Dielectric function parameters for a-$Si_{1-x}Ge_x$:H alloys versus H_2-dilution ratio R=[H_2]/{[SiH_4]+[GeH_4]} at $T_m=T_s=200$°C deduced in fits such as those of Fig. 2.19 for a series of depositions with G=0.167 prepared at the cathode. The dielectric functions fitted in this study were deduced by inversion at bulk layer thicknesses ~150-300 Å. The following parameters were fixed: $\varepsilon_\infty = 1$, $E_0 = 3.74$ eV.

resonance width, shows clear correlations with the amorphous roughening transition thickness in the growth process, an indication that enhanced surface diffusion, which is proposed to be reflected in a larger a→a roughening transition (see next section), results in improved short-range order in the film under all the conditions of growth explored for a-$Si_{1-x}Ge_x$:H, including variations in G=[GeH_4]/{[SiH_4]+[GeH_4]}, R=[H_2]/{[SiH_4]+ [GeH_4]}, and electrode configuration.

2.3 Model for Amorphous Roughening Transition in Amorphous Semiconductor Deposition

Overview

Real time spectroscopic ellipsometry (SE) results have demonstrated the existence of three regimes of surface roughness evolution during amorphous semiconductor thin film growth by plasma-enhanced chemical vapor deposition (PECVD) [2.1]:
   (i)   smoothening (or coalescence) of initial nucleation-generated clusters;
   (ii)   stable surface until a critical thickness; and
   (iii) roughening of the film beyond the critical thickness.
It should be emphasized that throughout these regimes the films remain fully amorphous.

Hydrogenated amorphous silicon (a-Si:H) thin films exhibiting the highest electronic performance also reveal in regime (i) the largest surface smoothening magnitudes and rates during coalescence, as well as in regime (ii) the smoothest, most stable surfaces throughout the growth of thick films [2.1]. In fact, for these highest quality films, the transition between regimes (ii) and (iii), denoted the a $\rightarrow$ a roughening transition, is not observed, presumably because it occurs at thicknesses greater than the final film thickness (typically > 0.5 μm). Deterioration of electronic properties is correlated with a reduction in the magnitude and rate of smoothening in regime (i) and an increase in the roughness thickness in regime (ii). Deterioration is also accompanied by a shift in the a $\rightarrow$ a transition to lower thicknesses. In fact, regimes (i) and (ii) may disappear when the electronic quality is sufficiently poor, e.g., under conditions combining high plasma power, little or no H_2-dilution, and low temperatures. In this section, insights into the three regimes listed above will be obtained by applying a simple, one-dimensional (1-D) continuum model of film growth. This 1-D continuum model of surface profile evolution adopts an initial condition designed to be consistent with the nucleation characteristics measured by real time SE. Good agreement between the experimental results and model calculations support the contention that optimum electronic qualities of the films are associated with weakly reactive surfaces and long lifetime precursors that lead to large precursor surface diffusion lengths.

Results and Discussion

Experimental Data

Real time SE has been performed using a rotating-compensator multichannel ellipsometer [2.2] in order to study the evolution of the surface roughness thickness for a-Si:H films fabricated by PECVD on crystalline silicon (c-Si) wafer substrates. Figure 2.24 (main part) depicts examples from a high-pressure, high-rate PECVD series for which all films remain amorphous throughout growth [2.17]. The substrate temperature T, rf plasma power P, and total pressure p were fixed at the following values: T = 200°C, P = 0.72 W/cm^2, and p = 3 Torr, respectively. The H_2-dilution ratio R=[H_2]/[SiH_4], was set at four different values ranging from 15 to 60, leading to deposition rates ranging from 18 Å/s (R=15) to 6.6 Å/s (R=60). These data demonstrate significant changes in the surface roughness evolution with R and clearly exhibit all three regimes described above. The a $\rightarrow$ a roughening transition thickness as a function of R is included in the deposition phase diagram shown in the inset. This diagram also includes the amorphous-to-(mixed-phase microcrystalline) transition thickness obtained from depositions with R set from 70 to 100. The three regimes can be
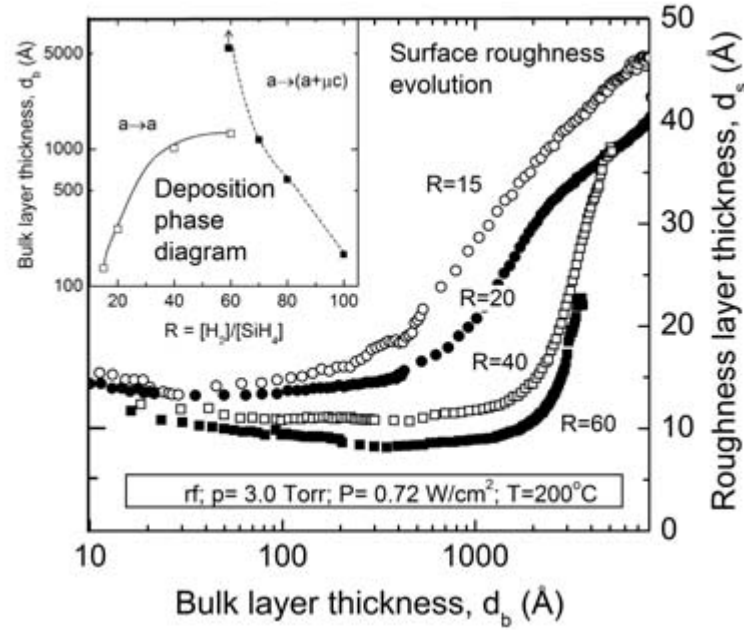
Fig. 2.24: Surface roughness evolution for a series of a-Si:H films prepared by high-pressure, high-rate PECVD using the following fixed parameters: substrate temperature, T=200°C; rf plasma power, P=0.72 W/cm^2; and total pressure, p=3 Torr. The H_2-dilution level R=[H_2]/[SiH_4] is set at different levels from 15 to 60. (Inset) Phase diagram compiled from Si:H films deposited under the same conditions over a wider range of R, including the roughening transition in the amorphous regime [a → a; solid line] and the amorphous-to-(mixed-phase microcrystalline) roughening transition [a→(a+µc); broken line].
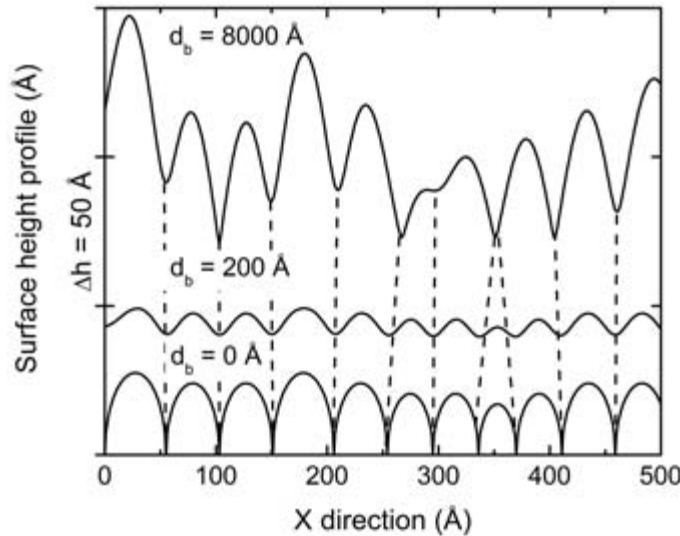
Fig. 2.25: The surface height profile at bulk layer thicknesses of d_b=0, 200, and 8000 Å for a 1-D continuum model of film growth that includes smoothening due to surface diffusion and roughening due to an atomic size effect. An initial mean cluster radius of 24 Å is used to simulate initial nuclei, and the diffusion length is assumed to be λ_0=45 Å.

better understood through a continuum surface diffusion model for the surface roughness evolution to be discussed briefly in the next subsection.

Surface diffusion theory

Continuum models have been applied to study both physical and chemical vapor deposition processes [2.18-2.21]. In such studies, the dynamics of the surface roughness morphology are often investigated by means of linear stability analysis. In this analysis, the surface roughness is considered to be a small perturbation from a perfectly flat surface (or from a straight line profile in a 1-D simulation), allowing one to linearize the differential equation that describes the surface profile evolution. Then the time evolution of the amplitude $h(\lambda, t)$ of a surface perturbation with spatial period λ in the in-plane direction can be described simply as

$$h(\lambda,t) = h_0 \exp[\omega(\lambda)t], \tag{2.1}$$

where ω is a decay rate that depends on the pertinent physical mechanisms of growth. In fact, the relevance of this approach has been tested in real time SE studies of a-Si:H growth on microscopically rough transparent conducting oxide surfaces having well defined in-plane periods [2.22]. In depositions on such surfaces, the substrate-induced roughness is observed to decay exponentially with time in accordance with Eq. (2.1). In general, the decay rate ω in Eq. (2.1) can be described as a polynomial function of spatial frequency $k=2\pi/\lambda$ so that [2.23]

$$\omega(\lambda) = \Sigma_m (a_m/\lambda^m) . \tag{2.2}$$

In this model, the specific physical mechanisms that impact the evolutionary development of the surface determine the polynomial terms present as well as the polynomial coefficients a_m. The three regimes listed above can be understood qualitatively from Eqs. (2.1) and (2.2) in the following general way. Low amplitude surface modulations of period λ less than some critical value λ_0 are unstable and decay versus time t (or thickness) according to Eq. (2.1), where $\omega(\lambda)<0$ for $\lambda<\lambda_0$. This behavior applies to short period surface modulations associated with the coalescence of initial nuclei. Features with $\lambda>\lambda_0$, such that $\omega(\lambda)>0$, are enhanced. This behavior applies to the later stage characteristics of growth, i.e., the a $\rightarrow$ a transition, in which case statistical fluctuations in nuclei height and radius ultimately lead to larger scale structures through space-filling competition among neighboring columns [2.24].

In one specific model [2.18,2.19], the smoothening effects can be attributed to capillarity-driven surface diffusion that exhibits a negative term in $\omega(\lambda)$ given by $\omega_4(\lambda) = -16\pi^4 D_e \lambda^{-4}$, where $D_e= \Omega^2\varepsilon\sigma_sD_s/k_BT$, and Ω, ε, σ_s, D_s, and k_BT are the atomic volume, number of atoms per area, surface energy density, surface diffusivity, and thermal energy, respectively. The roughening is an atomic size effect that exhibits a positive term in $\omega(\lambda)$ given by $\omega_2(\lambda) =4\pi^2\rho J \lambda^{-2}$, where ρ is the atomic radius and J is the deposition flux. For this effect, regions where the surface exhibits positive or negative curvature receive a deposition flux J greater than or less than J, respectively, as in a shadowing effect. Then the diffusion length corresponds to the specific period that is stable; i.e., $\lambda_0 = (4\pi^2D_e/\rho J)^{1/2}$, since this period is too large to be dampened by diffusion. Many additional useful features of this model have been described previously [2.18,2.22].

Simulations of surface roughness evolution

In applying the specific model described above, the surface perturbation is associated with the initial nucleation process. An appropriate 1-D model for the surface profile following nucleation consists of a series of contacting semicircles that simulate clusters, with radii determined by one Gaussian distribution, and the elevation of the semicircle diameter from the surface determined by a second Gaussian distribution [2.22]. This one dimensional surface profile is then allowed to evolve during film growth using the approach described in the previous subsection, as shown in Figure 2.25. As seen in the figure, the short-period perturbations in the initial surface profile arising from nuclei contact smoothen out during film growth in the initial stages. Generally with time (or thickness), however, the surface profile coarsens as can be seen by the disappearance of the smallest cluster in Fig. 2.25 and the development of superclusters encompassing many smaller clusers. The superclusters evolve from the statistical distribution of initial cluster heights and spacings. From the surface profile extracted at any point during film growth as in Fig. 2.25, the root-mean-square value of the surface roughness layer thickness, d_{rms}, can be deduced and converted to the surface roughness layer thickness, d_s, determined from real time SE using the expression $d_s = 3$ Å $+ 1.5 \ d_{rms}$ (Å). This expression has been obtained from a correlation of real time SE and atomic force microscopy measurements of the same surfaces [2.25].

As an example of the final results, Figure 2.26 shows a fit (solid line) to the surface roughness evolution determined by real time SE for the R=40 a-Si:H film from the series of Fig. 2.24. Also shown are the simulated roughness evolution curves obtained using the same initial nucleation profile, but assigning different values to the surface diffusion length from 12 to 160 Å, above and below the best fit value of 45 Å. Figure 2.27 summarizes the best simulation results plotted versus R for all four depositions of the series of Fig. 2.24. The simulations suggest that all the films in this series have a mean cluster radius ~ 20 Å which describes the contact thickness; however, λ_0, ranges from 28 Å for R=15 to 50 Å for R=60, which accounts for the significant variations with R. As shown in the figure, a linear correlation is found between the best fit surface diffusion length in the simulation, and the observed a → a transition thickness. The amorphous roughening transition is only sensitive to diffusion lengths above a certain value, however; below this value the roughening begins almost immediately in the deposition process.

Discussion

The full set of roughness evolution simulations reproduce the trends of the experimental data in Fig. 2.24, revealing all three characteristics, namely, coalescence of initial nucleation-generated clusters; a stable surface until a critical thickness; and roughening of the film beyond the critical thickness. Here it is of interest to address whether such a simple model includes a sufficiently strong physical basis to account for the complex growth process of a-Si:H. In support of this simple approach, molecular dynamics studies of surface roughness evolution suggest that the smoothness of a-Si:H arises from a valley filling mechanism whereby diffusing precursors preferentially incorporate in valleys where dangling bonds exist in greater numbers [2.26]. This process is analogous to the valley filling mechanism in the simple continuum model which serves to reduce the surface free energy. The roughening mechanism in the simple model is similarly reasonable based on simple geometric constraints of film growth at the atomic level [2.27]. Furthermore the ultimate conclusion of the present study, namely that the highest electronic quality a-Si:H materials are prepared under conditions that yield the largest surface diffusion length, is consistent with previous
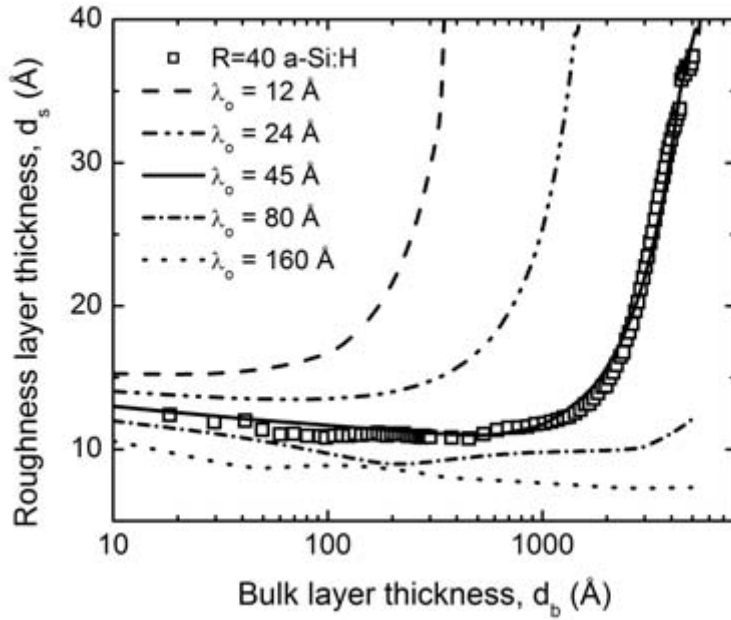
Fig. 2.26: Fit (solid line) to experimental data (squares) for a-Si:H with R=40 from Fig. 2.24 using a the 1-D continuum model of Fig. 2.25. In this model, initial nuclei with a mean radius of 24 Å are assumed, along with a diffusion length of λ_0=45 Å that controls the subsequent evolution as in Fig. 2.25. Additional broken lines are determined using the same initial profile, but with different values of λ_0 from 12 to 160 Å.
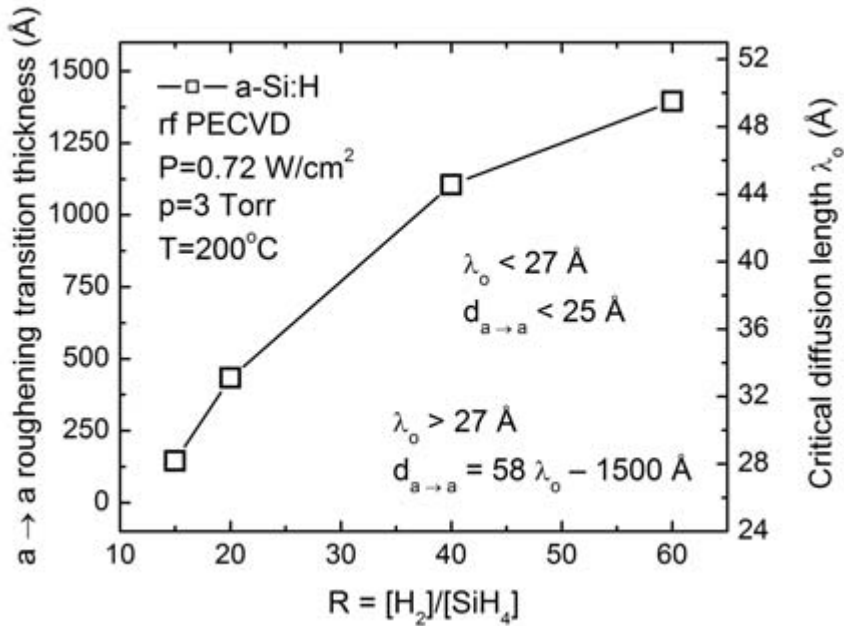
Fig. 2.27: Amorphous roughening transition thickness obtained from real time SE and the critical diffusion length obtained from the 1-D model of Figs. 2.25 and 2.26 plotted as a function of the H_2-dilution ratio R for the series of four a-Si:H samples of Fig. 2.24. Over this range of R, the two ordinate quantities are linearly related.

atomic scale models for growth [2.28,2.29]. In these models, diffusion length is limited either by short lifetime radicals that impinge on the surface from the plasma or by surface defects such as dangling bonds, both of which can lead to bulk defects that degrade electronic properties and stability.

Finally, it is important to note the drawbacks of this model. First of all the simulation is 1-D and should be extended to 2-D for closer quantitative comparisons. Given the complexity of the surface processes, however, it is likely that one can say with confidence only that the surface roughness evolution is reflective of a competition between smoothening driven by diffusion and a roughening process that drives columnar growth in thin films. It is less likely, however, that the mathematical forms of these competing terms are so simply described as in the continuum model. As a result, the greatest confidence should be placed in the trends reported here, rather than the numerical values. One of the complexities of real surfaces is that the diffusivity and hence the diffusion length may depend on the stage of film evolution. In the early stage in which clusters are making contact, the surface is more disordered with higher defect density, and this will limit the diffusion length. After the coalescence process the diffusion length may increase significantly as ordering improves and the defect density decreases. As a result any simple model to describe the full roughness evolution from thin film coalescence to thick film roughening is unlikely to be sufficiently complete for detailed quantitative purposes.

Summary

A 1-D continuum model of surface profile evolution with an initial condition designed to be consistent with nucleation characteristics measured by real time SE has been used in order to better understand the surface roughness evolution of Si:H films that remain amorphous throughout growth. The surface roughness evolution of such films as measured by real time SE exhibits a prominent roughening transition (designated a $\rightarrow$ a) at a critical thickness, and this critical thickness is found to correlate with the electronic properties of the film. In fact, for materials with the best electronic quality, the a $\rightarrow$ a transition occurs at thicknesses beyond that typically deposited for devices. Because of the importance of the a $\rightarrow$ a transition, it has been incorporated into deposition phase diagrams that have been applied successfully to optimize solar cell performance and stability. A key feature of modeling performed here is that the a $\rightarrow$ a transition thickness scales linearly with the precursor diffusion length. As a result such modeling supports previous proposals that optimum electronic film qualities are associated with weakly reactive surfaces, long lifetime precursors, and large precursor surface diffusion lengths.

References

[2.1] R.W. Collins, A.S. Ferlauto, G.M. Ferreira, C. Chen, J. Koh, R. Koval, Y. Lee, J.M. Pearce, and C.R. Wronski, *Solar Energy Mater. Solar Cells* **78**, 143 (2003).

[2.2] I. An, J. Zapien, C. Chen, A. Ferlauto, and R.W Collins, *Thin Solid Films* **455**, 132 (2004).

[2.3] P. Wickboldt, D. Pang, W. Paul, J. Chen, F. Zhong, C. Chen, J.D. Cohen, and D.L. Williamson, *J. Appl. Phys.* **81**, 6252 (1997).

[2.4] For a review see Ref. 1.

[2.5] G. Ganguly, I. Sakata, and A. Matsuda, *J. Non-Cryst. Solids* **200**, 300 (1996).

[2.6] N. J. Podraza, G. M. Ferreira, M. L. Albert, C. R. Wronski, and R. W. Collins, *Proceedings of the 31st Photovoltaics Specialists Conference,* January 2005, Orlando FL (IEEE, Piscataway, NJ, 2005), p. 1393.

[2.7] H. Fujiwara, M. Kondo, and A. Matsuda, *Surf. Sci.* **497**, 333 (2002).

[2.8] R.M. Dawson, Y.M. Li, M. Gunes, D. Heller, S. Nag, R.W. Collins, C.R. Wronski, M. Bennett, and Y.-M. Li, *Mater. Res. Soc. Symp. Proc.* **258**, 595 (1992).

[2.9] N.J. Podraza, G.M. Ferreira, C.R. Wronski, and R.W. Collins *Mater. Res. Soc. Symp. Proc.* **862**, 43 (2005).

[2.10] N.J. Podraza, C.R. Wronski, and R.W. Collins, *J. Non-Cryst. Solids*, in press (2006).

[2.11] A.S. Ferlauto, G.M. Ferreira, J.M. Pearce, C.R. Wronski, R.W. Collins, X. Deng, and G. Ganguly, *J. Appl. Phys.* **92**, 2424 (2002).

[2.12] X. Deng and E.A. Schiff, in: *Handbook of Photovoltaic Science and Engineering*, edited by A. Luque and S. Hegedus (Wiley, New York, 2003), p. 505.

[2.13] P. Lautenschlager, M. Garriga, L. Viña, and M. Cardona, *Phys. Rev. B* **36**, 4821 (1987).

[2.14] G.D. Cody, in: *Semiconductors and Semimetals*, Vol. 21B, edited by J.I. Pankove, Academic, New York (1984), p. 11.

[2.15] G.E. Jellison, Jr., and F.A. Modine, *Appl. Phys. Lett.* **69**, 371 (1996); **69**, 2137 (1996).

[2.16] J. Price, P.Y. Hung, T. Rhoad, B. Foran , and A.C. Diebold, *Appl. Phys. Lett.* **85**, 1701 (2004); N.J. Podraza, G.M. Ferreira, C.R. Wronski, and R.W. Collins *Mater. Res. Soc. Symp. Proc.* **862**, 43 (2005).

[2.17] G.M. Ferreira, A.S. Ferlauto, J.M. Pearce, C.R. Wronski, C. Ross, and R.W. Collins, *Mater. Res. Soc. Symp. Proc.* **808**, 215 (2004).

[2.18] A. Mazor, D.J. Srolovitz, P.S. Hagan, and B.G. Bukiet, *Phys. Rev. Lett.* **60**, 424 (1988).

[2.19] B.J. Palmer and R.G. Gordon, *Thin Solid Films* **158**, 313 (1988).

[2.20] G.S. Bales, A.C. Redfield, and A. Zangwill, *Phys. Rev. Lett.* **62**, 776 (1989).

[2.21] J.J. Thiart, V. Hlavacek, and H.J. Viljoen, *Thin Solid Films* **365**, 275 (2000).

[2.22] R.W. Collins and B.-Y. Yang, *J. Vac. Sci. Technol. B* **7**, 1155 (1989).

[2.23] R.S. Williams, W.M. Tong, and T.T. Ngo, *Mater. Res. Soc. Symp. Proc.* **367**, 273 (1995).

[2.24] R. Messier, *J. Vac. Sci. Technol. A* **4**, 490 (1986).

[2.25] J. Koh, Y. Lu, C.R. Wronski, Y. Kuang, R. W. Collins, T.T. Tsong, and Y.E. Strausser, *Appl. Phys. Lett.* **69**, 1297 (1996).

[2.26] E.S. Aydil, S. Agarwal, M. Valipa, S. Sriraman, and D. Maroudas, *Mater. Res. Soc. Symp. Proc.* **808**, 199 (2004).

[2.27] H.J. Leamy, G.H. Gilmer, and A.G. Dirks, in *Current Topics in Materials Science*, vol. 6 edited by E. Kaldis (North-Holland, Amsterdam, 1980) p. 309.

[2.28] G. Ganguly and A. Matsuda, *Phys. Rev.* B **47**, 3661 (1993).

[2.29] G. Ganguly and A. Matsuda, *J. Non-Cryst. Solids* **164**, 31 (1993).

Task 3. Device Loss Mechanisms

Novel Methodology for characterizing solar cells

The work carried out under Task 3 addressed the mechanisms and defects determining a-Si:H solar cell characteristics that had not yet been clearly resolved. The studies of a-Si:H based solar cells were refined with analysis using a theoretical treatment based on first principles. This treatment takes into account: (i) Shockley-Reed-Hall diffusion/recombination of injected carriers in the bulk and at the p/i interface; (ii) the drift-controlled transport of photogenerated carriers; (iii) the homogeneous densities of defects across the i-layers with continuous distributions of states in the gap; and (iv) potential barriers V_n, V_p due to the high concentration of carriers at the n, p contacts. The results on a wide variety of solar cell structures have been interpreted self-consistently with this model, described in Appendix A, thus allowing solar cell operation to be addressed systematically and a number of misconceptions to be rectified. In obtaining reproducible results for the J_D-V characteristics, the contribution of external contact resistance was taken into account by using a three-probe technique for measuring the currents. In addition the measurements were carried out using a thermoelectric heating/cooling stage with which the temperature of the samples could be controlled to within 0.1°C.

The distinctly different regimes in the dark forward bias current-voltage, J_D-V, characteristics in "state-of-the-art" a-Si:H cells have been utilized as novel powerful probes, not only for investigating these mechanisms, but also for characterizing the defect states in intrinsic a-Si:H materials when the i-layers, p/i interface regions, and p, n contacts are changed in systematic and controlled ways. The dependence of the bulk recombination currents on the thickness and densities of defects in the i-layers has been established. It was found that the "effective diode quality factors" of these currents do not exhibit a constant n, as has been generally considered for over 20 years. The characteristics exhibit voltage dependent "differential diode quality factor" n(V) equal to the inverse of $[kT/q][d(\ln J_D)/dV]$. This result is consistent with the model that predicts such n(V) values as a consequence of a continuous distribution of the states in the gap. The changes in the n(V) characteristics produced by the introduction of light induced defects and from differences in i-layer materials have been utilized in characterizing the corresponding gap states.

The magnitudes of the currents corresponding to the recombination at the p/i interfaces have been directly correlated with the nature of these regions. Their n(V) characteristics are as predicted by the model, independent of voltage with values very close to one. The systematic decreases of p/i recombination have allowed, for the first time, observation of the direct dependence of 1 sun V_{OC} on the thickness of the i-layers. The nature of the limitations on the carrier injection over the potential barriers V_n, V_p and their effects on the 1 sun fill factors have been explored and found to be consistent with the predictions of the model.

The transport and recombination of carriers generated by illumination in the i-layers were also characterized. Superposition between J_{SC}-V_{OC} and J_D-V characteristics is obtained over a wide range of currents and voltages. These results, as well as the nature of the separations obtained at voltages approaching 1 sun $V_{OC,}$ are together consistent with the recombination of carriers and the contributions of V_n, V_p predicted by the model. Such potential barriers can have a large effect on

carrier transport at voltages approaching 1 sun V_{OC} and hence the FF, even though the barriers are much smaller than those commonly postulated as being due to large densities of defects.

The differential diode quality factors, n(V), extracted from the J_D-V characteristics from the wide range of a-Si:H solar cell structures were investigated. From these studies the gap state distributions in the a-Si:H layers, and their difference in the annealed states of the R=10 and R=0 materials was directly and reliably identified. The n(V) characteristics were also applied to results on both R=10 and R=0 materials in studies of the creation of 1 sun light-induced defects and the energy distribution of their gap states. Again distinct differences in the distributions were clearly identified. Characterizing the n(V) spectra after the introduction of light induced defects in the i-layer materials showed that the changes in the density of state distributions in the R=10 and R=0 materials are also distinctly different after degradation.

The dark forward bias current, J_D-V, characteristics have been shown to be a new probe for characterizing carrier recombination, identifying the mechanisms limiting solar cell performance, as well as characterizing the defect states in the i-layers of a-Si:H solar cells. From the bias dependence of the differential diode quality factors, n(V), predictions can be made about the nature of the gap state distributions. The results obtained, in which carrier transport is clearly dominated by bulk recombination, show that there are distinct differences between the two types of i-layers (R=10 and 0) in their distributions of both native and light induced defect states. It has also been reported that in such cell structures with protocrystalline i-layers, degradation kinetics of J_D-V characteristics are obtained with 1 sun illumination that are similar to those due to the recombination with dark forward bias currents. Such "equivalence" has also been found with undiluted a-Si:H i-layers, whereby this is illustrated with results of the J_D-V characteristics shown in Figure 3.1. More importantly this similarity also exists in the differential diode quality factors, n(V), which are directly related to the corresponding energy distributions of the defect states in the i-layer, as is illustrated in Figure 3.2. This ability to create and directly characterize the metastable defect states with dark current voltage characteristics at the same temperatures greatly enhances the ability to characterize their creation as well as the changes in their subsequent relaxation.

In addition a strong similarity is obtained not only in the changes of J_D-V and n(V) characteristics but also in that of the fill factors as illustrated in Figure 3.3. In the experimental apparatus constructed under the present contract, both J_D-V and FF measurements can be carried out at well controlled temperatures for direct correlation, thus allowing direct information to be obtained -- not only about the nature of the metastable defects -- but also about their effects on the fill factors. Such studies have been undertaken in identifying and quantifying the respective contributions of the fast and slow defect states utilizing carrier recombination from dark currents which correspond to 1 sun J_{sc} but also at far forward biases that correspond to high intensity illuminations.
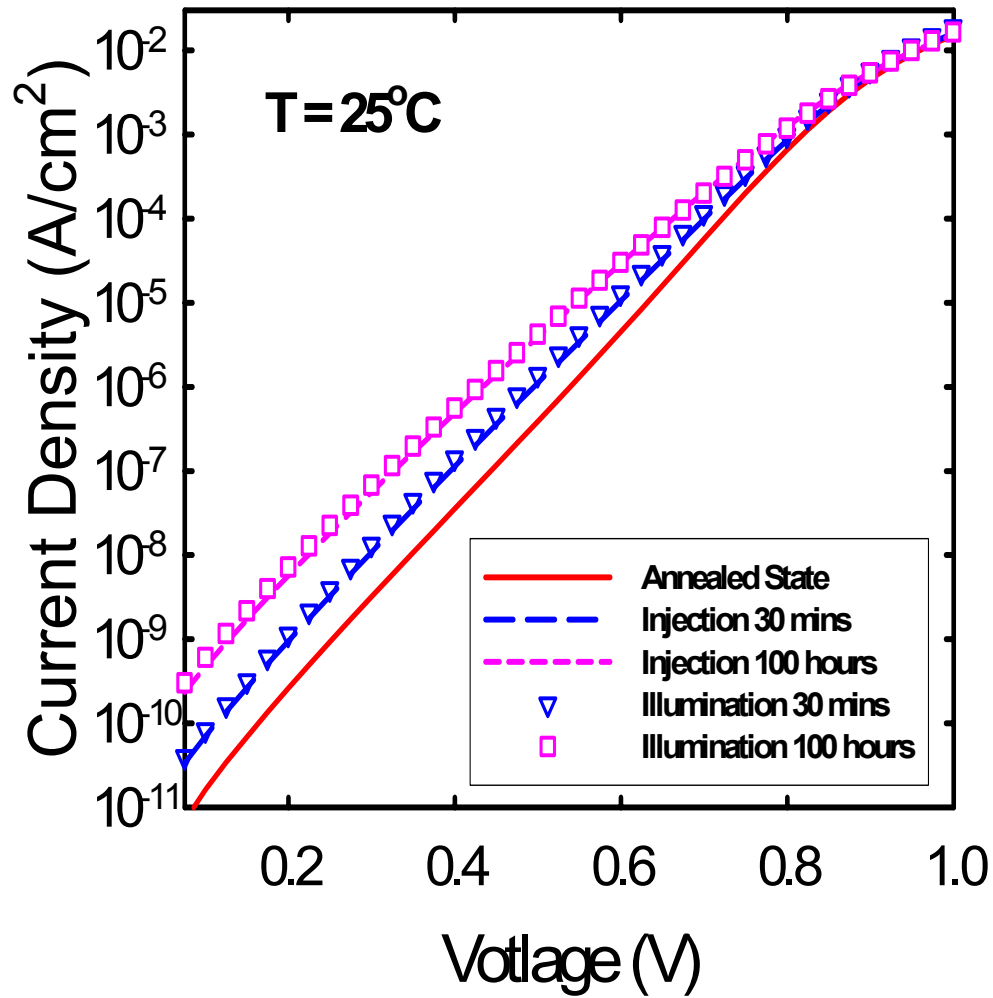
Figure 3.1: J_D-V characteristics for a p-i-n cell with 0.4 μm thick R=0 bulk i-layer and 200 Å R=40 p/i interface layer in the annealed state and after both 1 sun illumination and carrier injection induced degradation. The total recombination current in the case of the carrier injection is equal to J_{sc} of the cell under 1 sun illumination at the annealed state.
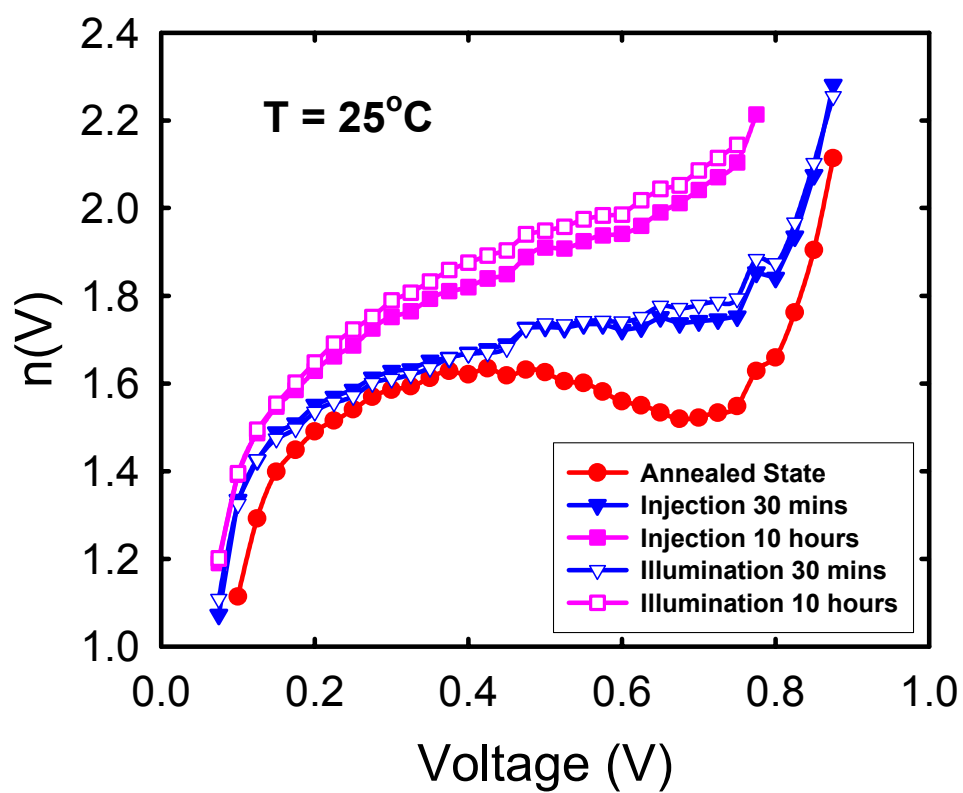
Figure 3.2: n(V) characteristics corresponding to the results of Figure 3.1
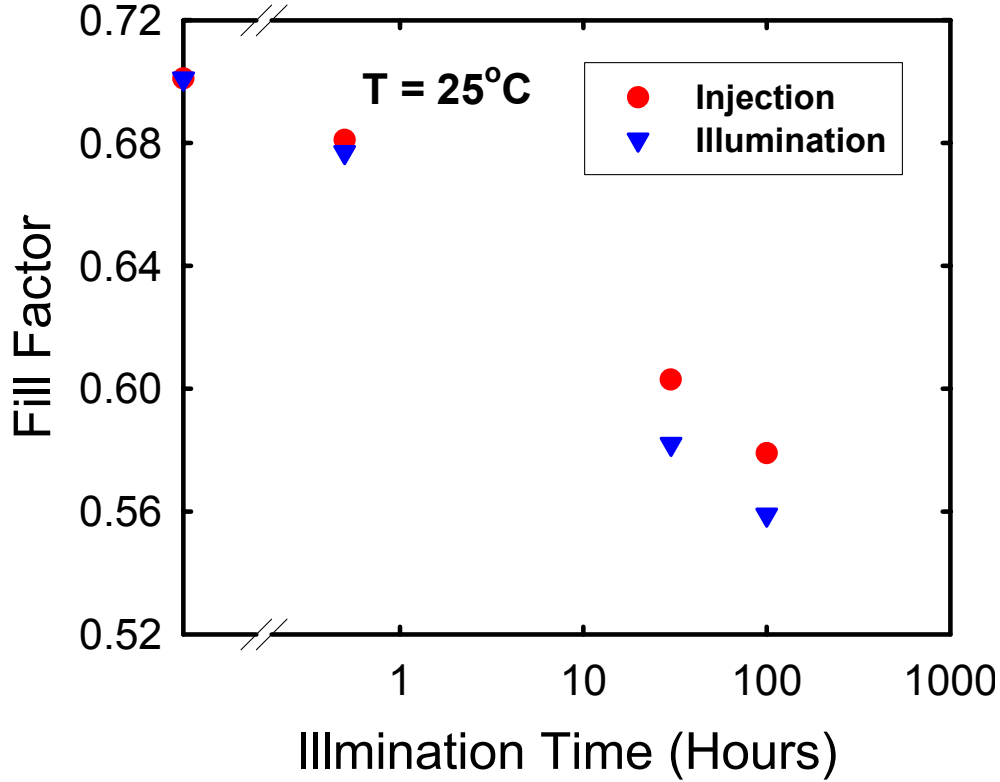
Figure 3.3: Degradation of fill factor with 1 sun illumination and carrier injection for the cell of Figure 3.1. The total recombination current in the case of the carrier injection is equal to J_{sc} of the cell under 1 sun illumination in the annealed state.

A good understanding of the defect states in the intrinsic layers of a-Si:H solar cells and the limitations imposed by different device loss mechanisms on their performance and stability is critical in the optimization of constituent materials as well as cell structures for the further improvement of the already high performance of these solar cells. The conventional measurement techniques and analysis used in such investigations are primarily based on the analysis of light current-voltage (I-V) parameters such as fill factor (FF), open circuit voltage (V_{oc}), and short circuit current (J_{sc}), measured under 1 sun illumination. These parameters are inherently complicated, being affected by the contributions from different parts of the cells such as bulk i-layer, p/i interface as well as n and p contacts, which are difficult to separate and thus to quantify. In order to overcome these limitations, new approaches are being developed. They include the systematic analysis of results obtained on carefully designed cell structures, including forward bias dark current (J_D-V) characteristics, which are extensively used in characterizing crystalline solar cells. In the past, little attention was given to J_D-V characteristics of a-Si:H based solar cells because of the reported lack of correlation between light and dark I-V's as well as the reported predictions by the defect pool model for the presence of very high densities near the n and p contacts and non-uniform distributions of defect states across the i-layer. More recently however, equivalence between carrier recombination in the J_D-V and light I-V characteristics has been established from the superposition between J_{sc}-V_{oc}

and J_D-V characteristics over a wide range of illumination intensities [3.1,3.2].   It has also been shown that in solar cells with high quality materials and optimized cell structures, the defect state densities are approximately uniform across the entire bulk i-layer [3.3]. Consequently, it has been possible through the new approaches to the analysis of J_D-V characteristics to obtain valuable information about the contributions of p/i interface recombination and potential barriers at the p and n contacts, as well as bulk recombination. A key factor of the new approach is the analysis of differential diode quality factors, n(V), characteristics whose presence has not been previously recognized and allow direct information to be obtained about the nature and densities of the defect states in the i-layers [3.4]. The advantages of this new approach are illustrated here with successful application of the results on J_D-V characteristics to the results on V_{oc}'s under various illumination intensities in the cells. In these studies, the p/i interface recombination is minimized and the carrier transport is dominated by the recombination in the bulk i-layers. Excellent correlation is found between the J_D-V characteristics and V_{oc}'s for cells with different bulk i-layers in their annealed states as well as after light induced degradation. In addition, the distinct differences observed in the degradation kinetics of 1 sun V_{oc} between the cells having hydrogen diluted (protocrystalline) and undiluted i-layers are correlated with the differences in the defect state distributions between these two materials as indicated by the analysis carried out previously on the differential diode quality factors n(V) [3.4].

The p (a-SiC:H)/ i (a-Si:H)/ n (μc-Si) (superstrate) a-Si:H solar cells used in this study were fabricated by RF plasma enhanced chemical vapor deposition at a substrate temperature of 200°C under conditions described previously [3.5]. The bulk i-layers in the cell structures were deposited using SiH_4 diluted with H_2, with R = $[H_2]/[SiH_4]$ of either 10 (diluted) or 0 (undiluted). To minimize the contributions of shunts, cell structure areas of 0.02 cm^2 were used, which were defined by removing the uncovered top n μc-Si:H layers with reactive ion etching. The J_D-V characteristics were measured at temperatures that were controlled to within ±0.1^{o}C and a three-probe technique was used to eliminate any effects of extraneous series resistance. Care was also taken to ensure that the steady-state currents were measured at low biases and that no defects were introduced by double injection in the high forward bias regions. The annealed states were achieved by heating the cells for 4 hours at 170°C and the light induced defects were introduced using illumination generated by ELH lamp which has light intensity equivalent to that of 1 sun illumination. The illumination intensities lower than that of 1 sun was obtained with various combinations of neutral density filters.

It has been shown that for the cells in which bulk recombination dominates the current and the defect state distribution is essentially uniform across the bulk i-layer, there is a dependence of the J_D-V characteristics on the bulk i-layer thickness as a result of the scaling of the electric fields [3.3]. One natural extension to this is that because of the higher recombination in the thicker cells there should also be a corresponding reduction in their 1 sun V_{oc}'s. This requires that the bulk recombination dominate the carrier transport not only at relatively low biases but also at high biases up to 1 sun V_{oc}. That this is indeed the case is illustrated in Fig. 3.4 which shows the results on the thickness dependence of the 1 sun V_{oc} as well as J_D-V characteristics for p-i-n cells having the same structure but different thickness of R=0 bulk i-layers. In these cells the recombination at the p/i interfaces is minimized by having 200Å of a R=40 protocrystalline i-layer in the p/i region. It can be seen in the inset of Fig. 3.4 that the 1 sun V_{oc} decreases systematically with the increasing thickness of the bulk i-layer. A decrease of ~30mV (from about 0.89 to 0.86V) occurs in V_{oc} for an increase of a factor of 2 in the dark currents at low biases. This 30mV decrease in V_{oc} is consistent with the

dark current, whose increase for this change in voltage corresponds to the "effective" diode quality factor of ~1.6 for these cells. It is important to note here that these V_{oc}'s were measured not with fixed illumination intensities but instead with a fixed J_{sc} of 10 mA/cm^2 (equivalent to 1 sun J_{sc} for the cells with 0.4μm thick i-layer). This approach was used to eliminate the effect of the changes in light absorption due to the differences in the i-layer thickness. In thicker cells the increases in the dark current at voltages corresponding to 1 sun V_{oc} cannot be directly observed because the dark current becomes limited by carrier injection over the potential barriers in the i-layers adjacent to the p and n contacts.
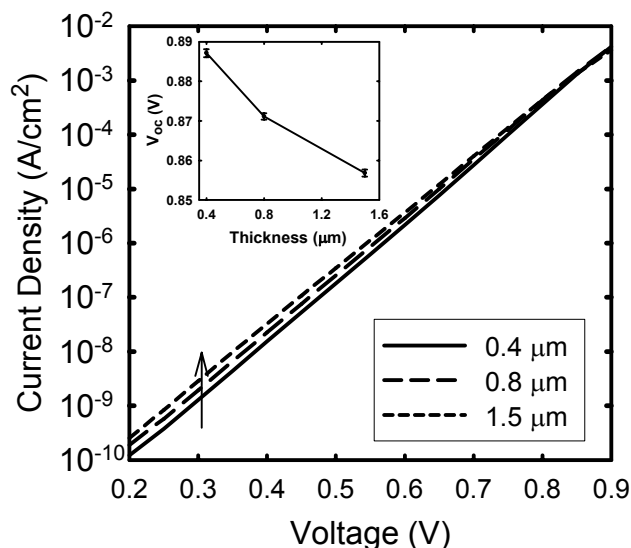
Fig. 3.4: Thickness dependence of 1 sun V_{oc} and J_D-V characteristics for p-i-n cells having the same structure but different thickness of R=0 bulk i-layers.
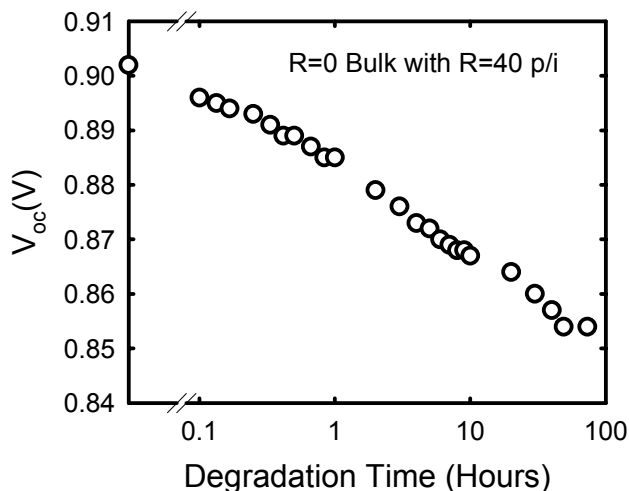
Fig. 3.5: Degradation of 1 sun V_{oc} under 1 sun illumination at 25°C for the cell in Fig. 3.4 with the 0.4 μm thick i-layer.

The domination of V_{oc} by bulk recombination currents at biases corresponding to 1 sun V_{oc} in the cells studied here could be further confirmed with the degradation kinetics of the 1 sun V_{oc}. Shown in Fig. 3.5 is the degradation of the 1 sun V_{oc} under 1 sun illumination at 25°C for the cell in Fig. 3.4 having the 0.4 μm thick i-layer. It can be seen that there is an immediate decrease in the 1

sun V_{oc} that is a clear indication that there are no significant contributions from p/i interface recombination. After 100 hours of degradation there is a decrease in V_{oc} of approximately 50 mV that is consistent with the changes in the J_D-V characteristics of the same cell as shown in Fig. 3.6. In Fig. 3.6 there is an increase in the recombination current of a factor of ~3 at a bias that corresponds to the 1 sun V_{oc}.
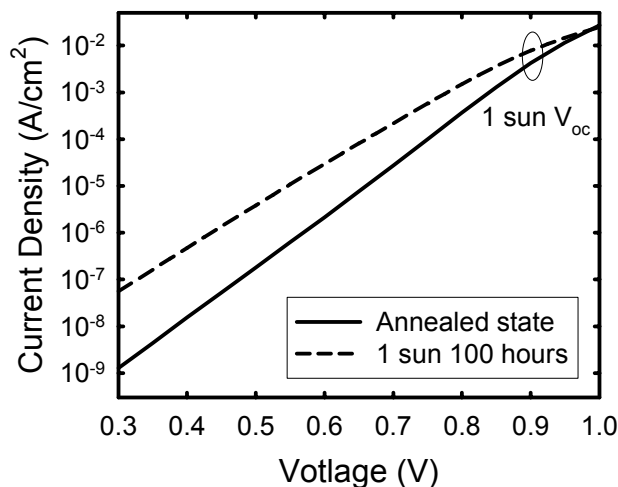
Fig. 3.6: J_D-V characteristics of the cell in Fig. 3.5 in the annealed state and after 100 hours of 1 sun illumination.

Similar correlations between the degradation of the V_{oc}'s and J_D-V characteristics are also obtained for the cells with R=10 protocrystalline i-layers. This is illustrated in Figs. 3.7 and 3.8 with results on a p-i-n cell with a 0.4 μm thick R=10 bulk i-layer and 200 Å thick R=40 p/i interface. In Fig. 3.7, the V_{oc} measured under light intensities from 1 to 10^{-4} sun is shown as a function of the degradation time under 1 sun illumination. It can be seen that as the light intensity and V_{oc} are lowered there are corresponding changes in both the rate and magnitude of the voltage decreases in reaching a degraded steady state after ~100 hours of illumination. For the illumination intensity of 10^{-4} sun, corresponding to an initial V_{oc} of 0.62 V, there is a decrease of 70 mV in V_{oc}. For 1 sun illumination the degradation is less than 10 mV, a value that is also significantly smaller than the 50 mV degradation of the 1 sun V_{oc} for the cell with R=0 i-layer after the same time of 1 sun degradation. This small degradation at such a high illumination level cannot be due to the limitations imposed by p/i interface recombination since a similar dependence of 1 sun V_{oc} on thickness was also found for the cells with R=10 i-layers. The degradation in V_{oc} in Fig. 3.7 can be directly correlated with the changes in J_D-V characteristics shown in Fig. 3.8. In Fig. 3.8 systematic increases are observed in the dark currents with illumination time just as in the corresponding V_{oc} results. The changes in the currents -- which are larger at the lower biases -- correspond to the higher decreases in V_{oc} measured at the lower illumination intensities. Unlike the large change in the cell with the R=0 i-layer, there are barely discernable changes in the dark current at the levels equivalent to 1 sun J_{sc} for the cell with the R=10 i-layer. This cannot be completely due to the carrier injection limitations imposed by the potential barriers since these limitations occur at similar current levels for both types of the cells. The difference in the 1 sun V_{oc} degradation between the cells with the R=10 and R=0 i-layer thus clearly points to a distinct difference in their gap state distributions upon light induced degradation.
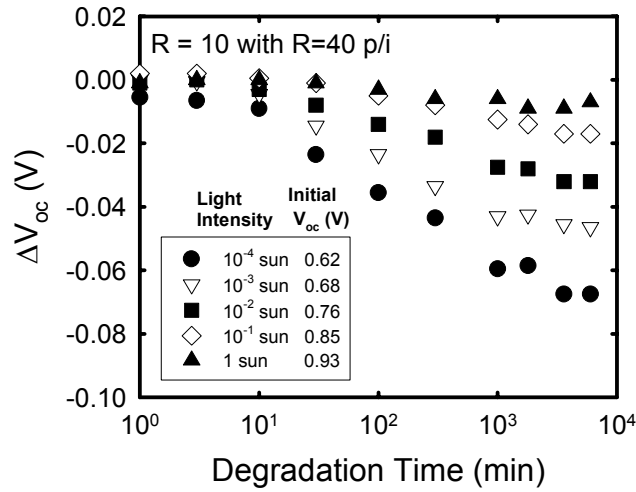
Fig. 3.7: Degradation of V_{oc} for a p-i-n cell with a 0.4 μm thick R=10 bulk i-layer and a 200 Å thick R=40 p/i interface, measured under light intensities from 1 to 10^{-4} sun.
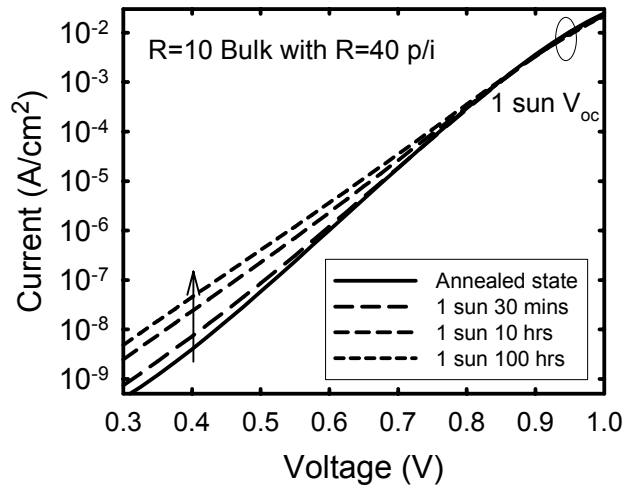
Fig. 3.8: J_D-V characteristics of the cell in Fig. 3.7 in the annealed state and after light induced degradation.

Several conclusions can be drawn from the above experimental results. First, in these cells the currents are dominated by bulk recombination up to bias levels equivalent to 1 sun V_{oc}. This is significant because the results obtained on the J_D-V characteristics can then be directly applied to the analysis of solar cell performance. Second, there are large light induced changes in the densities and distributions of the defect states in both the undiluted and diluted protocrystalline i-layers associated with the Staebler-Wronski Effect (SWE). Thirdly, the distributions of gap states in the two i-layers are distinctly different, thus leading to the differences in the corresponding solar cell performance and stability.

In order to understand the relation between solar cell parameters such as V_{oc} and the distribution of gap states in the i-layers, it is necessary to identify the differences between the two i-layer materials. The essential features of the distributions for both the undiluted and diluted i-layers

40

have been obtained from the analysis on the n(V) characteristics [3.4]. In both cases they are consistent with a Gaussian-like distribution around midgap followed by an exponentially rising distribution away from midgap which could also be regarded as the rising edge of a second Gaussian-like distribution. Similar Gaussian-like distributions have been proposed in several previous studies [3.6-3.9]. There is a major difference, however, between the undiluted and diluted i-layers whereby in the former case the rising edges of the second Gaussian-like distributions are much less steep. Furthermore, after the introduction of light induced defects, the distributions in both i-layers broaden with a much smaller broadening occurring in the case of the protocrystalline i-layer. For both cases there is also a large increase in the density of states around midgap which causes the large increases in the dark currents under low forward biases and the large decreases in the V_{oc}'s under illumination intensities much smaller than 1 sun. On the other hand, in the case of the dark currents under high forward bias and V_{oc} under sufficiently high illumination intensity, the splitting between the two quasi-Fermi levels is sufficiently large as to include as recombination centers not only the gap states around midgap but also those located further away from the midgap. For the cell with a protocrystalline i-layer, due to the narrower Gaussian distributions in the annealed and degraded states, the positions of quasi-Fermi levels at 1 sun V_{oc} are in a region where the native defects away from midgap play a dominant role in the recombination. This then explains the very small degradation of 1 sun V_{oc} while there is significant degradation for the V_{oc}'s under the lower intensities of illuminations. On the other hand, for the cell with undiluted i-layer, due to the broad distribution away from midgap the contribution from the light induced defects increases the recombination over that of the native defect states alone and accounts for the significant degradation in 1 sun V_{oc}. It is very important to note here that for cells having both undiluted and protocrystalline i-layers the degradation in the 1 sun V_{oc} is much smaller than that expected if the V_{oc} was limited purely by the recombination through the neutral dangling bonds, with states located around midgap and detected by electron-spin resonance. This is a further indication that gap states other than the neutral dangling bonds determine cell performance [3.10,3.11] and demonstrates the key role of the Gaussian-like distributions away from midgap as identified from the analysis of the n(V) characteristics.

It has been shown from the J_D-V characteristics that it is possible to identify and quantify the limitation imposed on 1 sun V_{oc} by bulk recombination. As a consequence, it has been possible to relate the light induced changes in J_D-V characteristics to those in 1 sun V_{oc} for cells with undiluted and protocrystalline i-layers. In addition, the new approach in the analysis of J_D-V characteristics in terms of differential diode quality factor n(V) has allowed these differences to be directly related to differences in the distributions of gap states in the corresponding i-layers. The results further demonstrate that J_D-V characteristics offer a *new and powerful probe* for characterizing mechanisms limiting the performance and stability of a-Si:H solar cells as well provide direct information about the distribution of gap states in the intrinsic layers. They also point out a key reason why it is not possible to obtain correlation between solar cell characteristics and neutral dangling bond densities. It is therefore important to take advantage of this powerful probe in guiding a systematic approach to further improving performance of a-Si:H based solar cells as well as in obtaining new insights into SWE.

Creation kinetics of metastable defects in protocrystalline intrinsic layers of p-i–n cells

In the course of studies on the light-induced changes of the i-layers, a new phenomenon in SWE was observed – the thermal relaxation of defect states at 25°C created by 1 sun illumination. This relaxation is readily observed at low forward biases and is sensitively dependent on the voltage at which it is characterized. This clearly shows that it is due to the states located close to midgap. Large decreases in this relaxation effect are also observed when the quasi-Fermi level splitting, and thus carrier recombination, is increased with higher bias, and the relaxation is eliminated for the splitting that occurs under 1 sun illumination. In addition, it is found that the relaxation effect changes with temperature -- as expected, however, in a way that cannot be readily characterized by any simple activation energy. These results have initiated *careful* studies on corresponding films as discussed in Task 4. Such studies confirm this relaxation effect, giving a new wrinkle to SWE, whose effects have not been recognized in either room temperature studies or in the models for creation of SW defects.

Because of the demonstrated ability to characterize the defect states in the i-layers of solar cells, the potential of using the recombination under far forward bias to generate defects in studies of the SWE was investigated. It was found that in cell structures, for which the recombination in the p/i interface regions is very much less than that in the bulk, equivalence is observed in the kinetics of the changes in the I-V characteristics under 1 sun illumination and those for far forward bias currents equal to J_{SC}. Such a method of creating SW defects was subsequently being used, adding flexibility to the conditions for the studies on the creation, annealing, and relaxation metastable defects.

The creation of metastable defects in the bulk of the intrinsic layers of a-Si:H p-i-n solar cells by recombination of photo-generated carriers as well as those injected under far forward bias has been investigated. The evolution in the defects, created with volume-absorbed red light at open circuit voltage and with constant far forward bias currents, was characterized with the Shockley-Reed-Hall recombination obtained from the dark currents under low forward bias voltages. This allowed the kinetics to be studied at different temperatures in the absence of isothermal annealing. It is found that the form of the kinetics obtained with the two methods are the same and a detailed study was carried out with currents from 1 to 100 mA/cm^2 with carrier injection during which the electron and hole concentrations remain essentially constant.

Because these measurements are carried out in about 5 seconds, they allow the recombination through these states to be monitored in essentially a continuous manner as well as prior to thermal annealing which is significant even at 25°C, particularly in the initial stages of degradation [3.4,3.13]. Consequently they have been particularly useful in characterizing the changes when the densities of the metastable states are **comparable to or less** than those of the intrinsic defects. New information is presented on the evolution of metastable defects induced either by the recombination of photo-generated carriers under open-circuit voltage or by the recombination of injected carriers under far forward bias and constant current. In these cells the short circuit current, J_{SC}, remains essentially unchanged during the degradation while the constant currents are maintained with essentially no change in the corresponding applied forward bias. Thus in both cases the quasi-Fermi level splitting, and hence the free carrier concentrations, n and p, responsible for the degradation remain constant. This is in contrast to the light induced changes in films where n and p continuously decrease due to the introduction of shorter carrier lifetimes during degradation [3.14].

Fig. 3.9 shows the recombination currents I_R at 0.4 V forward bias at 25 and 75°C for metastable defects induced by carrier injection currents from 5 to 100 mA/cm^2. Also included in Fig. 3.9(a) are the results obtained at 25°C with 1 sun illumination under open circuit conditions. A striking similarity can be seen in Fig. 3.9(a) between the results obtained with the 1 sun (with a corresponding I_{sc} of 10 mA/cm^2) and 30 mA/cm^2 where the excellent superposition is obtained for the *actual* currents. The very much larger currents at 75 °C are due to the high activation energy of I_R (half of the band gap) and not the correspondingly higher densities of metastable defects. At both temperatures three regimes can be clearly identified in I_R similar to those reported for the changes in thin films. There is a region with a power-law-like time dependence, as indicated in Fig. 3.9, which can be represented by a $t^{1/3}$ dependence, observed extensively in results on thin films [3.15,3.16]. Also in agreement with results on thin films is the fact that this regime, which at 25 °C covers changes in I_R of about a factor of 3 to 4, maintains such a form at different degradation intensities and temperatures. This regime in Fig. 3.9 is bounded by a transition to kinetics whereby the rate of change in I_R is greatly reduced. This transition eventually leads to a degraded steady state, as seen in Fig. 3.9(b) for the 30 and 100 mA/cm^2 results with dependence both on the degradation intensity and temperature similar to that found for fill factors]. The third regime, which represents the initial changes in the total defect state densities, has received much less attention than the $t^{1/3}$ dependence except in its possible contributions to stretched exponential type of kinetics [3.17]. However, in Fig. 3.9 it does represent a significant fraction of the total changes in I_R, prior to its transition into the regime that leads to a degraded steady state. At 25°C it covers a change in I_R by a factor of between 2 and 3 that is essentially independent of the degradation intensity.

(a)   (b)
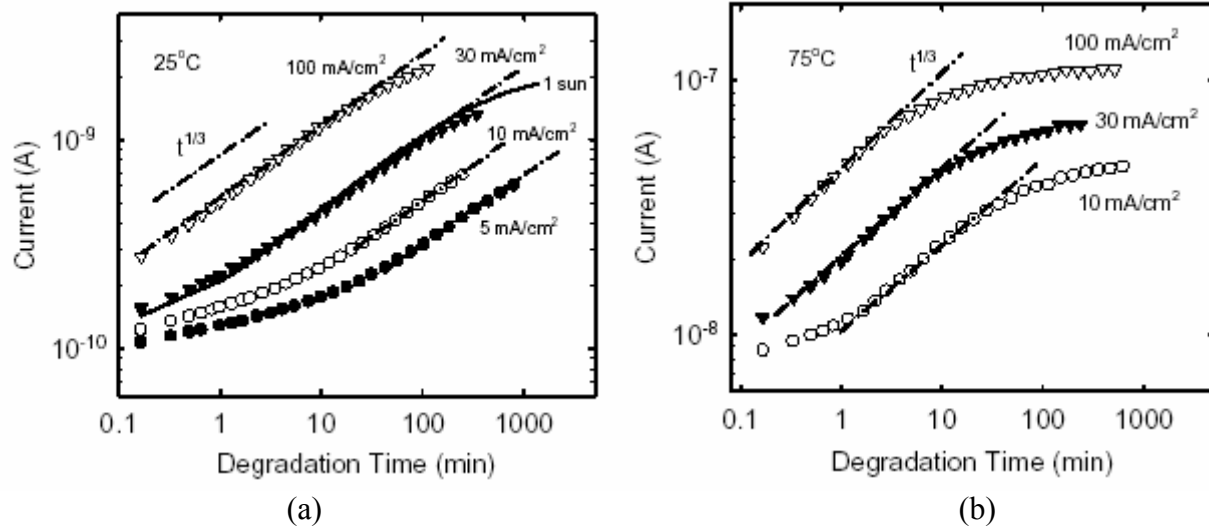
Fig. 3.9: (a) Change of current at 0.4 V and 25°C for a p-i-n cell under injection currents of different intensities and 1 sun illumination; (b) Change of current at 0.4 V and 75°C for a p-i-n cell under injection currents of different intensities.

43

Because the $t^{1/3}$ relation covers a limited region of the entire degradation kinetics, it is important to characterize the evolution of just the metastable states, including when their initial contributions are comparable to or less than those of the intrinsic states. This can be obtained from the results in Fig. 3.9 by subtracting I_{R0}, the recombination currents in the intrinsic state. Since this also takes into account any difference in the carrier capture cross sections that may exist between the intrinsic and metastable defect states $\Delta I_R = I_R - I_{R0}$ can be directly related to the densities of the metastable defects. The results obtained for ΔI_R from Fig. 3.9(a) and (b) are shown in Figs. 3.10(a) and 3.10(b) respectively. It can be seen that for both temperatures and for all degradation intensities, ΔI_R has power-law-like time dependence, which is essentially $t^{1/2}$ over the entire time span prior to the transition into the regime that eventually leads to saturation. This includes both the extensive initial evolution that can be seen in Fig. 3.9(a) at 25 ^{o}C as well as the region that was previously associated with a $t^{1/3}$ dependence. This evolution of the metastable defects with a $t^{1/2}$ dependence is present for all degradation currents I, such that the degradation is approximately *linear* with I. This naturally leads to the fact that the degree of degradation is proportional to $I^2 t$ as illustrated in Fig. 3.11 for the results in Fig. 3.10. Such a dependence is found for films and for solar cells, the latter in the degradation of the fill factor [3.18]. Street [3.19], who characterized the far forward bias-induced changes in defect state densities with thermally emitted currents under reverse bias, observed a $t^{1/2}$ dependence for the very high currents of 1 A/cm^2 where the densities of the induced states were indeed very much greater than those of the intrinsic state. He did not find the presence of a $t^{1/3}$ dependence at lower values of I and attributed its absence to his interpretation of carrier concentrations under far forward bias responsible for inducing the metastable states.
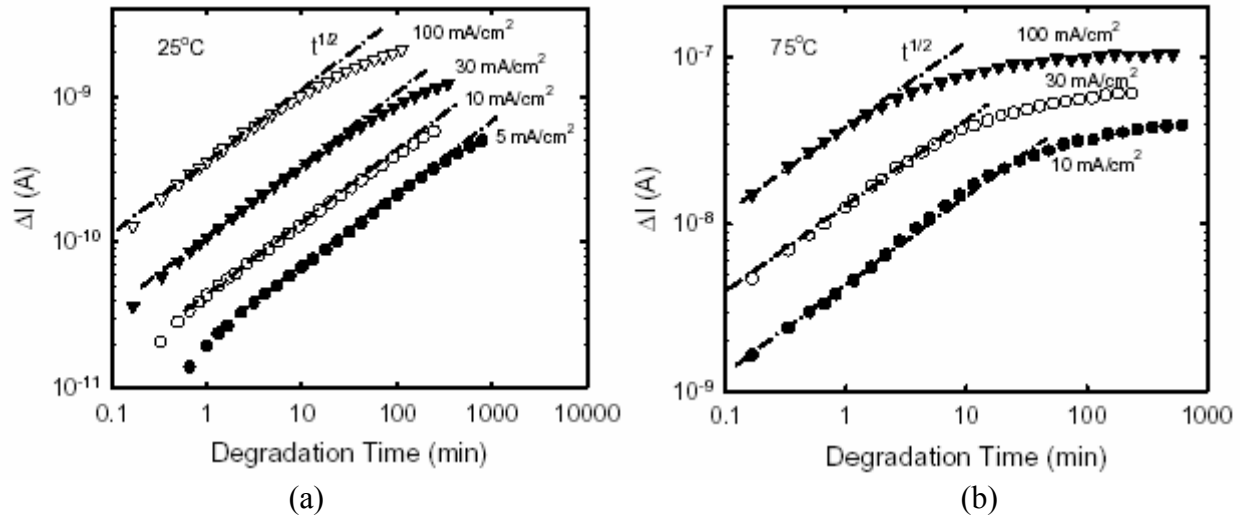
Fig. 3.10: (a) Changes relative to the initial value for the currents in Fig. 3.9(a); (b) Changes relative to the initial value for the current in Fig. 3.9(b).
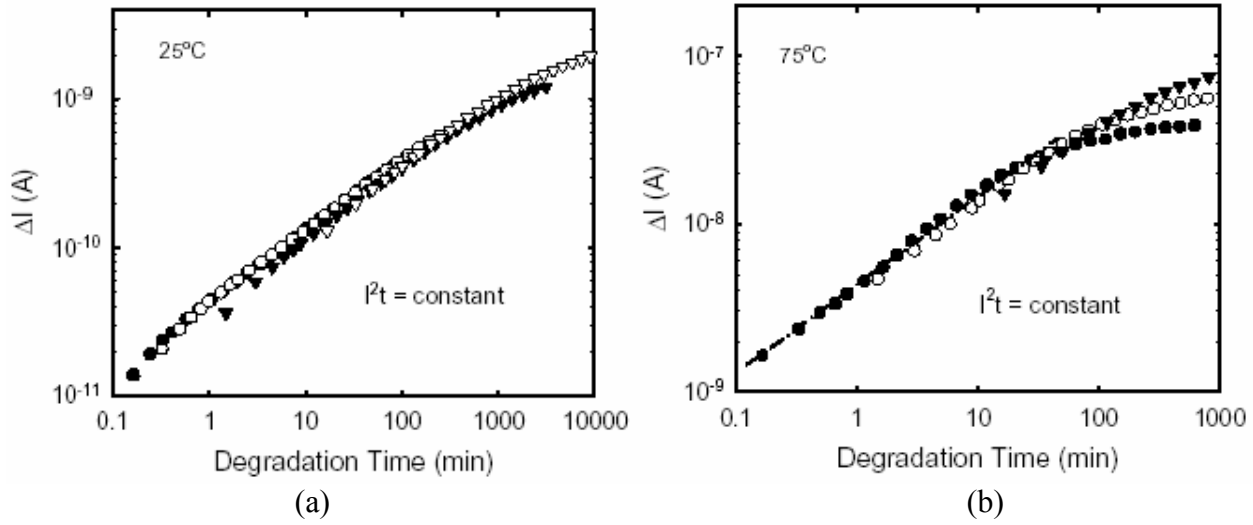
Fig. 3.11: (a, b) Normalization of the degradation kinetics under different intensities according to I^2t = constant for the corresponding figures in Fig. 3.10.

The similarity of the three regimes seen here to those reported for thin films, and particularly that represented by a $t^{1/3}$ dependence, is significant since these metastable defects are induced under conditions under which n and p remain constant. Most of the models proposed for the mechanisms responsible for the creation of light induced defects are based on the kinetics represented by the $t^{1/3}$ relation found for thin films, where *n, p* do not remain constant during degradation. Among these models, the one that has received the most attention is that of Stutzmann, Jackson and Tsai (SJT) [3.15] who proposed that the recombination between the electrons and holes in the band tail states break weak bonds, thus creating dangling bond defects. Since their concentrations are directly proportional to that of the free carriers, the rate equation for the creation of the dangling bond defects is proportional to the *np* product, each of which is proportional to the inverse of the dangling bond density, N_D. Consequently, in absence of any annealing, the rate equation for the increase in the densities of states, N_D, located around midgap has a bimolecular form, which can be written as:

$$\frac{dN_D}{dt} = C_1np = C_2 \frac{G^2}{N_D^2} \tag{3.1}$$

where C_1 and C_2 are constants and G is the photo-generation rate. This yields a time dependence for the total density of dangling bonds:

$$N_D(t)^3 - N_D(0)^3 = 3C_2G^2t \tag{3.2}$$

where $N_D(0)$ is the density of the native defect states. For $N_D(t) \gg N_D(0)$ Eq. 3.2 yields

$$N_D(t) \sim G^{\frac{2}{3}}t^{\frac{1}{3}} \tag{3.3}$$

The dependence found here for the changes in the total density of defects with n, p constant discounts the validity of the SJT model. The results for the evolution of just the metastable defects on the other hand are inconsistent with Eq. 3.2. Rather, the $t^{1/2}$ and I^2t dependences seen in Figs. 3.10 and 3.11 point to a rate equation for the creation of metastable defects, N_{ms} :

$$\frac{dN_{ms}}{dt} \sim \frac{I^2}{N_{ms}} \, .$$ (4)

It is significant that the creation kinetics found here for the metastable defects induced by the recombination of photo-generated carriers and injected carriers are the same. However the rate of creation of the metastable defects by the recombination of carriers from identical values of I_{sc} and I are not the same as seen in Fig. 3.9(a). The effect of the photo-generated carriers being field driven and having energies greater than the band gap, while the injected carriers are diffusive and their energies correspond to that of band gap, should be further investigated. *This study raise serious questions concerning the models of SWE that are based on a rate equation having the form of Eq. 3.1.* This includes not only the SJT model but also the hydrogen collision model proposed by Branz [3.20]

References

[3.1]   J. Deng, J.M. Pearce, V. Vlahos, R.W. Collins, and C.R. Wronski, *Mater. Res. Soc. Symp. Proc.* **762**, A3.4 (2003).

[3.2]   J.M. Pearce, R.J. Koval, A.S. Ferlauto, R.W. Collins, C.R. Wronski, J. Yang, and S. Guha, *Appl. Phys. Lett.* **77**, 3093 (2000).

[3.3]   J. Deng, J.M. Pearce, R.J. Koval, V. Vlahos, R.W. Collins, and C.R. Wronski, *Appl. Phys. Lett.* **82**, 3023 (2003).

[3.4]   J. Deng, J.M. Pearce, V. Vlahos, R.W. Collins, and C.R. Wronski, *Mater. Res. Soc. Symp. Proc.* **808**, A8.8 (2004).

[3.5]   R.J. Koval, J. Koh, Z. Lu, L. Jiao, R.W. Collins, and C.R Wronski, *Appl. Phys. Lett.* **75**, 1553 (1999).

[3.6]   K.K. Mahavadi, K. Zellama, J.D. Cohen, and J. P. Harbison, *Phys. Rev. B* **35**, 7776 (1987).

[3.7]   L. Jiao, H. Liu, S. Semoushkina, Y. Lee, and C.R. Wronski, *Proc. 25th IEEE PVSC* (IEEE, New York, 1996), p. 1073.

[3.8]   M. Günes and C.R. Wronski, *J. Appl. Phys.* **81**, 3526 (1997).

[3.9]   V. Nadazdy and M. Zeman, *Phys. Rev. B.* **69**, 165213 (2004).

[3.10] B. Von Roedern, *Appl. Phys. Lett.* **62**, 1368 (1993).

[3.11] J. Pearce, X. Niu, R. Koval, G. Ganguly, D. Carlson, R.W. Collins, and C.R. Wronski, *Mater. Res. Soc. Proc*. **664**, 1231 (2001).

[3.12] J. Deng, J.M. Pearce, V. Vlahos, M. Albert, R.W. Collins, and C.R. Wronski, *Conf. Record 31st IEEE Photovoltaic Specialists Conf*., IEEE New York, 2005, p. 1404.

[3.13] M.L. Albert, J. Deng, J.M. Pearce, X. Niu, R.W. Collins and C.R. Wronski, *Mater. Res. Soc. Symp. Proc*. **862**, A13.2 (2005).

[3.14] D.L. Staebler and C.R. Wronski, *Appl. Phys. Lett*. **31**, 292 (1977).

[3.15] M. Stutzmann, W.B. Jackson, and C.C. Tsai, *Phys. Rev. B* **32,** 23 (1985).

[3.16] P. Stradins, *Solar Energy Materials and Solar Cells* **78**, 349 (2003).

[3.17] D. Redfield and R. H. Bube, *Appl. Phys. Lett*. **54**, 1037 (1989).

[3.18] L. Yang, L. Chen, and A. Catalano, *Appl. Phys. Lett*. **59**, 840 (1991).

[3.19] R.A. Street, *Appl. Phys. Lett*. **59,** 1084 **(**1991).

[3.20] H.M. Branz, *Solar Energy Materials and Solar Cells* **78**, 425 (2003).

Task 4. **Characterization Strategies for Advanced Materials**

Relaxation of SWE defects in a-Si:H materials

The presence of the thermal annealing of light induced defect states at room temperature after 1 sun illumination, discovered in studies of solar cells, triggered a corresponding careful study of a-Si:H thin films. This study was carried out on the kinetics of fast states at 25°C created by 1 sun illumination in hydrogen-diluted (protocrystalline) a-Si:H films. The results were for the bulk properties of the a-Si:H films, which were confirmed by the similarity of their characteristics to those obtained for corresponding intrinsic layers in p-i-n solar cells. It is found that the kinetics exhibit two regimes. The first regime is in the form of a delay before the onset of an A·log(t) time dependence, indicative of a dispersive process. Despite the unexpected effect of a dependence of this first regime on the degradation/annealing history of the samples, it was possible to characterize the highly reproducible logarithmic dependences for different illumination times, as well as in the presence of different carrier generation/recombination rates. It is found that for the degradation times studied, the annealing kinetics associated with the second regime are independent of the 1 sun illumination time but are dependent on the recombination introduced by illumination levels as low as $\sim 10^{-6}$ sun. From the multiple experiments carried out in this study, it is found that the initial regimes depend not only on the carrier generation, G, and the time of 1 sun illumination of the films, but also on the degradation and annealing history. The subsequent regimes, which are independent of this history, do depend on G with the accompanying changes in the quasi-Fermi level splitting and the time of 1 sun illumination -- in agreement with the results on corresponding solar cells. These results raise interesting questions that still need to be answered about the nature and origin of the fast defects in order to assess their contribution to the long term degradation and the overall stability of a-Si:H materials.

The experiments were performed on hydrogenated protocrystalline silicon thin films (a-Si:H) that were deposited at 200°C with Cr/n-type a-Si:H coplanar Ohmic contacts. The measurements were carried out on different films from the same deposition with the initial states obtained after 4 hr annealing at 170°C. The samples were mounted in a light tight enclosure on a copper platform of a thermoelectric stage. An ELH lamp powered by a DC constant voltage supply was used to produce the 1 sun illumination and the probe photocurrents. Each lamp was used up to 20 hours over which time the illumination remained within ±5% of its initial flux. The probe photocurrents were generated with volume-absorbed illumination through a 687 nm band pass filter whose maximum intensity matched that obtained with a solar simulator. The light flux incident on the film was controlled with a shutter and 5 position filter wheel that could accommodate different combinations of neutral density and 687 nm band pass filters. Probing was conducted using filter combinations that were selected to produce bulk carrier generation rates from $\sim 10^{15}$ to 10^{18} cm^{-3}s^{-1}. During probe measurements, the currents were measured over a period of 10 seconds to take into account the photocurrent response times. In all cases the dark currents were an insignificant portion of the total current measured. The experimental procedures related to filter positioning, shutter state, and data collection were completely automated with a personal computer thus allowing the experiments to be reproducibly conducted over long periods of time.

The 1 sun photoconductivity of the films decreases approximately according to the often-reported $t^{-0.3}$ dependence, which after ~2 hours of illumination undergoes a transition to a slower rate. In this regime a relaxation in the 1-sun photocurrents can be observed even after very short interruptions in the illumination. This is illustrated in Figure 4.1 where the 1 sun photocurrents are shown with intermittent 10 second probe illuminations of $G=8x10^{15}$ cm^{-3}s^{-1}. It can be seen in the figure that such 1 sun photocurrents, relaxation decreases with the time of illumination. The corresponding results for the probe photocurrents are shown after normalizing them to their values of 1 minute degradation. This is done because of the very large changes in the current that occurs in minute of 1 sun illumination when probed with low levels of illumination [4.1]. These changes are
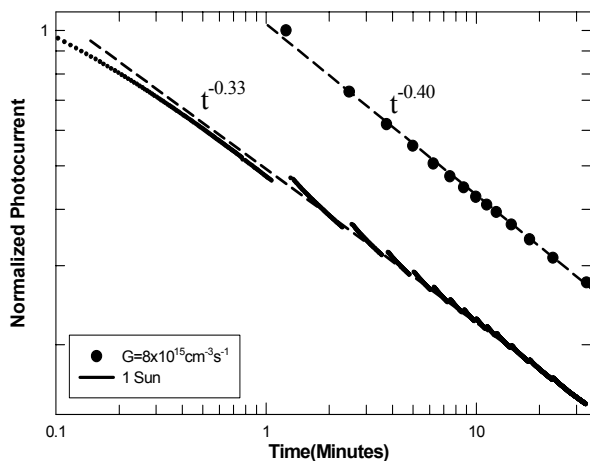
Figure 4.1: 1 Sun and 10 second intermittent probe photocurrents for carrier generation rate $G=8x10^{15}$cm^{-3}s^{-1} during the first 30 minutes of degradation.
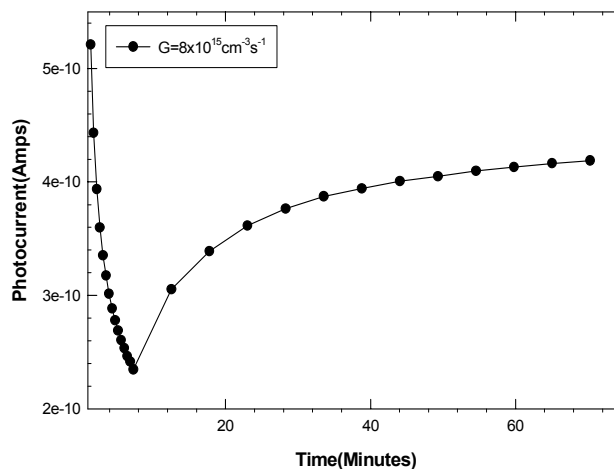
Figure 4.2: Probe photocurrents for $G=8x10^{15}$cm^{-3}s^{-1} during 1 sun degradation for 5 minutes and subsequent relaxation in the dark for 1 hour.

rapidly reduced by the creation of light induced defects under 1 sun illumination. The 1 minute photocurrents are found to be reproducible to ±10% in the different experiments and are also found to reflect the properties of bulk a-Si:H confirmed with results on corresponding p-i-n solar cells. Initial results on the cells indicated a time dependence different from the 1 sun relationship which is approximately $\sim t^{-0.4}$ as illustrated in Figure 4.1. This initial conclusion required revision and a subsequent detailed study on the creation of light induced defects is presented later. In Figure 4.2, results are presented for $G=8x10^{15}$cm^{-3}s^{-1} intermittent probe currents during a 5 minute degradation at 1 sun. During the period between 1 and 5 minutes of 1 sun illumination, the probe photocurrent decreases by about a factor of two. After this short illumination, the sample was recovered in the dark and occasionally probed leading to a remarkable recovery in the probe photocurrents after 1 hour to within 20% of the 1-minute value. In Figure 4.3, results are shown for the recoveries in the dark, after 30 minutes of 1 sun illumination, probed with G of $1x10^{15}$ and $8x10^{15}$cm^{-3}s^{-1}. In both cases the photocurrents had degraded by about a factor of four from their 1 minute values and recovered after 1 hour to about 50% of these values. When the relaxation of these photocurrents is represented in the form of their normalized values, as is done in Figure 4.3, striking features in the

annealing kinetics of the defect states are revealed. It can be seen that there are two regimes in the kinetics beginning with an initial delay regime before the onset of an A·log(t) dependence indicative of a dispersive process whereby the prefactor in both cases is A=0.9 as indicated in the figure. However, a difference can be seen between the times for these onsets in the two sets of results.

From the multiple experiments carried out at different stages of this study, it was possible to identify that the time of the delays was dependent on the history of the sample. Identical experiments conducted repeatedly on the same film exhibited a systematic change in the relaxation kinetics as illustrated in Figure 4.4. The results shown are for normalized photocurrents obtained with continuous illuminations with $G=8x10^{15}cm^{-3}s^{-1}$ after 30 minutes of 1 sun degradation. A systematic extension in delays prior to the logarithmic time dependence exhibit a
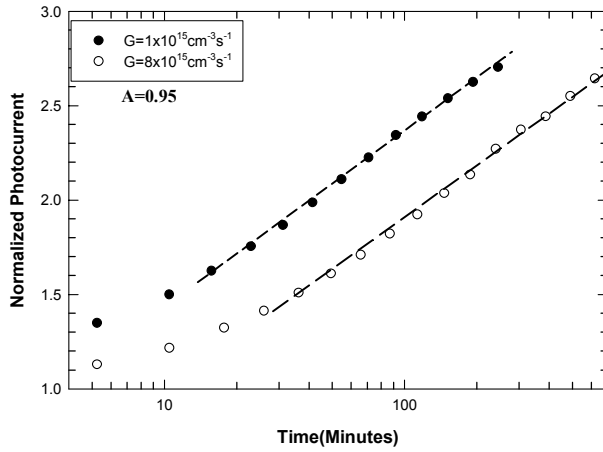
Figure 4.3: Intermittent probe photocurrents for $G=1x10^{15}cm^{-3}s^{-1}$ normalized to their degraded state after 30 minutes of 1 sun illumination obtained at different stages of this study.
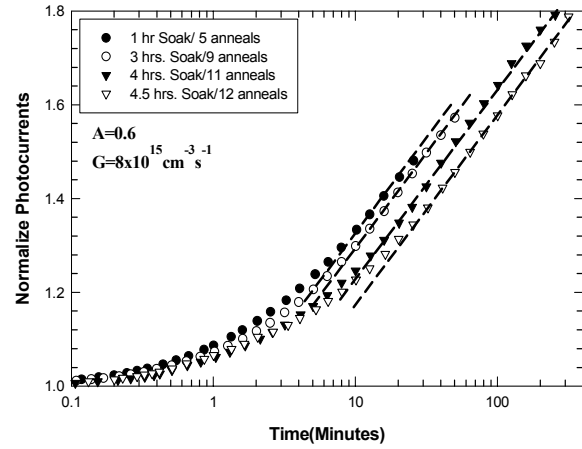
Figure 4.4: Continuous probe currents for $G=8x10^{15}cm^{-3}s^{-1}$ normalized to their degraded state after 30 minutes of 1 sun illumination.

dependence on the sequence in which the experiments were carried out. However, the prefactors of the A·log(t) time dependence remain the same with a value of A=0.4. Because the A·log(t) kinetics are independent of the sequence of experiments, it was possible to characterize their dependence on G. Results obtained after 30 minutes of degradation are shown in Figure 4.5 for G from $1x10^{15}$ to $4x10^{17}cm^{-3}s^{-1}$. These results not only show the systematic decrease in A from $0.60 \leq A \leq 0.16$ with increase in G, but also indicate that the delay in the onset of these kinetics also depends on G. It should be pointed out that the increase in G leads to photocurrents that result in both higher carrier recombination as well as higher quasi-Fermi level splitting. By augmenting the quasi-Fermi level splitting, states further removed from midgap are introduced as recombination centers. Analogous effects occur in p-i-n solar cells under forward bias as higher voltages are applied. The results for the relaxation in the bulk recombination currents after 30 minutes of degradation in corresponding p-i -n solar cells are shown in Figure 4.6 for forward biases of 0.3, 0.4, and 0.5 V. Although these

results cannot be readily correlated with those on the films in a quantitative way, a strong similarity to the results in Figure 4.5 can be seen. These results also exhibit a logarithmic time dependence whose prefactors systematically decrease with higher forward bias as the carrier recombination and quasi-Fermi level splitting increases.

It was also possible to identify the effects of different times of degradation on the annealing kinetics. This is illustrated in Figure 4.7 with results for continuous probe currents of $G=8\times10^{15}$ $cm^{-3}s^{-1}$ obtained after different times of 1 sun illumination from experiments that were not carried out in a sequence related to these times. In Figure 4.7 it can be seen that the time to reach the logarithmic time regime increases in length with the duration of 1 sun degradation shown for values between 15 minutes to 10 hours. However, there is no change in their prefactors, which remain at 0.4 throughout. Similar characteristics are obtained in both the delays and invariance in the prefactors of the logarithmic time regime for the recombination currents in p-i-n cells after prolonged degradation.
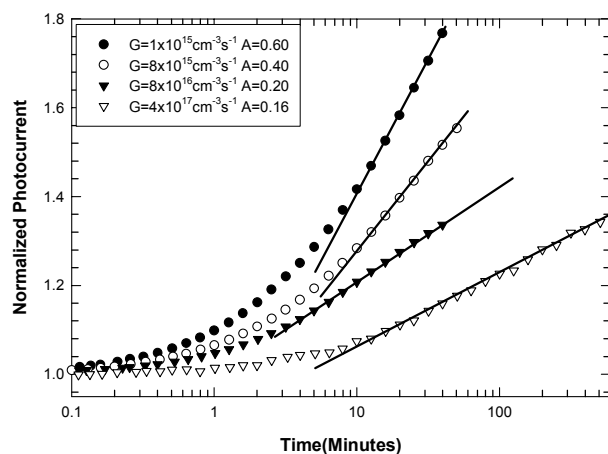
Figure 4.5: Continuous probe currents normalized to their degraded states after 30 minutes of 1 sun illumination for carrier generation rates from 1×10^{15} to $4\times10^{17}cm^{-3}s^{-1}$.
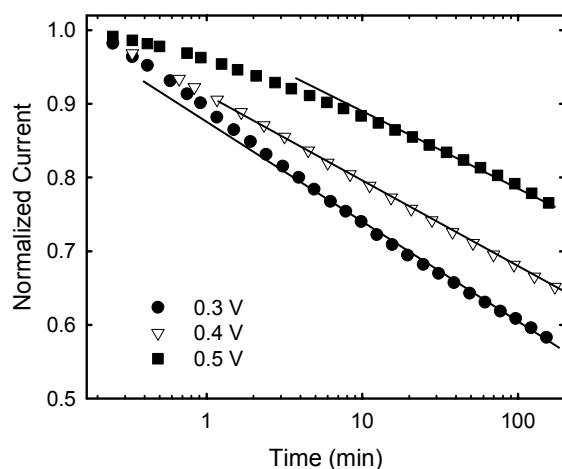
Figure 4.6: Bulk recombination currents in p-i-n solar cells at 0.3, 0.4 and 0.5 V forward bias after 30 minutes of 1 sun illumination.
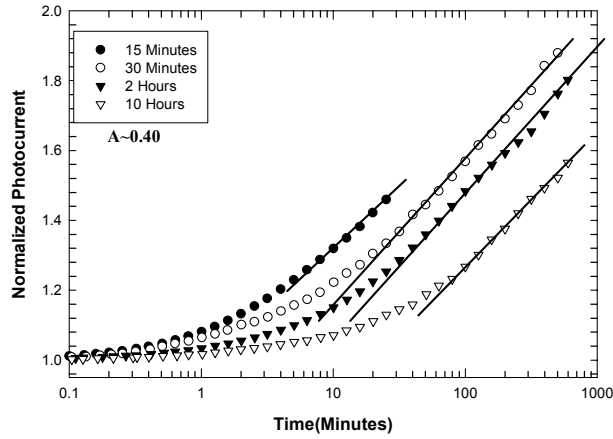
Figure 4.7: The continuous probe photocurrents for G=8x10^{15}cm^{-3}s^{-1} normalized to their degraded states after different 1 sun illumination times.

The annealing kinetics of the light induced defects at 25°C created by 1 sun illumination reported here is consistent with the fast states identified in studies of solar cells after high intensity illumination [4.2]. The similarity of the annealing characteristics obtained between the forward bias recombination currents in p-i-n solar cells and their corresponding i-layer film measurements, confirm that the results reported here are reflective of the properties of bulk a-Si:H. The photoconductivity studies of these protocrystalline hydrogen-diluted a-Si:H films were conducted with sufficiently short times of 1 sun illumination (≤ 10 hours) such that the carrier recombination was not dominated by the slow states [4.3]. The unexpected results on the dependence of the annealing kinetics on the degradation and annealing history of the thin film samples were thoroughly investigated with multiple identical experiments and it was found that they were not experimental artifacts. It could also be concluded that the changes occur only in the first of the two regimes found in the annealing kinetics of these fast defects. The presence of the two distinctly different regimes and the fact that their kinetics respond differently to history and 1 sun illumination time suggest two processes that contribute to the annealing kinetics. The similarities in the dependences of the changes in the first regime, comparing the history of experiments in Figures 4.4 and the times of illumination in Figure 4.7, suggest that the cumulative time of degradation, rather then the repetitive annealing, may be responsible for this effect. The corresponding lack of dependences of the A·log(t) regimes on the history and time of illumination would, on the other hand, suggest that there are differences in the underlying mechanisms responsible for these two regimes. The fact that both regimes/processes are affected by carrier recombination is highly significant. What is equally important, however, is that this occurs for carrier generation rates that correspond to illuminations of ≤ 10^{-6} sun, levels that are negligible in comparison to the illumination required to create the slow states that eventually dominate the long term degradation. The sensitivity to such recombination is

52

indicated by the large decrease in A from 0.95 for the annealing in the dark seen in Figure 4.3 to 0.6 in Figure 4.5 for carrier/generation of only $1x10^{15}cm^{-3}s^{-1}$; then A systematically decreases for increasing values of G. The fact that these characteristics are observed with carrier generation that results in small quasi-Fermi level splitting about midgap indicates that the states that act as the recombination centers are located close to midgap. This is the region of the gap associated with the location of the dangling bond defect states that have been extensively characterized by ESR and subgap absorption [4.4]. Since those defect states anneal out at significantly higher temperatures than 25°C, intriguing questions are raised about the nature of these fast states and dangling bond defect states, as well as the mechanism for their creation. This underscores further the complexity of the unresolved mechanisms responsible for SWE. To answer some of these questions, studies on both the protocrystalline and undiluted a-Si:H films should be carried out, as well as exploration of temperatures above 25° C.

Creation kinetics of SWE defects in a-Si:H films

Direct correlations have been obtained for the evolution of metastable defects in the intrinsic layers of protocrystalline p-i-n a-Si:H solar cells and in corresponding thin film material observed by characterizing their carrier recombination through states located around midgap. This study is performed using photoconductivity measurements with illumination levels from 1 to 10^{-6} sun for the thin film material and compared with the Shockley-Reed-Hall recombination in the dark under low forward bias for the corresponding solar cells. Because these studies were carried out in the absence of isothermal annealing, so as to characterize the actual creation kinetics, the contributions of different concentrations of the "fast/soft" and "slow/hard" defect states could be reliably analyzed. The same apparatus was used in relaxation studies to characterize 0.8 μm thick protocrystalline and undiluted thick films; the protocrystalline cell structures were characterized with SRH recombination at 0.4 V forward bias as in Task 3.

In order to directly correlate the creation of metastable states in films with creation in the corresponding intrinsic layers of solar cells, it is important to characterize the carrier recombination through similar regions of the gap. In the case of the protocrystalline a-Si:H reported here, the kinetics of the changes in carrier recombination are the same for quasi-Fermi level splitting obtained with generation rates (G) from $\sim10^{16}$ $cm^{-3}s^{-1}$ to that of 1 sun ($\sim5x10^{20}$ $cm^{-3}s^{-1}$). This is illustrated in Fig. 4.8 for the results obtained under 1 sun illumination at 25°C, where the inverse of the continuous 1 sun and probe photocurrents with $G=1.8x10^{16}$ $cm^{-3}s^{-1}$ are shown to reflect the changes in the gap states more directly. Also, to take into account the very fast changes observed in photocurrents with low generation rates, the photocurrents are normalized to their values after 1 minute. It can be seen in Fig. 4.8 that the kinetics of the changes in 1-sun and the intermittent probe photocurrents are the same. This is not the case, however, for non-protocrystalline films obtained without hydrogen dilution, demonstrating the importance of the a-Si:H microstructure, a point to be discussed later.

The same form of the kinetics is found for the recombination through midgap states in the intrinsic layers of the corresponding cells. This is illustrated in Fig. 4.9, which depicts the I_R results for metastable defects induced with 1-sun illumination under open circuit conditions and with a forward bias current of 30 mA/cm^2. The excellent superposition in the *actual* values of the current

also clearly shows that the recombination being characterized is in the bulk of the intrinsic layer. The striking similarity of the kinetics in Figs. 4.8 and 4.9 shows that with the characterization carried out here, it is possible to directly correlate the light induced changes in films with those in the intrinsic layers of the corresponding cells. This is true even though the changes in photoconductivity are due simply to changes in the electron lifetimes, while I_R is determined by both electron and holes. The difference in the approach to a degraded steady state that is observed here may be due to this difference, as well as to the symmetry of the quasi-Fermi splitting about midgap.

The kinetics in Fig 4.9, which reflect the recombination through both the intrinsic as well as the created metastable gap states, show three distinct regimes with the $t^{1/3}$ relation covering only a limited region of the kinetics. On the right side of the figure, this region is bounded by a transition to kinetics whereby the rate of change is greatly reduced as the degraded steady state is eventually reached. On the left side, the region transitions into one in which the contributions of the metastable defects are comparable or less than those of the intrinsic states. Because of the presence of "fast/soft" and "slow/hard" states [4.5,4.6], it is important to separate the contribution of the metastable states from that of the intrinsic defects in order to accurately characterize the evolution of the former. Since this also takes into account any difference in the carrier capture cross sections that may exist between the intrinsic and metastable states, these results can be directly related to the densities of the metastable defects. This was carried out in the same manner as was done with the recombination currents of the intrinsic layers of the p-i-n cell in Task 3, and can be obtained from $\Delta I_R = I_R - I_{R0}$, where I_{R0} is the recombination current in the intrinsic state. The results obtained for these kinetics are shown in Fig. 4.10 for the intrinsic layer of the cells and illumination levels from 5 to 100 mA/cm^2. It can be seen that for all the illumination levels, the evolution of only the metastable defects has a power-law-like time dependence, which is essentially $t^{1/2}$ over the *entire* region prior to the transition into the saturation regime. This includes the regime previously associated with a $t^{1/3}$ dependence.

Similar evolution of the metastable defects alone is obtained for the protocrystalline thin films under 1-sun illumination. In Fig. 4.10, results from 10 separate measurements of the probe photocurrents are shown after subtracting out the 1-minute values. Here the evolution of the metastable defects is represented by the inverse of the *net* probe photocurrents. In this case, a logarithmic-type time dependence is obtained with an exponent of 0.55±0.03. This is very close to the value of 0.5 for the corresponding intrinsic layers in the cells and clearly nowhere near the 1/3 that is generally associated with the creation kinetics of these defects. It is important to note here that -- as is evident from the results in Fig. 4.8 -- such a dependence is also obtained for the recombination in the 1-sun photocurrents. Thus, in this case the light induced changes in carrier recombination are essentially independent of the location of the electron quasi-Fermi level as it changes from approximately 0.25 eV above midgap up to ~0.55 eV from the conduction band.

This is not the case, however, for the undiluted a-Si:H films, for which the kinetics of the changes in recombination obtained for photocurrents under 1-sun illumination are distinctly different from those present in the probe photocurrents. This is illustrated in Fig. 4.11 with the results for the 1-sun and probe photocurrents having G=2x10^{16} cm^{-3}s^{-1} where the standard deviations in the exponent of the identified logarithmic regions are obtained from 10 measurements. The exponent

for the 1-sun photocurrents of 0.32 is the same as in the case of protocrystalline a-Si:H. On the other hand, in the case of the probe currents, the exponent is very close to 0.5. When the contributions of the intrinsic states are taken into account, the evolution of the states probed with 1-sun illumination has the logarithmic dependence close to 0.55, while that of the probe photocurrents is close to 0.7. This clearly shows that the evolution of the metastable defects in this material is different from that in the protocrystalline a-Si:H; thus, a new "fingerprint" exists for identifying possible causes that lead to their differences in stability.

The presence of a logarithmic dependence close to 0.5 in the evolution of the light induced defects in films and solar cells, as well as the dependence of defect density on intensity, I, are significant. This logarithmic exponent and proportionality in the densities of the metastable defects to $I^2 t$ further confirms the presence of a rate equation for the creation of metastable defects that is of the form $dN_{ms}/dt \propto I^2 / N_{ms}$, as proposed earlier. This has a direct bearing on the various models proposed for SWE that rely on the rate equation of the form $dN_{ms}/dt \propto I^2 / N^2_{ms}$ [4.7,4.8]. Results on both the protocrystalline and undiluted films are relevant for the 1-sun illumination level under which solar cells operate, and not for the significantly higher intensities generally used in studies on films. Results show that photoconductivity at intensities of 1 sun or greater do not necessarily reflect recombination through the states just around midgap, as is generally assumed. The results also reveal the kinetics in the absence of isothermal annealing, thus the actual creation kinetics are characterized. This in turn has allowed the contributions of different concentrations of "fast/soft" and "slow/hard" [4.5,4.6] metastable defect states to be reliably characterized. The origin of these states and the reason why their difference leads to the improved stability of protocrystalline a-Si:H is not understood. Improved understanding of this, as well as the dependence on microstructure, can be obtained from studies similar to the one reported here carried out at different temperatures on films and solar cells whose microstructure is changed systematically.
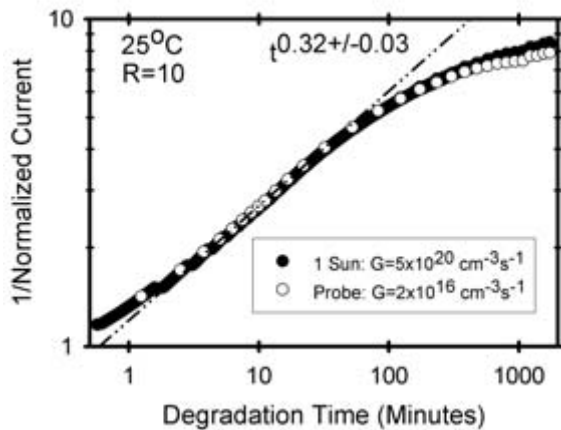
Fig 4.8: Reciprocal of 1 sun and probe photocurrents for 1 sun degradation.
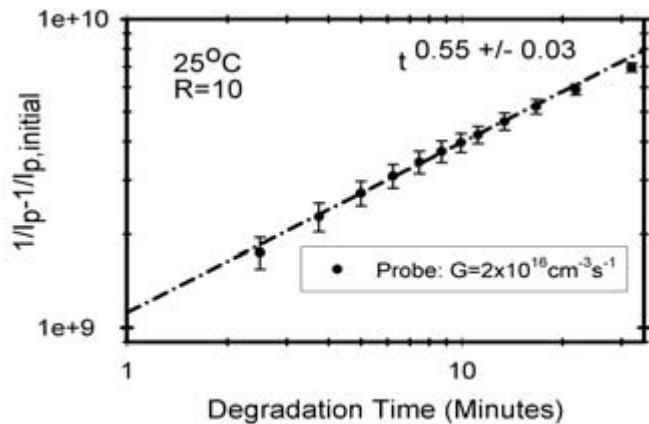
Fig 4.9: Evolution of forward bias current at 0.4 V for a p-i-n cell during the degradation with 1 sun and far forward bias current of 30 mA/cm^2.
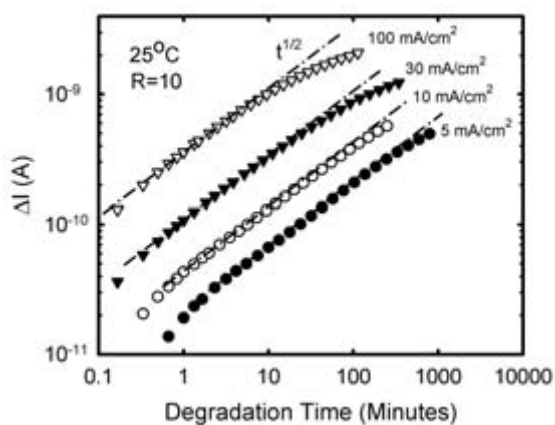
Fig 4.10: Evolution under 1 sun illumination of reciprocals of probe photocurrents relative to 1 minute value.
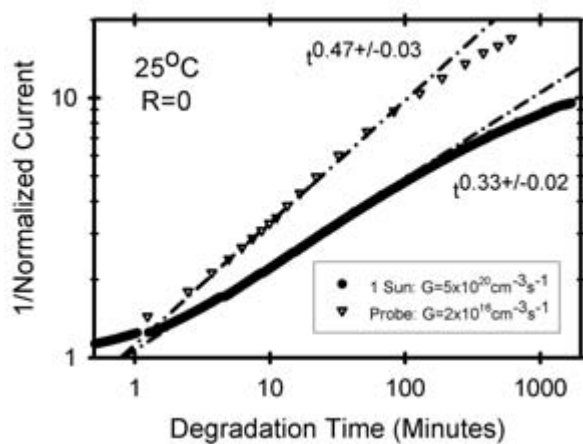
Fig 4.11: Reciprocal of 1 sun and probe photocurrents for 1 sun

56

Accurate analysis Dual Beam Photoconductivity
subgap absorption results from 2 to 0.5 eV

The light induced degradation in a-Si:H is generally associated with the creation of dangling bonds and the emphasis has been on determining their evolution under illumination. Although the neutral dangling bond (D^0) defect density can be directly measured using electron spin resonance the most commonly used method is photoconductive subgap absorption as a function of photon energy, $\alpha(h\upsilon)$. Generally $\alpha(h\upsilon)$ is interpreted solely in terms of D^0, dangling bond defect states where their densities are directly related to the magnitude, $|\alpha(h\upsilon)|$, typically for $h\upsilon$ from 1.1 to 1.3 eV. Such an approach has been successfully applied in interpreting a plethora of results on light induced changes as well as the creation and annealing of SWE defects. Because results have also been reported that point to the presence of other defect states, however, it has become clear that $\alpha(h\upsilon)$ cannot be interpreted in such a simple manner [4.9]. The approach taken at Penn State is to take into account the contributions to $\alpha(h\upsilon)$ due to multiple defect states by analyzing the evolution of the entire spectra rather than just their magnitude at an arbitrary value.

Any interpretation of $\alpha(h\upsilon)$ in terms of the density and energy distribution of multiple defect states is complicated by the nature of photoconductive subgap absorption, which is determined by N(E), the densities of *electron occupied states and not directly by the total defect density*, N_{def}. Photoconductive subgap absorption is determined from the absorption of photons, which excite electrons into the extended states in the conduction band whose density is then measured as the generated photocurrent. Thus, for any given photon energy, $\alpha(h\upsilon)$ is a measure of the number of electrons excited into the conduction band which are located at least within $h\upsilon$ of E$_C$ and is given by [4.10]:

$$\alpha(h\upsilon) = k(h\upsilon)^{-1} \int N(E)N_{CO}(E+h\upsilon-E_C)^{1/2}dE \tag{4.1}$$

The integral takes into account the fact that the photon $h\upsilon$ can excite electrons with an energy E such that $E_C - E < h\upsilon$. $N_{CO}(E-E_C)^{1/2}$ is the parabolic distribution of extended states in the conduction band. The parameter k depends on the dipole matrix elements for transitions from localized to extended states which in turn depends on both $h\upsilon$ and E in theory. In practice, however, k can be taken to be constant to a good approximation for the different gap states [4.11]. In the case of a single type of defect state it is possible to relate N(E) to $N_{def}(E)$ directly because the occupation of these states is constrained by charge neutrality. In the case of multiple defect states, however, the electron occupation of each type of state is *determined by the kinetics of carrier recombination*, and thus depends -- not only on their energy distribution in the gap -- but also on their relative densities and carrier capture cross-sections of the states [4.12]. Despite these complexities, information can be obtained about the evolution of the light induced defects and in particular about their energy distributions. In order to relate $\alpha(h\upsilon)$, which includes the contributions from all the electron occupied states at energies within $h\upsilon$ of E$_C$, to the energies of the defect states relative to E$_C$, it is necessary to take the derivative of the $\alpha(h\upsilon)$ spectra. For the case when N(E) changes rapidly with E, relative to $N_{CO}(E-E_C)^{1/2}$,

the effect of the latter on the joint density of states is small. Consequently, the derivative of equation 1 yields:

$$kN(E) = (h\upsilon)d[\alpha(h\upsilon)]/dE - \alpha(h\upsilon) \qquad (4.2)$$

In past studies of $\alpha(E)$ spectra, the nature of gap states in a-Si:H films was determined using a numerical model, SAM. With SAM which includes Eq. (4.2), experimental results on electron mobility-lifetime products over a wide range of generation rates and $\alpha(E)$ were self-consistently fit using the same "operational" parameters. Results were obtained showing that self-consistent fitting can only be achieved in the presence of different gap states. However, there are still many unanswered questions regarding their nature because of the number of unknown and adjustable parameters that are needed to describe these states in the simulations.

In order to experimentally characterize N(E) in any meaningful way it is critical to obtain $\alpha(E)$ spectra with both high accuracy as well as spectral resolution. The construction of a new dual beam photoconductivity (DBP) apparatus, which overcomes several deficiencies of the past one at Penn State, was completed in the last quarter of this phase. Among the key improvements are:

- The range in the spectra of $\alpha(E)$ was extended to 0.5 eV. Currently, however, the signal to noise ratio from 0.5 to ~ 0.65 eV is too low for $\alpha(E)$ to be considered reliable. However, the new DBP apparatus does effectively reduce the lower limit of the spectra from 0.9 eV to 0.7eV.

- The computer automation, improved signal to noise, and coupling to the lock-in amplifier, enables the $\alpha(E)$ to be obtained consistently in under 30 minutes.

- Improved data acquisition and monochromator resolution allows high resolution $\alpha(E)$ spectra to be obtained for reliable analysis of derivatives.

- The ability to measure electron $\mu\tau$ products has been incorporated into the new instrument.

- The ability to perform in-situ controlled light soaking of films has been established.

- The new instrument provides the capability of controlling the quasi-Fermi level splitting. This allows $\alpha(E)$ spectra to be obtained with known splitting values as well as maintaining these values constant during degradation. With bias illumination at constant generation rates, as used in the past, this splitting decreases due to higher recombination, and this adds another variable in the measurement of the $\alpha(E)$ spectra.

Figure 4.12 shows an example of the subgap absorption and its derivative kN(E) *clearly identifying three distributions of states around midgap*
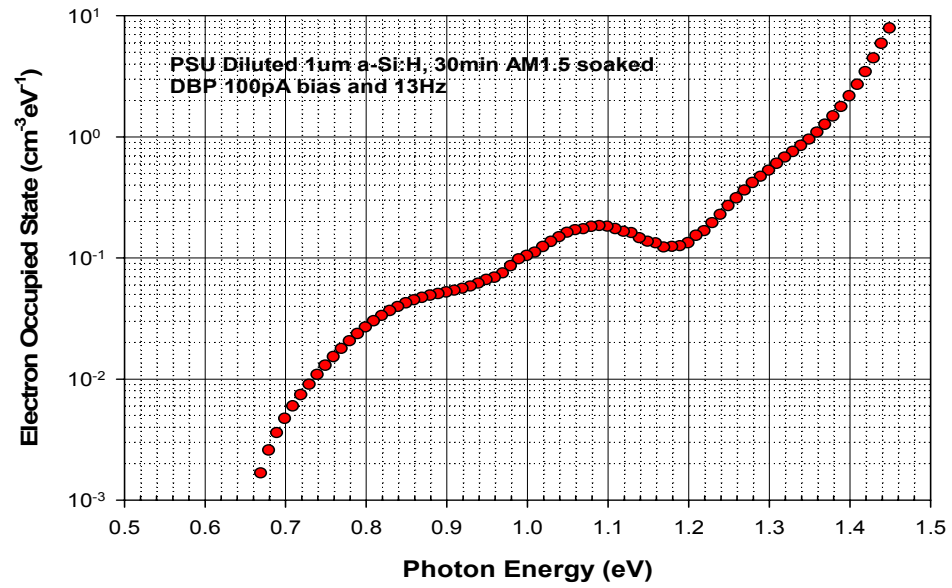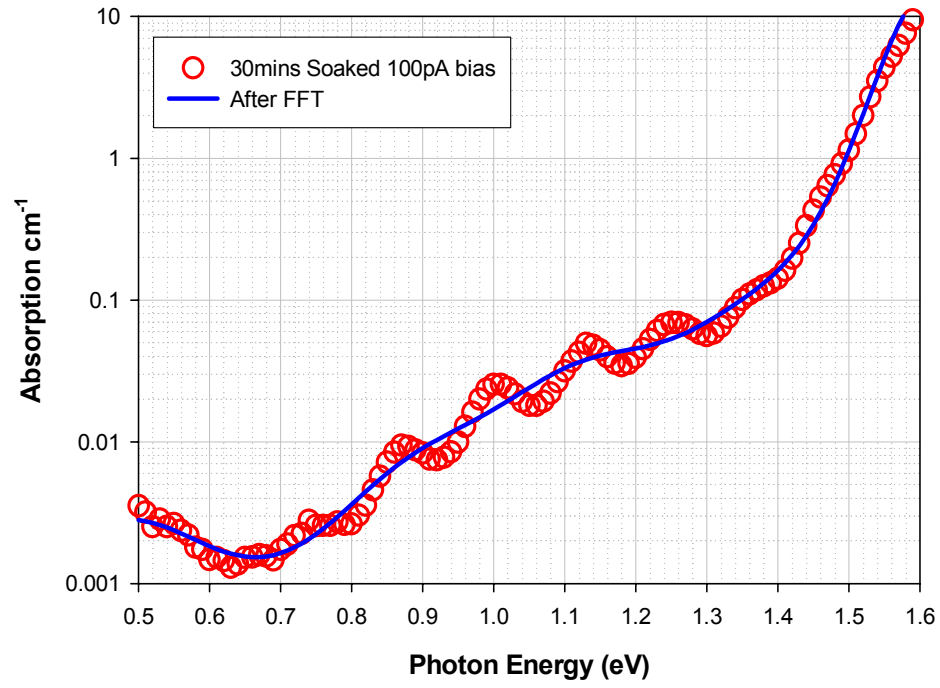
Fig. 4.12: An example of for the subgap absorption and its derivative kN(E), clearly identifying three distributions of states around midgap.

Virtual Interface Analysis: Evaluation of Compositional Depth Profiles in Mixed Phase (Amorphous + Crystalline) Silicon Films from Real Time Spectroscopic Ellipsometry

Overview

Deposition phase diagrams have been developed that describe the microcrystal nucleation and coalescence thicknesses for films that evolve from amorphous Si (a-Si:H) to microcrystalline Si (μc-Si:H) during plasma-enhanced chemical vapor deposition (PECVD) from SiH_4 at low temperature (T<300°C) [4.13]. In the simplest such diagram, the two transition thicknesses are plotted versus the H_2-dilution flow ratio $R=[H_2]/[SiH_4]$ for a given substrate. In fact, R is a key parameter controlling the phase -- from pure a-Si:H at low R to pure μc-Si:H at high R (e.g., $R \leq 10$ and $R \geq 40$, respectively, for native-oxide covered Si wafer substrates at 200°C). At intermediate R, the film forms initially as a-Si:H, but microcrystals nucleate from the amorphous phase and grow preferentially with accumulating thickness, eventually coalescing to form single-phase μc-Si:H. Optimum a-Si:H intrinsic (i) layers for solar cells are deposited using the maximum R possible, while avoiding microcrystal nucleation within the desired thickness [4.14-16]. Similarly, the optimum performance of μc-Si:H i-layers appears to occur at the minimum R possible, while maintaining single phase μc-Si:H throughout [4.17]. Owing to the importance of Si:H deposition near the phase boundaries, techniques are needed to determine the evolution of the μc-Si:H content as a continuous function of accumulated thickness. In this section, the application of real time spectroscopic ellipsometry (RTSE) is described for this purpose.

The ability to characterize the phase evolution of the intrinsic (i) semiconductor layers incorporated into amorphous silicon (a-Si:H) and microcrystalline silicon (μc-Si:H) thin film solar cells is critically important for device optimization. In this study, a new method has been developed to extract the thickness evolution of the μc-Si:H volume fraction in mixed-phase amorphous + microcrystalline silicon [(a+μc)-Si:H] i-layers. This method applies real time spectroscopic ellipsometry (RTSE) performed using a rotating-compensator multichannel ellipsometer during rf plasma-enhanced chemical vapor deposition of the films, in conjunction with a two-layer virtual interface analysis of the RTSE data. In this analysis, the depth profile of the μc-Si:H volume fraction in the mixed phase growth regime can be determined simultaneously with the evolution of the surface roughness layer thickness. From this information, the microcrystallite nucleation density and cone angle can be estimated, the latter describing the preferential growth of the silicon microcrystallites. The results from RTSE analysis correlate well with structural and p-i-n solar cell device measurements.

Experimental Details

The Si:H films studied by RTSE were prepared in a single-chamber reactor by rf PECVD using a substrate temperature range of 200-260°C. The deposition parameter of greatest interest is the H_2-dilution ratio R which was varied from R=7.5 to 40. The substrates were crystalline Si (c-Si) wafers covered by native oxides or by 2000-3000 Å

thick R=0 a-Si:H layers. The smooth surfaces of the former provide the highest sensitivity to the transition thicknesses, whereas the latter serve to simulate i-layer deposition on p-layers for p-i-n cells. The p-i-n solar cells for comparison with RTSE were fabricated in a load-locked multi-chamber system. Specular SnO_2-coated glass served as the substrate for the cells, and the p-layers were prepared without H_2-dilution from SiH_4, CH_4, and $B(CH_3)_3$. The phase diagrams for single- and multi-chamber Si:H deposition compare well as deduced from RTSE and ex situ SE, respectively. RTSE was performed using a rotating-compensator multichannel ellipsometer with a range of 1.5-4.5 eV and a minimum acquisition time of ~50 ms [4.18]. This instrument employs a MgF_2 biplate compensator in the PSC_rA configuration.

Results and Discussion

Real time spectroscopic ellipsometry and microstructural studies
The volume fraction of μc-Si:H in the graded, mixed-phase growth regime is best determined by tracking the dielectric function of the top-most growing material throughout the deposition. This is an ideal application for the two-layer [(outerlayer)/(surface roughness)] virtual interface (VI) approach to RTSE analysis [4.19,4.20]. In order to apply this approach, the dielectric functions (ε_1, ε_2) of the single-phase a-Si:H and μc-Si:H must be obtained by RTSE in the initial and final stages of the same deposition, when only the pure phases are growing. Figure 4.13 compares such results for an R=20 Si:H film deposited on a Si wafer substrate at 200°C. This film evolves through single-phase a-Si:H, mixed-phase (a+μc)-Si:H, and single-phase μc-Si:H regimes during growth to a bulk layer thickness of d_b=2300 Å, as will be demonstrated in subsequent figures.

The dielectric function of the pure a-Si:H phase in Fig. 4.13 was determined by applying the conventional two-layer (uniform bulk)/(roughness) model to analyze the RTSE data collected in the a-Si:H growth regime $0 \leq d_b \leq 200$ Å, before the microcrystal nucleation [4.21]. The dielectric function of the pure μc-Si:H phase was obtained from data collected after crystallite contact (d_b>1900 Å). In this case, the emphasis was on the top ~200 Å of the film where the dielectric function is nearly uniform with depth. The underlying structure, including the graded layer, is incorporated within a hypothetical uniform film located beneath a virtual interface to the top 200 Å. The correct roughness layer thickness at the very surface of the structure is required in order to extract the (ε_1, ε_2) spectra for single-phase μc-Si:H. This value was determined by embedding the VI analysis within a global error minimization routine. The differences between the results in Fig. 4.13 support an interpretation in terms of phase evolution during growth.

Figures 4.14 and 4.15(a) show the evolution of the μc-Si:H volume fraction $f_{\mu c}$ and surface roughness thickness d_s for the R=20 film of Fig. 4.13, as determined using two-layer VI analysis. The profile in $f_{\mu c}$ is presented throughout the mixed-phase growth regime, starting and ending near the nucleation and coalescence transitions. The optical model consists of (i) a pseudo-substrate, incorporating the history of mixed-phase
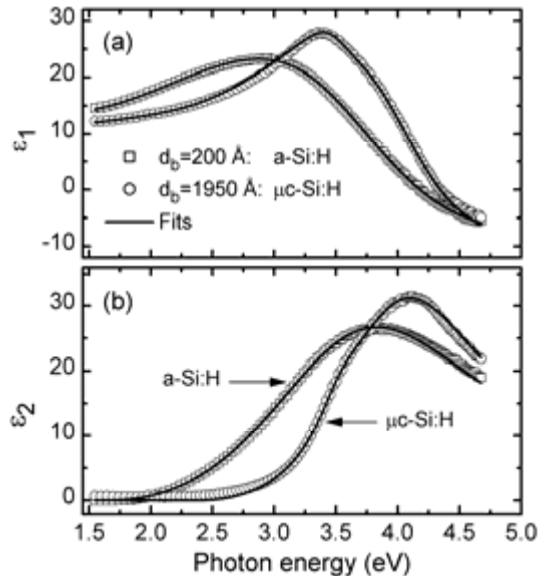
Fig. 4.13: (a) Real and (b) imaginary parts of the dielectric functions of the pure a-Si:H and μc-Si:H phases for an R=20 deposition on c-Si. The solid lines are fits using analytical models.

Fig. 4.14: Depth profile in the volume fraction of the microcrystalline phase (points) throughout the mixed-phase (a+μc)-Si:H growth regime for the R=20 Si:H deposition on c-Si from Fig. 4.13 Also shown as the solid line is the prediction of the microcrystallite cone growth model depicted in Fig. 4.15(b).

Fig. 4.15: (a) Surface roughness thickness versus bulk layer thickness for the R=20 Si:H deposition of Figs. 4.13 and 4.14; (b) schematic of the cone growth model used to estimate the microcrystallite nucleation density and cone angle.
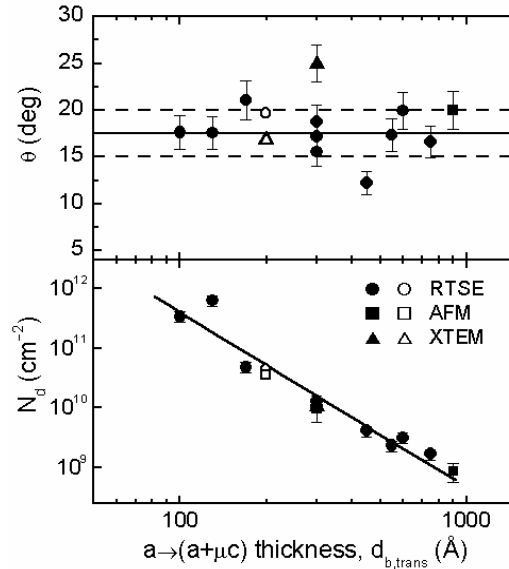
Fig. 4.16: Cone angle θ and nucleation density N_d versus the nucleation transition thickness $d_{b,trans}$ for Si:H films deposited under different conditions on c-Si wafers and on R=0 a-Si:H. The values of θ and N_d are deduced from RTSE (circles), XTEM (triangles) and AFM (squares). Data are included from this study (closed symbols) and from that of Ref. [4.24] (open symbols).

deposition, (ii) an outerlayer of thickness d_o, modeled as a $f_{\mu c}/(1-f_{\mu c})$ mixture of μc-Si:H/a-Si:H, and (iii) a topmost surface roughness layer of thickness d_s, modeled as 0.50/0.50 mixture of outerlayer/void. The dielectric function of the pseudo-substrate is determined as its pseudo-dielectric function (corrected only for the roughness layer). The dielectric functions of the two layers are determined from the component volume fractions and dielectric functions via Bruggeman effective medium theory [4.22].

The two-layer VI analysis used to deduce the results of Figs. 4.14 and 4.15(a) begins as follows [4.19]. Consecutive spectra $\{(\psi_j^{(e)}, \Delta_j^{(e)}); j=1, 2, 3\}$ (e: experimental) collected over a time interval $\Delta t = 103$ s (1 s acquisition; 50 s delay) are chosen such that the j=2 pair, at the interval center, occurs at the nucleation transition [i.e., at the roughening onset established from the two-layer (uniform bulk)/(roughness) model]. Initially, trial values are assigned to $\{f_{\mu c}, d_s\}$ for the interval Δt, providing sufficient information for analytical removal of the roughness layer. Thus, the spectra are converted to those of a hypothetical one-layer (pseudo-substrate)/(outerlayer) structure with pseudo-dielectric functions $\{(<\varepsilon_1>_j^{(e)}, <\varepsilon_2>_j^{(e)}); j=1, 2, 3\}$, for usual one-layer VI analysis [4.23].

At this point, the deposition rate (which is a known constant, r=0.28 Å/s) and the data set $\{(<\varepsilon_1>_j^{(e)}, <\varepsilon_2>_j^{(e)}); j=1, 2, 3\}$ are used together to determine the derivative of $<\varepsilon>$ with respect to the outerlayer thickness d_o, denoted $<\varepsilon>'$. Then using as input $<\varepsilon>'$ and the outerlayer dielectric function ε_o determined from $f_{\mu c}$, the common pseudo-substrate approximation is applied to predict the pseudo-dielectric function $(<\varepsilon_1>_2^{(c)}, <\varepsilon_2>_2^{(c)})$ at the center of the interval (j=2) [4.23]. Finally, the roughness layer is reintroduced, generating the predicted pair $\{(\psi_2^{(c)}, \Delta_2^{(c)})\}$. This pair is compared to the experimental spectra $\{(\psi_2^{(e)}, \Delta_2^{(e)})\}$, and an error function is generated. Based on the error function values for a grid of trial $(d_s, f_{\mu c})$, a new trial pair is determined. The process is iterated until $(d_s, f_{\mu c})$ are found that minimize the error function. Then the next triplet $\{(\psi_j^{(e)}, \Delta_j^{(e)}); j=2, 3, 4\}$ is chosen and the analysis is repeated.

The final results of this procedure are two functions $\{d_s(t), f_{\mu c}(t)\}$ that can be converted to $\{d_s(d_b), f_{\mu c}(d_b)\}$ because r is known throughout this process. The resolution of the profile $f_{\mu c}(d_b)$ is $\sim d_o = r\Delta t$, which is set for ~ 30 Å by the 50 s delay in data acquisition. A similar resolution is possible without loss of signal-to-noise ratio up to a deposition rate of r=10 Å/s by elimination of this delay. Finally, it should be noted that the average of the error functions over time provides a global measure of the fit quality, and this can be used as a criterion to select the correct roughness thickness and dielectric function in the analysis of the pure μc-Si:H phase.

Evidently, the evolution of d_s in Fig. 4.15(a) provides higher sensitivity to the presence of microcrystals, since it reveals a nucleation transition at ~ 300 Å, whereas $f_{\mu c}$ in Fig. 4.14 is first discerned above zero at $d_b \sim 700$ Å. The solid line in Fig. 4.14 is the result for $f_{\mu c}$ vs. d_b using a model of conical microcrystal evolution as shown in Fig. 4.15(b). This model is based on assumptions supported by cross-sectional transmission electron microscopy (XTEM) and atomic force microscopy (AFM). First, it is assumed

that all microcrystal nuclei originate at the nucleation transition thickness [~300 Å, from Fig. 4.15(a)]. Second, the area density of such nuclei is assumed to be N_d, and the nuclei are assumed to grow preferentially at the expense of the a-Si:H phase with a thickness-independent cone angle, θ. Third, cones are assumed to be spherically capped with a cap radius r_c given by $r_c = d_b - d_{b,trans}$. From this geometry, N_d and θ can be deduced from the values of $\Delta d_b = d_{b,coal} - d_{b,trans}$ and $\Delta d_s = d_{s,coal} - d_{s,trans}$. Here, $d_{b,trans}$ and $d_{s,trans}$ are the bulk and surface roughness layer thicknesses at the nucleation transition and $d_{b,coal}$ and $d_{s,coal}$ are the corresponding values at the coalescence transition. For the deposition of Figs. 4.13-15, values of θ=19° and N_d=1.1x10^{10} cm^{-2} are determined.

Figure 4.16 presents results for θ and N_d versus $d_{b,trans}$ for a series of Si:H films prepared on c-Si and R=0 a-Si:H surfaces under different conditions of R, T, and rf plasma power. Results solely from RTSE are compared with those from XTEM and AFM. In Fig. 4.16, the solid and open symbols represent results from this work and from Ref. [4.24], respectively. Evidently the nucleation density decreases significantly with increasing nucleation transition thickness, yet the cone angle is nearly constant between 15° and 20°. Figure 4.16 reveals consistency between the indirect (but real time) SE and the direct (but ex situ) structural measurements.

Device comparisons
Similar analyses to that of Figs. 4.12-15 performed for films deposited on R=0 a-Si:H can be compared with the performances of the corresponding p-i-n solar cells as long as the p-layers in the cells are amorphous and prepared near R=0. As an example, Fig. 4.17 shows RTSE results for the evolution of $f_{\mu c}$ near the microcrystal nucleation transition for two-step (R=40 interface)/(R=20 bulk) i-layers on R=0 a-Si:H substrate films. These structures are distinguished by the thickness d_i of the R=40 i-layer, selected as d_i=400, 150, and 0 Å, whereas the total i-layer thickness is fixed at 4000 Å. Figure 4.18 shows the dark current-voltage (J-V) curves of the corresponding Si:H p-i-n solar cells of this series. For the cell with the highest currents in Fig. 4.18 (inverted triangles, with d_i=400 Å), the associated two-step i-layer structure measured by RTSE exhibits the nucleation transition after 200 Å of R=40 deposition. For comparison purposes, the cell with the lowest currents (squares) was fabricated using an optimum two-step (R=40 interface)/(R=10 bulk) a-Si:H i-layer (designated the "optimum cell") [4.16].

Computer simulations of the J-V curves were also carried out, and the results are shown in Fig. 4.18 (solid lines). The optimum cell could be considered in terms of a uniform a-Si:H i-layer with a mobility gap of 1.86 eV. Results for the other three cells were modeled assuming an a-Si:H i-layer at the p/i interface with the same 1.86 eV mobility gap and a bulk μc-Si:H i-layer with a mobility gap of 1.15 eV as indicated by RTSE. This simple model for the solar cells reproduces the overall features of the J-V curves. Table 4.1 includes a comparison of the RTSE and J-V simulation results for the three Si:H p-i-n solar cells with two-step (R=40)/(R=20) 4000 Å i-layers of Figs. 4.17 and 4.18. The table compares the thickness of the a-Si:H i-layer component nearest the p/i interface, as deduced from the device modeling, with the i-layer thickness required to reach $f_{\mu c}$ = 0.2, as deduced from RTSE. This good agreement suggests that once $f_{\mu c}$ approaches ~0.2, transport is dominated by the microcrystalline phase.

Summary

Real time spectroscopic ellipsometry (RTSE) studies of PECVD Si:H films that undergo amorphous-to-(mixed-phase amorphous + microcrystalline) transitions were performed. Novel approaches for RTSE data analysis were conceived and developed that provide (i) the volume fraction of the μc-Si:H phase as a function of the accumulated thickness, (ii) the optical properties of the films in the amorphous, mixed-phase (a+μc)-Si:H, and single-phase μc-Si:H growth regimes, and (iii) estimates of the nucleation density and cone angle characterizing the evolution of the Si microcrystallites in the mixed-phase (a+μc)-Si:H regime. The resulting information correlates well with that from ex situ structural and device performance studies.
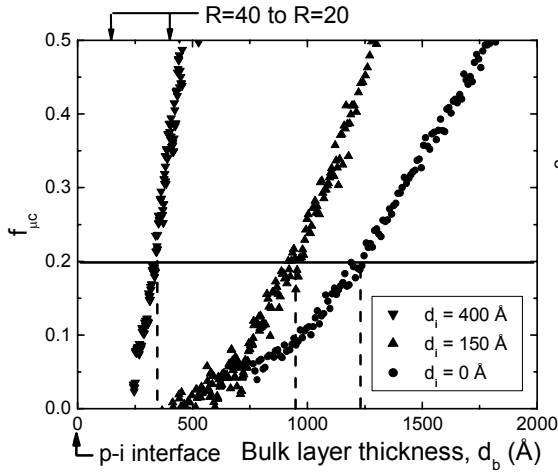
Fig. 4.17: Depth profiles of the microcrystal volume fraction $f_{\mu c}$ in the i-layer for three 4000 Å thick two-step R=40/20 i-layer structures on R=0 a-Si:H substrates. The thicknesses d_i of the R=40 p/i interface layer are $d_i = 0$ Å (circles), 150 Å (triangles), and 400 Å (inverted triangles).
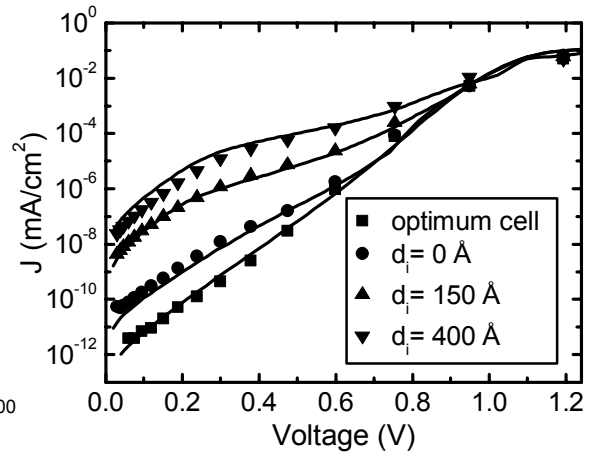
Fig. 4.18: Experimental (symbols) and simulated (lines) dark J-V characteristics for four Si:H p-i-n solar cells. The squares denote a standard cell that incorporates an optimized [R=40 (200 Å)]/[R=10 (3800 Å)] a-Si:H i-layer, and the other cells incorporate [R=40 (d_i)]/[R=20 (4000–d_i) Å] i-layers where $d_i = 0$ Å (circles), 150 Å (triangles), and 400 Å (inverted triangles).

65

Table 4.1:
Correlation of RTSE and device modeling results for Si:H p-i-n cells with 4000 Å thick two-step R=40/20 i-layers in which the R=40 interface thickness is varied.

First step: R=40 thickness (Å)	Real time SE: d_b when $f_{\mu c}$=0.2 (Å)	Device Modeling: Heterojunction position from p/i (Å)
0	1240 ± 30	1300 ± 300
150	950 ± 30	700 ± 200
400	330 ± 20	400 ± 100

References

[4.1]   L. Jiao, H. Liu, S. Semoushkina, Y. Lee, and C. R. Wronski, *Proc. 25th IEEE PVSC* (IEEE, New York, 1996), p. 1073.

[4.2]   L. Yang and L. Chen, *Appl. Phys. Lett.* **63**, 400 (1993).

[4.3]   C. R. Wronski, J. M. Pearce, R. J. Koval, X. Niu, A. S. Ferlauto, J. Koh, and R. W. Collins, *Mater. Res. Soc. Symp. Proc.* **715**, 459 (2002).

[4.4]   C. Lee, W. D. Olsen, and P. C. Taylor, *Mater. Res. Soc. Symp. Proc.* **70**, 225 (1986).

[4.5]   H. Fritzsche, *Annu. Rev. Mater. Res.* **31**, 47 (2001).

[4.6]   P. Stradins, *Solar Energy Materials and Solar Cells* **78**, 349 (2003).

[4.7]   For a review see Ref. 4.5.

[4.8]   Howard M. Branz, *Solar Energy Materials and Solar Cells* **78**, 425(2003).

[4.9]   C. R. Wronski, J. M. Pearce, R. J. Koval, X. Niu, A. S. Ferlauto, J. Koh, and R. W. Collins, *Mater. Res. Soc. Symp. Proc.* **715**, A13.4 (2002).

[4.10] J. M. Pearce, J. Deng, V. Vlahos, R. W. Collins, and C. R. Wronski, *Proceedings of the 3rd World Conference on Photovoltaic Energy Conversion,* (IEEE, New York, 2004) Paper 5O-D14-01.

[4.11] W. B. Jackson, S. M. Kelso, C. C. Tsai, J. W. Allen, and S. J. Oh, *Phys. Rev. B* **31**, 5187 (1985).

[4.12] A. Rose, *Concepts in Photoconductivities and Allied Problems*, (Robert. E. Kreiger, New York, 1978).

[4.13] R. W. Collins, A. S. Ferlauto, G. M. Ferreira, C. Chen, J. Koh, R. J. Koval, Y. Lee, J. M. Pearce, and C. R. Wronski, Solar Energy Mater. Solar Cells **78**, 143 (2003).

[4.14] Y. Lu, S. Kim, M. Gunes, Y. Lee, C. R. Wronski, and R. W. Collins, *Mater. Res. Soc. Symp. Proc.* **336**, 595 (1994).

[4.15] D. V. Tsu, B. S. Chao, S. R. Ovshinsky, S. Guha, and J. Yang, *Appl. Phys. Lett.* **71**, 1317 (1997).

[4.16] J. Koh, Y. Lee, H. Fujiwara, C. R. Wronski, and R. W. Collins, *Appl. Phys. Lett.* **73**, 1526 (1998).

[4.17] O. Vetterl, F. Finger, R. Carius, P. Hapke, L. Houben, O. Kluth, A. Lambertz, A. Muck, B. Rech, and H. Wagner, *Sol. Energy Mater. Sol. Cells* **62**, 97 (2000).

[4.18] J. Lee, P. I. Rovira, I. An, and R. W. Collins, *Rev. Sci. Instrum.* **69**, 1800 (1998).

[4.19] S. Kim and R. W. Collins, *Appl. Phys. Lett.* **67**, 3010 (1995).

[4.20] H. Fujiwara, J. Koh, C. R. Wronski, R. W. Collins, and J. S. Burnham, *Appl. Phys. Lett.* **72**, 2993 (1998).

[4.21] I. An, Y. M. Li, C. R. Wronski, H. V. Nguyen, R. W. Collins, *Appl. Phys. Lett.* **59**, 2543 (1991).

[4.22] H. Fujiwara, J. Koh, P. I. Rovira, R. W. Collins, *Phys. Rev. B* **61**, 10832 (2000).

[4.23] D. E. Aspnes, *J. Opt. Soc. Am. A* **10**, 974 (1993).

[4.24] H. Fujiwara, Y. Toyoshima, M. Kondo, and A. Matsuda, *Phys. Rev. B* **60**, 13598 (1999).

APPENDIX A
Theoretical Considerations

The experimental results previously reported (April 2003) showed that there are no large densities of defect states in i-layers adjacent to p, n contacts such as predicted by the defect pool model. Instead, the distributions of the defects are relatively homogeneous across the bulk. This conclusion greatly facilitates the analysis of the experimental results and serves as a fundamental basis for the correct understanding of the physical mechanisms governing the operation of a-Si:H solar cells.

From the J_D-V characteristics it was clearly seen that extended voltage regions exist in which the currents increase exponentially with the applied forward bias voltages, consistent with the diffusion/recombination model proposed by Lips et al.[1] Furthermore, it has been shown that these currents increase when the density of defects is increased by light-induced degradation, which indicates that the recombination process is governed by Shockley-Reed-Hall (SRH) recombination mechanisms in which electrons and holes recombine through the defect states in the gap[2].

The current transport in the dark for these a-Si:H solar cells over an large range of forward bias voltages can be considered in terms of the diffusion of the electrons and holes into the bulk under the forward bias and recombination through gap states which have a relatively homogeneous distribution across the bulk. The recombination rate given by SRH theory is determined by the product of the electron and hole concentrations, n and p respectively, which can be expressed as:

$$r = np/(sn+p)\tau_{no} \qquad (A1)$$

where s is the ratio of the electron to hole capture cross sections and τ_{no} is the electron capture time determined by the density of gap states that act as recombination centers. To facilitate the discussion but without losing generality, an equal electron and hole capture cross section (s=1) is assumed in the following discussion.

Even though the recombination occurring at the p/i interface and in the bulk is both described by the SRH recombination mechanism, their contributions to the diode quality factor of the dark current characteristics are distinctly different. Let us first consider the recombination in the bulk. When the carrier transport is diffusive, the concentrations of the electrons and holes in the bulk have an exponential (negative) dependence on the potential difference relative to the n and p contacts, respectively. The further away from their respective contacts, the higher the potential difference so that these carrier concentrations decay exponentially away from their contacts. Under forward bias, the potential difference is reduced across the bulk so that the carrier concentrations increase exponentially. Although n and p both vary rapidly across the bulk, their product is constant and:

$$np = n_i^2 \exp(qV/kT) \qquad (A2)$$

[1] K. Lips, Mat. Res. *Soc. Symp. Proc.* **377**, 455 (1995).
[2] W. Shockley and W. T. Read, *Phys. Rev.* **87**, 835 (1952).

where n_i is the intrinsic carrier concentration, determined by the band gap; q is the electron charge; k is the Boltzmann constant; T is the temperature; and V is the applied forward bias voltage.

In the case of a single defect in the mid gap, τ_{no} is a constant. Then according to Eq. A1, the maximum recombination rate occurs at the location where n+p is the minimum, which is achieved only when n=p. At this location, from Eq. A2, it can be easily found that:

$$n = p = n_i \exp(qV/2kT) \quad\quad\quad\quad (A3)$$

Away from this location in the bulk, either n or p increases rapidly so that the recombination rate decreases rapidly resulting in a recombination profile, which has sharp slopes around its center. Combining equation A1 and A3, the maximum recombination rate r_{max} can be obtained:

$$r_{max} = [n_i \exp(qV/2kT)]/\tau_{n0} \qu\quad\quad\quad (A4)$$

The total recombination current can be obtained by either integrating r across the bulk or equivalently by multiplying r_{max} by the width of the recombination profile. It has been shown that this width is proportional to the local field ε around the center of the recombination profile so the dark current J_D has the form[3]:

$$J_D \sim [(1/\varepsilon) \, n_i \exp(qV/2kT)]/\tau_{n0} \quad\quad\quad (A5)$$

Due to the fact that in these a-Si:H cells the n contact is more heavily doped than the p contact, the location where n=p is closer to the p contact. As will be discussed in more detail, the n an p contacts induce a space charge region in the i-layer adjacent to them so that the electric filed ε in the bulk does not scale exactly with the bulk i-layer thickness -- neither does J_D. This conclusion has been utilized earlier in explaining the thickness dependence of the J_D-V characteristics. More importantly, since ε is not a fast-varying function of V, Eq. A5 yields a diode quality factor of 2, which has been well established in the case of crystalline-Si p-n junctions at low forward bias when the recombination in the space charge regions dominates the total current.

In the case of a-Si:H i-layers, which have a continuous distribution of gap states between valence band and conduction band, however, τ_{no} is no longer a constant. In SRH type recombination, the gap states that act as recombination centers are those located between the electron and hole quasi-Fermi levels, F_n and F_p respectively, where the separation is equal to the applied voltage. As the applied voltage and the splitting of the quasi-Fermi levels are increased there is a corresponding continuous increase in the number of gap states acting as recombination centers, which leads to a decrease in τ_{no} and a corresponding increase in the recombination. In the case of a distribution of states increasing exponentially around mid-gap the increase in the number of recombination centers enhances the current by an exponential term, which then changes the diode quality factor from 2 to a lower value whose offset depends on the specific exponential

---

[3] C. van Berkel, M. J. Powell, A. R. Franklin, and I. D. French, *J. Appl. Phys.* **73**, 5264 (1993).

69

form in the energy distribution of the gap states. This has been confirmed numerically by Hack and Shur.[4] Thus, an effective diode quality factor m of 1.4 to 1.6 seen over an extended voltage region in the J_D–V characteristics of the cells with minimized p/i interface recombination,[5] can be explained simply by the presence of a continuous distribution of gap states in the a-Si:H i layer. There is therefore no necessity, as has been previously suggested,[6] for a spatially varying density of defects in the i-layer as predicted by the defect pool model.

For the case of a gap state distribution that is significantly different from exponential form, however, $d(\ln(J_D))/dV$ does not remain constant so that the diode quality factor changes with the applied voltage. Consequently, there is a voltage dependent differential diode quality factor n(V), which is equal to the inverse of $[kT/q][d(\ln(J_D))/dV]$. In the results obtained for cells having either diluted or undiluted i-layers, where the recombination is dominated by that in the bulk of the i-layers, values of n(V) are present which are approximately constant over an extended region of voltage. This indicates that the distributions of the gap states around mid-gap are similar, although not identical, to that of an exponential form such as the Gaussian distributions suggested by the studies on the corresponding thin film i-layers[7]. It can be pointed out here also that the difference in such n(V) values obtained between the two types of cells is a clear indication of a difference in the energy distribution of the gap states in their respective i-layers.

In the case of recombination at the p/i interface, the concentration of holes adjacent to the p-contact is much larger than that of the electrons, and the electrons become the minority carriers. Thus, from Eq. A1, the recombination rate is determined only by the electron concentration at the p/i interface. The electron concentration n at p/i interface is an exponential function of the applied forward bias voltage V so that the recombination rate at the p/i interface is given by:

$$r_{pi} = n/\tau_{npi} = [n_{0pi}\exp(qV/kT)]/\tau_{npi} \qquad (A6)$$

where n_{0pi} is the electron concentration at the p/i interface in equilibrium and τ_{npi} is the electron capture time at the p/i interface, which is usually smaller than that in the bulk. It should be noted here that n_{0pi} can be controlled by changing the band gap of the p/i interface layers as has been carried out for controlling p/i recombination in the cells studied. The corresponding dark currents can be obtained either by summing up all the recombination in the thin regions adjacent to the p/i interface or by introducing an effective interface recombination velocity, S_{eff}, which gives:

$$J_D = qnS_{eff} = qS_{eff}\, n_{0pi} \exp(qV/kT) \qquad (A7)$$

[4] M. Hack and M. Shur, *J. Appl. Phys.* **54**, 5858 (1983).
[5] J. Deng, J.M. Pearce, R.J. Koval, V. Vlahos, R.W. Collins and C.R. Wronski, *Appl. Phys. Lett.* **82**, 3023 (2003).
[6] M.A. Kroon and R.A.C.M.M. van Swaaij, *J. Appl. Phys.* **90**, 994 (2001).
[7] L. Jiao, Ph.D. Thesis, The Pennsylvania State University, 1999.

Thus, in the case of interface recombination dominated currents, the effective diode quality factors such as m* are close to one.[8] By comparing Eq. A7 with Eq. A5, it can be seen that the increase with voltage in the interface recombination currents is much faster than that of the bulk recombination currents. It is therefore not surprising that at the higher bias voltages the p/i interface recombination can readily dominate over the bulk recombination.

To simplify the above discussion, the effects of the space charge that is present in the bulk on the current transport are not considered here. This space charge consists mainly of the trapped electrons and holes, the concentrations of which are higher than those of the free electrons and holes even in the highest quality a-Si:H solar cells. The densities of trapped electrons and holes depend on the positions of electron and hole quasi-Fermi level, respectively. These in turn are determined by the free electron and free hole concentrations -- higher free carrier concentration leads to higher trapped carrier concentration for the corresponding carriers. The presence of the space charge in i-layers affects the electric field distribution across the bulk. Due to the high electron (n_0) and hole concentrations (p_0) in the regions of i-layer adjacent to the n and p contacts, respectively, the space charge densities in these regions are higher than in the bulk. This results in potential drops V_n near the n and V_p near the p contact, which constitute barriers for the injection of carriers from the contacts into the bulk of the i-layer. These potential barriers are included in the schematic band diagram for a p-i-n cell under a forward bias V shown in Figure A.1. In the figure, ϕ represents the potential drop across the bulk region and $\phi=V_{bi}-V-V_n-V_p$, where V_{bi} is the built-in voltage across the cell. Positive values of ϕ indicate that the carrier transport is diffusive while negative values indicate that the transport is drift-driven. In a-Si:H solar cells with low defect densities in their intrinsic layers, both V_n and V_p are quite small so that ϕ remains positive for biases V up to values close to V_{bi}. This results in the exponential dependence of the diffusive current J_D on V over an extended voltage range so that direct correlations of J_D-V characteristics can be made with bulk dominated recombination and consequently the densities of gap states in the intrinsic layers.

The transport of photo-generated carriers is distinctly different from that of those injected from the contacts since with volume-absorbed light the carriers are created throughout the bulk of the i-layer. They are subject to a drift field, ε, which sweeps them out towards the contacts as a net drift current[9]. In i-layers with low defect densities the space charge that is present has only a small effect on the electric field distribution so that $\varepsilon \cong \phi/L$ where ϕ is the potential drop across the bulk of the i-layer and L its thickness. The photo-current J_L is then determined by the densities of electrons and holes that reach the contacts before recombining, where the probability of undergoing recombination depends on their effective lifetime, τ, and transit time T_{tr}. This current J_L can be written as $J_L=J_G-J_{RG}$ where J_G is the photocurrent created by the generation rate of carriers, G, due to the absorbed photons in the bulk. J_{RG} is the recombination current in the bulk which is determined by T_{tr} and τ. J_G depends only on the intensity of the illumination and is independent on the electric field ε (V) while J_{RG} depends on ε since $T_{tr}\propto 1/\varepsilon$. Under short

[8] J. Deng, J.M. Pearce, R.J. Koval, V. Vlahos, R.W. Collins and C.R. Wronski, *Appl. Phys. Lett.* **82**, 3023 (2003).
[9] D.E. Carlson and C.R. Wronski, *Appl. Phys. Lett.*, **28**, 671 (1976).

circuit conditions, the effective transit time $T_{tr} \propto 1/V_{bi}$. In high quality a-Si:H cells J_{RG} is significantly lower than J_G which is reflected by the quantum efficiencies under short circuit conditions of virtually 100% for carriers generated in the bulk. For $J_{RG} \ll J_G$, $J_{SC} \cong J_G$ which makes J_{SC} directly proportional to the illumination intensity as is observed in high quality cells.

Under a forward bias V across the i-layer, T_{tr} increases as does J_{RG}. At the same time the balance between the drift and diffusive currents from the high densities of n_0, p_0 carriers is disturbed so that the net diffusion currents, J_{diff}, are introduced in the opposite direction to the photo-generated currents, as is illustrated in Figure A.2. J_L then becomes:

$$J_L(V) = J_G - J_{RG}(V) - J_{diff}(V) \qquad (A8)$$

Since the mechanism governing this J_{diff} is exactly the same as that for the diffusion current J_D in the dark, as discussed earlier, they increase exponentially with V. For the same diffusive transport under illumination as that in the dark, $J_{diff}(V) = J_D(V)$. Since both J_{RG} and J_{diff} increase with V, J_L decreases until it becomes zero at $V = V_{OC}$, so under open circuit conditions:

$$J_{SC} \cong J_G = J_{RG}(V_{OC}) + J_{diff}(V_{OC}) \qquad (A9)$$

which for $J_{diff} \gg J_{RG}$ becomes:

$$J_{SC} \cong J_{diff}(V = V_{OC}) = J_D(V = V_{OC}) \qquad (A10)$$

At high current densities and forward bias, there are clear deviations from the exponential dependence on V in the dark current. This occurs when $V_{bi} - V$ approaches $V_n + V_p$, which corresponds to ϕ approaching zero. Further increases in V invert the field across the i-layer, which then results in the field driven drift currents. In addition, at high values of J_D the potential barriers associated with V_n and V_p begin to limit the carrier injection from the contacts into the i-layer[10]. The height of these barriers depends on the space charge, which in turn is determined by n_0, p_0 and the defect densities in the i-layers, which are small in high quality intrinsic materials. As a consequence, the effects of V_n, V_p do not become significant until current levels are very high. However, in low quality cells, where these barriers are high due to a large density of defects, their effects already become significant at lower current levels.

As a consequence there is a superposition between J_{SC} versus V_{OC} and J_D versus V, as reported. This occurs even though the superposition principle is not valid in a-Si:H solar cells for *all* values of V due to the voltage dependent contributions of J_{RG} to J_L.

The absence of superposition between J_{SC}-V_{OC} and J_D-V, however, also occurs if at $V = V_{OC}$, J_{RG} is comparable to or larger than J_{diff}. This can occur at high illumination levels when V_{OC} approaches V_{bi} so that the small values of ϕ and hence ε present across the bulk result in $T_{tr} > \tau$, which lead to large values of J_{RG}. At the same time the high forward bias currents in the J_D-V characteristics encounter limitations on carrier injection imposed by the potential barriers V_n and V_p. Both of these effects can then contribute to a split

---

[10] F.A. Rubinelli, J.K. Arch, and S.J. Fonash, *J. Appl. Phys.* **72**, 1621 (1992).

between the two characteristics since the limitations of J_{RG} on V_{OC} move the J_{SC}-V_{OC} to lower values of V_{OC}, while on the other hand the limitations on carrier injection move J_D-V to higher values of V. Higher densities of defects in the i-layer result in larger values of J_{RG} as well as V_n and V_p at the n and p contacts, so that the divergence between the J_{SC}-V_{OC} and J_D-V characteristics occurs at lower voltages.

As was discussed earlier, the potential barriers that limit the carrier injection are determined by both n_0 and p_0 as well as by the densities of defects in the i-layer contributing to the space charge. Any increase in density of these defects leads to larger V_n and V_p, which then reduces the carrier injection. The contributions to the divergence between J_{SC}-V_{OC} and J_D-V due to the densities of gap states in the i-layer have been confirmed by introducing light induced defects.

Although the presence of the potential barriers V_n and V_p has little effect on V_{OC}, it can have deleterious effect on FF. This is because, as has been discussed above, the presence of these barriers lowers the average electric filed across the bulk and thus reduces the collection efficiency of the photo-generated carriers. This points to a important fact that FF is not merely determined by the defect density in the bulk but also affected by V_n and V_p. Consequently, FF is in general not a parameter directly corresponding to the i-layer defect density. Thus, when FF is used as a parameter to study the density of defects in the bulk i-layers, it is necessary to ensure that the contributions from V_n and V_p is negligible.
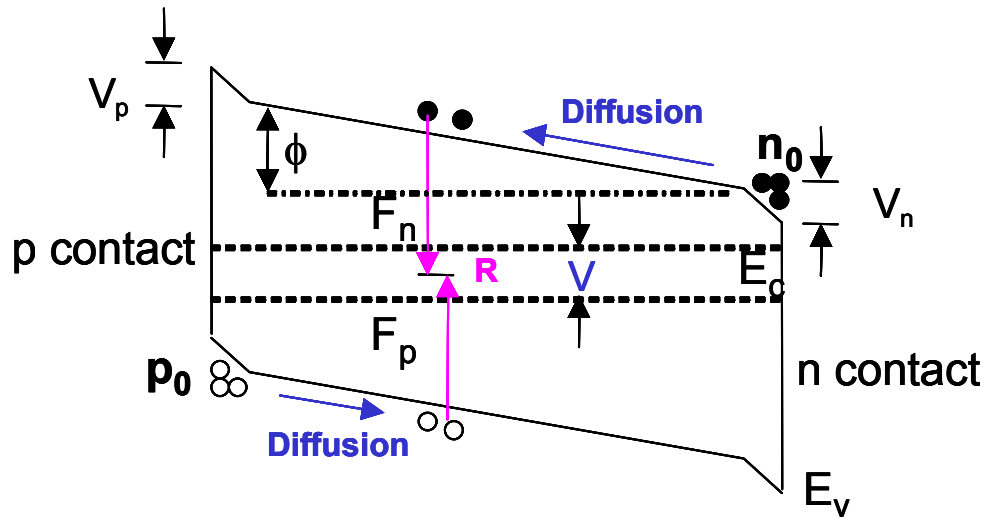
Figure A.1: Schematic band diagram for the i-layer of a p-i-n cell under forward bias in the dark.
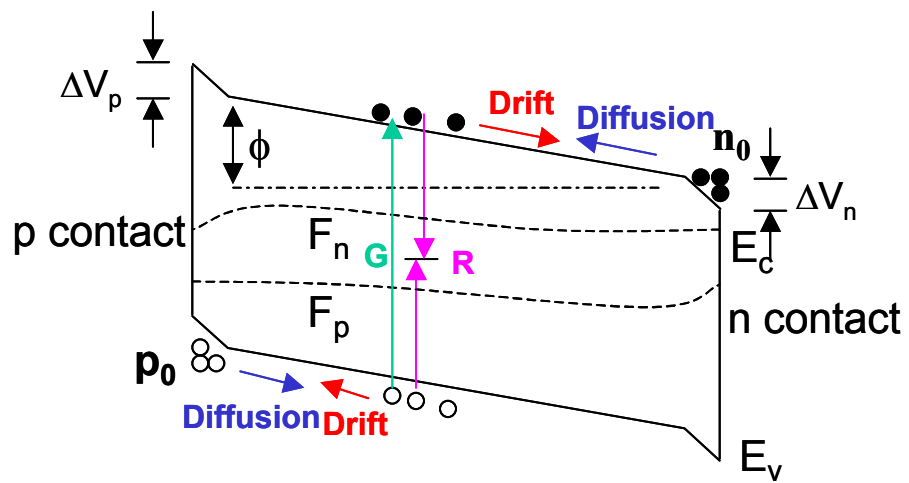
Figure A.2: Schematic band diagram for the i-layer of a p-i-n cell under forward bias and illumination.

REPORT DOCUMENTATION PAGE

Form Approved
OMB No. 0704-0188

1. REPORT DATE *(DD-MM-YYYY)*	2. REPORT TYPE	3. DATES COVERED *(From - To)*
August 2006	Subcontract Report	October 2001–July 2005

4. TITLE AND SUBTITLE
Optimization of Phase-Engineered a-Si:H-Based Multi-Junction Solar Cells: Final Technical Report, October 2001–July 2005

5a. CONTRACT NUMBER
DE-AC36-99-GO10337

5b. GRANT NUMBER

5c. PROGRAM ELEMENT NUMBER

6. AUTHOR(S)
C.R. Wronski, R.W. Collins, N.J. Podraza, V. Vlahos, J.M. Pearce, J. Deng, M. Albert, G.M. Ferreira, and C. Chen

5d. PROJECT NUMBER
NREL/SR-520-40400

5e. TASK NUMBER
PVB65101

5f. WORK UNIT NUMBER

7. PERFORMING ORGANIZATION NAME(S) AND ADDRESS(ES)
Pennsylvania State University
University Park, Pennsylvania

8. PERFORMING ORGANIZATION REPORT NUMBER
NDJ-1-30630-01

9. SPONSORING/MONITORING AGENCY NAME(S) AND ADDRESS(ES)
National Renewable Energy Laboratory
1617 Cole Blvd.
Golden, CO 80401-3393

10. SPONSOR/MONITOR'S ACRONYM(S)
NREL

11. SPONSORING/MONITORING AGENCY REPORT NUMBER
NREL/SR-520-40400

12. DISTRIBUTION AVAILABILITY STATEMENT
National Technical Information Service
U.S. Department of Commerce
5285 Port Royal Road
Springfield, VA 22161

13. SUPPLEMENTARY NOTES
NREL Technical Monitor: B. von Roedern

14. ABSTRACT *(Maximum 200 Words)*
The scope of the work under this subcontract has involved investigating engineered improvements in the performance and stability of solar cells in a *systematic* way, which included the following four tasks: 1. Materials research and device development; 2. Process improvement directed by real time diagnostics; 3. Device loss mechanisms; and 4. Characterization strategies for advanced materials Our work has resulted in new and important insights into the deposition of a-Si:H-based materials, as well as into the nature of the Staebler-Wronski Effect (SWE). Presumably, many of these insights will be used by industrial partners to develop more systematic approaches in optimizing solar cells for higher performance and stability. This effort also cleared up several serious misconceptions about the nature of the p-layer in cells and the SWE in materials and cells. Finally, the subcontract identified future directions that should be pursued for greater understanding and improvement.

15. SUBJECT TERMS
PV; solar cells; high performance; devices; manufacturing; materials research; real-time diagnostics; phase engineering; amorphous silicon; Staebler-Wronski Effect.

16. SECURITY CLASSIFICATION OF:

a. REPORT	b. ABSTRACT	c. THIS PAGE
Unclassified	Unclassified	Unclassified

17. LIMITATION OF ABSTRACT
UL

18. NUMBER OF PAGES

19a. NAME OF RESPONSIBLE PERSON

19b. TELEPHONE NUMBER *(Include area code)*

Standard Form 298 (Rev. 8/98)
Prescribed by ANSI Std. Z39.18

F1146-E(12/2004)